



저작자표시-비영리-변경금지 2.0 대한민국

이용자는 아래의 조건을 따르는 경우에 한하여 자유롭게

- 이 저작물을 복제, 배포, 전송, 전시, 공연 및 방송할 수 있습니다.

다음과 같은 조건을 따라야 합니다:



저작자표시. 귀하는 원저작자를 표시하여야 합니다.



비영리. 귀하는 이 저작물을 영리 목적으로 이용할 수 없습니다.



변경금지. 귀하는 이 저작물을 개작, 변형 또는 가공할 수 없습니다.

- 귀하는, 이 저작물의 재이용이나 배포의 경우, 이 저작물에 적용된 이용허락조건을 명확하게 나타내어야 합니다.
- 저작권자로부터 별도의 허가를 받으면 이러한 조건들은 적용되지 않습니다.

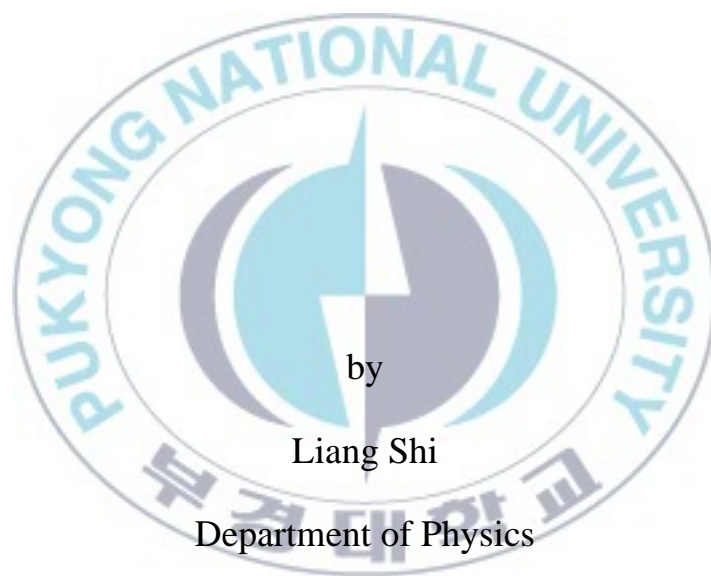
저작권법에 따른 이용자의 권리는 위의 내용에 의하여 영향을 받지 않습니다.

이것은 [이용허락규약\(Legal Code\)](#)을 이해하기 쉽게 요약한 것입니다.

[Disclaimer](#)

Thesis for the Degree of Doctor of Philosophy

Luminescence Dynamics of Eu^{2+} in
 LiBaF_3 Crystals



by

Liang Shi

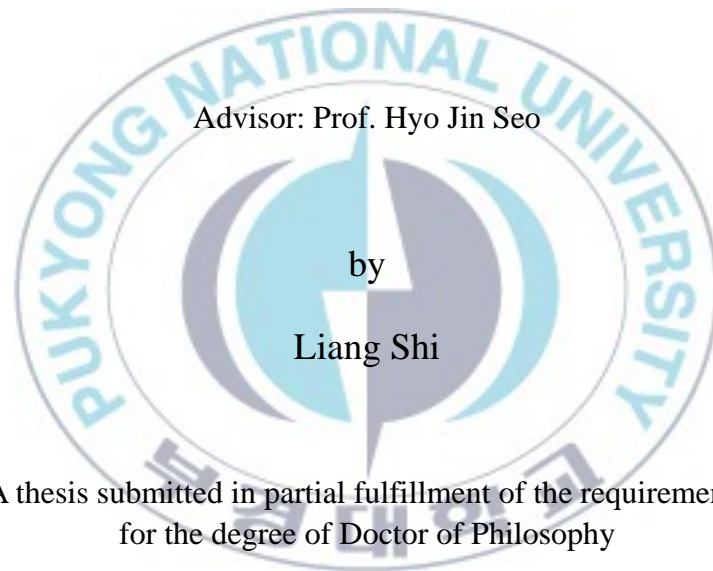
Department of Physics

The Graduate School

Pukyong National University

August 2011

Luminescence Dynamics of Eu^{2+} in
 LiBaF_3 Crystals
 LiBaF_3 결정에 첨가된 Eu^{2+} 이온의
형광 동역학 연구



Advisor: Prof. Hyo Jin Seo

by

Liang Shi

A thesis submitted in partial fulfillment of the requirements
for the degree of Doctor of Philosophy

in Department of Physics, The Graduate School,
Pukyong National University

August 2011

Luminescence Dynamics of Eu^{2+} in LiBaF_3 Crystals

A dissertation

by

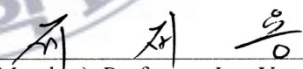
Liang Shi

Approved by:



(Chairman) Professor Chi Il Ok


(Member) Professor Palamandala Babu


(Member) Professor Jae Yong Je


(Member) Doctor Kyoung Hyuk Jang


(Member) Professor Hyo Jin Seo

August 25, 2011

Contents

Abstract	i
1. Introduction	1
2. Background of crystal growth and luminescence dynamics	5
2.1 Crystal growth by the Czochralski method	5
2.2 Crystal structure of ABF ₃ type fluorides	9
2.3 Site-occupation of RE ions in ABF ₃ lattices	12
2.4 Radiative and nonradiative transitions	16
2.5 Energy levels and excited states of Eu ²⁺ ions in solid	19
2.6 Relaxation process of excited states in a three-level system	22
2.7 Mixing of Eu ²⁺ 4f (⁶ P _{7/2}) and 5d (E _g) states by tunnelling Process	25
3. Experimental procedure	28
3.1 Preparation of single crystals	28
3.1.1 Synthesis procedure of LiBaF ₃ powder	30
3.1.2 X-ray diffraction analysis	35
3.1.3 Growth of LiBaF ₃ single crystals	36
3.2 Spectroscopic measurements	39

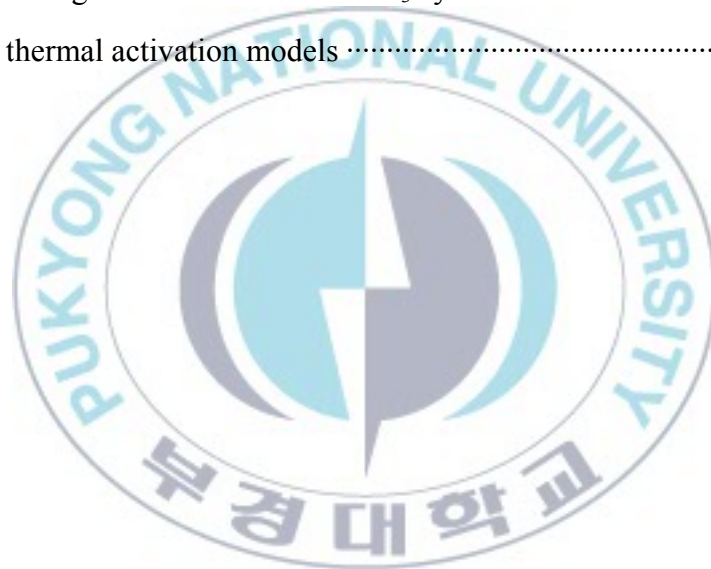
3.2.1	Measurements of absorption spectrum	39
3.2.2	Luminescence excitation and emission spectra	41
3.2.3	Luminescence spectra and decay measurements by the pulsed laser excitation	43
4.	Results and discussion	45
4.1	Growth of $\text{LiBaF}_3:\text{Eu}^{2+}$ single crystals	45
4.1.1	Different degrees of calcinations	45
4.1.2	Results of different ratios of the LiF and BaF_2 powders	48
4.1.3	The initial temperature cooling rate	50
4.1.4	Rotation and pulling speeds	51
4.2	Energy level structure of $\text{LiBaF}_3:\text{Eu}^{2+}$ single crystal	52
4.2.1	Absorption and excitation spectra of Eu^{2+} in LiBaF_3	52
4.2.2	Emission spectra of Eu^{2+} in LiBaF_3	55
4.3	Zero-phonon lines and phonon side bands of the ${}^6\text{P}_{7/2} \rightarrow {}^8\text{S}_{7/2}$ transition	58
4.4	Relaxation process of excited states of Eu^{2+} in LiBaF_3	66
4.4.1	Thermal activation and quenching of the excited $4f({}^6\text{P}_{7/2})$ and $5d(\text{E}_g)$ states in LiBaF_3	66
4.4.2	Calculations of energy barriers E_1 and E_2	84
4.5	Quantum tunneling process in double wells of the $4f({}^6\text{P}_{7/2})$ and $5d(\text{E}_g)$ states of Eu^{2+} in LiBaF_3	92

4.5.1 410-nm slow component by tunneling process	92
4.5.2 Anomalous spectral feature and nonexponential decay curves of 410-nm slow component	101
5. Conclusions	105
6. References	108
7. Publication List	112
8. Acknowledgement	116



List of Tables

Table 2.1 Typical ABF ₃ compounds	10
Table 2.2 Effective ionic radius	14
Table 4.1 The positions of the Stokes and anti-Stokes vibration lines of LiBaF ₃ : Eu ²⁺ single crystal	65
Table 4.2 Fitting values of Eu ²⁺ in LiBaF ₃ by the three-level and thermal activation models	91



List of Figures

Figure 2.1 Instruction of the Czochralski method	8
Figure 2.2 Cubic perovskite structure of ABF_3	11
Figure 2.3 The inverse-perovskite structure of $LiBaF_3$ crystalline	15
Figure 2.4 Configurational coordinate diagram. E is radiative energy. ABS is the absorption process. Em is the emission process. Parabola e is the excited state of the ground state g. e' is the excited state of another level	18
Figure 2.5 Schematic energy level diagram of the Eu^{2+} ion. Left side is the energy levels of $4f^7$ configuration. Right side is the energy levels of $4f^65d$ configuration. The degeneracy of the $5d$ level is split into the doubly-degenerate (E_g) and the threefold-degenerate (T_{2g}) energy levels in a crystal. 10 Dq is the energy gap between the T_{2g} and E_g levels	21
Figure 2.6 Three-level system with two metastable states (2 and 3) and one ground state (1)	24
Figure 3.1 Preparative procedure diagram of the $LiBaF_3$ single crystal ...	29
Figure 3.2 Phase diagram of the LiF - BaF_2 system	31
Figure 3.3 Differential thermal analysis (DTA) curves of LiF - BaF_2 mixture	33
Figure 3.4 The crystal growth system for the Czochralski method	34
Figure 3.5 Illustration of crystal growth chamber. Pure $LiBaF_3$ crystal	

seeds were used to grow single crystals	37
Figure 3.6 Photo of a LiBaF ₃ single crystal	38
Figure 3.7 Schematic diagram of a single-beam spectrophotometer	40
Figure 3.8 Schematic diagram of the main elements for measuring photoluminescence spectra	42
Figure 3.9 The equipment diagram of spectroscopy measurement system. The fourth harmonic of Nd:YAG laser was used to get a beam of 266 nm laser which was transmitted to the workbench by a group of mirrors. The 266 nm laser with 25 mJ energy was focused by a lens and crossed two polished faces of the LiBaF ₃ :Eu ²⁺ single crystal	44
Figure 4.1 XRD diagram of the LiBaF ₃ powder (a) with LiF 60 mol% after one time calcination	46
Figure 4.2 XRD diagram of the LiBaF ₃ powder (b) with LiF 60 mol% after two times calcinations	47
Figure 4.3 XRD diagram of the LiBaF ₃ powder (c) with LiF 55 mol% after two times calcinations	49
Figure 4.4 (a) Absorption spectrum (solid line) of LiBaF ₃ :Eu ²⁺ single crystal. (b) Excitation spectrum of the Eu ²⁺ obtained by monitoring at sharp line or broad band emissions	53
Figure 4.5 Energy level diagram of the 4 <i>f</i> → 5 <i>d</i> transition for absorption or excitation of Eu ²⁺ in LiBaF ₃	54
Figure 4.6 Emission spectrum of LiBaF ₃ :Eu ²⁺ single crystal obtained	

at (a) RT and (b) 15 K	56
Figure 4.7 Energy levels of Eu^{2+} ion in LiBaF_3	57
Figure 4.8 The high resolution emission spectra of the ${}^6\text{P}_{7/2} \rightarrow {}^8\text{S}_{7/2}$ transition of Eu^{2+} in LiBaF_3 single crystal at 15 K	59
Figure 4.9 The zero-phonon line (359 nm), Stokes and anti-Stokes vibration lines of $\text{LiBaF}_3:\text{Eu}^{2+}$ single crystals	60
Figure 4.10 Line emission spectra of the $\text{LiBaF}_3:\text{Eu}^{2+}$ single crystal at low temperatures. The zero-phonon line was observed at 359 nm. The other peaks were due to Stokes and anti-Stokes vibrations	63
Figure 4.11 Temperature-dependent line emission spectra of $4f \rightarrow 4f$ transitions under 266 nm excitation at different temperatures and the inset is variation of their integrated intensity	64
Figure 4.12 Decay curves of 359 nm emission of $\text{LiBaF}_3:\text{Eu}^{2+}$ single crystal at temperature range between 15 and 300 K under 266 nm excitation	67
Figure 4.13 The experimental decay values of line emissions as a function of temperature. The inset is the logarithmic scale of decay values	68
Figure 4.14 (a) rise time of line emissions at 359 nm at low temperatures. (b) the calculated values of rise time as a function of temperature. (c) the energy transfer model between the excited $4f$ and $5d$ states	69

Figure 4.15 (a) The normalized initial and integrated intensities of emissions at 359 nm in the temperature region of 15-100 K.	
(b) The transfer model between the excited $4f$ and $5d$ states	72
Figure 4.16 The integrated intensity and decay values of line emissions at 359 nm in the temperature region of 15-300 K	73
Figure 4.17 Decay curves of broad band emission (monitoring at 410 nm) of $5d \rightarrow 4f$ transition at the temperature range between 15 and 100 K under 266 nm excitation	75
Figure 4.18 The experimental decay values of short component as a function of temperature. The inset is the logarithmic scale of decay values	76
Figure 4.19 The integrated intensity and decay curves of fast component in the temperature region of 15-100 K	77
Figure 4.20 Time-resolved ($t=0-0.5 \mu\text{s}$) emission spectra with fast decay component at different temperatures and the inset is variation of their integrated intensity	78
Figure 4.21 Decay curves of slow component of emission band (monitoring at 410 nm) of $\text{LiBaF}_3: \text{Eu}^{2+}$ single crystal in the temperature range between 15 and 300 K under 266 nm excitation	80
Figure 4.22 The calculated decay values of slow component as a	

function of temperature. The inset is the logarithmic scale of decay values	81
Figure 4.23 Mixed decay curves with fast and slow components of band emission at 410 nm at 20 K. Solid line is the best fitting for the equation 4.4.1	83
Figure 4.24 Configurational coordinate diagram of the $\text{LiBaF}_3:\text{Eu}^{2+}$ single crystal. ΔE is the energy difference between the excited $4f$ and $5d$ levels. P_d , P_f , W_{df} , and W_{fd} are the radiative and nonradiative probabilities between the $5d$ level and excited $4f$ level, respectively	85
Figure 4.25 Decay values of line emission (359 nm) (single points). The solid lines are the best-fit of the thermal activation (a) and three-level (b) models	88
Figure 4.26 Decay values of fast component of band emission (410 nm) (single points). The solid lines are the best-fit of the thermal activation (a) and three-level (b) models	89
Figure 4.27 Configurational coordinate diagram of energy levels of Eu^{2+} in LiBaF_3	90
Figure 4.28 (a) Integrated intensities of band emissions at 410 nm with slow decay component. (b) The thermal activation (2) and tunneling (1) transfers between the excited $4f$ and $5d$ states	95
Figure 4.29 (a) Decay values of band emissions at 410 nm with fast	

and slow decay components in temperature region of 15-180 K. (b) The thermal activation (arrows 1 and 3) and tunneling (2) transfers between the excited $4f$ and $5d$ states 96

Figure 4.30 The calculated decay values of emission at 359 nm (circle) and 410 nm (triangle) with slow decay component of $\text{LiBaF}_3:\text{Eu}^{2+}$ single crystal between 15 and 300 K under 266 nm excitation. The inset is logarithmic scale of decay values 97

Figure 4.31 (a) the normalized initial and integrated intensities of fast component at 410 nm in 15-100 K. (b) the normalized initial intensity of fast component at 410 nm in 15-40 K 98

Figure 4.32 The integrated intensity curve of slow component of band emission at 410 nm in the temperature region of 15-300 K, the inset is the intensity in 15-80 K 99

Figure 4.33 Decay curves of 359 nm emission and 410 nm emission with slow component at 15 K 103

Figure 4.34 Time-resolved emission spectra of the $\text{LiBaF}_3:\text{Eu}^{2+}$ single crystal at 18 K excited by 266 nm laser. (a) and (b) are the band emissions monitoring at the fast and slow decay components by using the time gate (Δt) = 0-3.6 μs and 0.4-1.8 ms, respectively 104

Luminescence dynamics of Eu^{2+} in LiBaF_3 crystals

Liang Shi

Department of Physics, The Graduate School,
Pukyong National University

Abstract

Pure and Eu^{2+} doped LiBaF_3 single crystals have been grown by the Czochralski method. The detailed preparation procedure of crystal growth has been investigated. The melting point of LiBaF_3 powder has been analyzed by the DTA measurement. The lattice parameters and phase identification have been measured by XRD. It has been confirmed that the different mole ratios of $\text{LiF}:\text{BaF}_2$ powder and calcinations times can greatly influence the purity of LiBaF_3 compounds. The substitution mechanism of Eu^{2+} ion has been discussed, and the Ba^{2+} site is reasonable in LiBaF_3 crystal.

The absorption and excitation spectra show two band peaks due to the splitting of $5d$ states. The high resolution emission spectra show a line emission near 359 nm from $4f' \rightarrow 4f$ transition and a band emission maximum at 410 nm from the $5d \rightarrow 4f$ transition. The zero-phonon line of the $4f' \rightarrow 4f$ transition is observed with some Stokes and anti-Stokes vibrations, and their intensity shows strong temperature dependence. The luminescent decays of line and band emissions monitoring at 359 and 410 nm have been measured in the temperature range from 15 to 300 K. The decay of band emission at 410 nm has two components: fast ($\sim \mu\text{s}$) and slow ($\sim \text{ms}$) components. A three-level model of Eu^{2+} in LiBaF_3 host was successfully built, and the energy barriers and transition rates of the excited $4f$ and $5d$ states were obtained by using the thermal quenching and three-level models,

respectively.

The initial and integrated emission intensities, temperature-dependent decay values, rise times and non-exponential decay curves of line and band emissions show a quantum tunneling process resulting in unusual energy back transfer from the excited $4f$ to $5d$ states at low temperature. The luminescence dynamics of $\text{LiBaF}_3:\text{Eu}^{2+}$ from 15 to 300 K have been well discussed. The anomalous relaxation process is caused by the energy transfer and back transfer processes between $4f$ to $5d$ states assigned to competition of the thermal activated and quantum tunneling effects.



1. Introduction

It is well recognized that the rare earth ions (RE) have the most complicated optical spectra, because they have rich energy levels of the $4f \rightarrow 4f$ transitions. The rare earth ions can be present in solids either in the divalent (RE^{2+}) or trivalent (RE^{3+}) states in which electronic configurations are $4f^n 5s^2 5p^6$ or $4f^{n-1} 5s^2 5p^6$, respectively. The electrons in the $4f$ shell are well shielded by outside shells of $5s^2 5p^0$. Therefore, the transitions within the $4f$ configurations are forbidden for the electric dipole transition by the parity selection rule. However, they are usually observed in some crystals due to the effects of special crystal fields which mix some different parity states into the $4f$ states. For the trivalent rare earth ions (i.e. Eu^{3+} and Sm^{3+}), the $4f^n$ configuration is relatively isolated and the $4f^{n-1} 5d$ lies in a high energy above the ground term of the $4f^n$ configuration and many line emissions can be obtained due to the $4f \rightarrow 4f$ transitions. For the divalent rare earth ions (i.e. Eu^{2+} and Sm^{2+}), the energy separation between the $4f^n$ and $4f^{n-1} 5d$ configurations depends strongly on a host lattice and the transitions between them can be observed as band emissions [1-5].

The Eu^{2+} ion has the $4f^7 5s^2 5p^6$ (named $4f$ hereafter) electronic configuration as the ground state and $4f^6 5s^2 5p^6 5d$ ($5d$) as the first excited electronic configuration. The interconfigurational electronic $4f^7 (^8S_{7/2}) \rightarrow 5d$ transition is parity allowed, while the intraconfigurational $4f^7 (^8S_{7/2}) \rightarrow 4f^7 (^6P_{7/2})$ transition is parity-forbidden. Therefore the optical absorption due to the latter transition is much weaker than the absorption due to the former transition [5,

6]. The Eu^{2+} emission varies from ultraviolet to red depending on the covalency, the radii of the cation, lattice vibrations (phonons), and the crystal field strength of the host lattice [5, 7]. Because the transitions between the $4f^7$ ($^8\text{S}_{7/2}$) ground state and the crystal field components of the $5d$ excited state configuration are parity allowed, they depend strongly on the crystal field strength and lattice vibration. The decay time of these transitions is usually in the range from 0.2 to 2 μs , whereas the radiative lifetime of the emission from transitions within the $4f^7$ configuration is in the order of a millisecond [2-4].

The optical properties of a luminescent center in different host lattices are different because the ions experience the different surroundings of such a center. Compare with the general RE-doped oxide-based host materials, the fluoride has lower covalency property which brings higher energy levels [5]. The intraconfigurational $4f^7$ ($^8\text{S}_{7/2}$) \rightarrow $4f^7$ ($^6\text{P}_{7/2}$) transition of Eu^{2+} has a relative higher energy and it can be observed only when the lowest $5d$ component situates above the $^6\text{P}_J$ states of the $4f$ configuration [8-10]. In the fluoride host, the spectral positions of the $4f^n \rightarrow 4f^{n-1}5d$ transition tend to be at slightly higher energy than in the oxide which increases probability of the appearance of the $4f$ ($^6\text{P}_{7/2}$) \rightarrow $4f$ ($^8\text{S}_{7/2}$) transition in spectra.

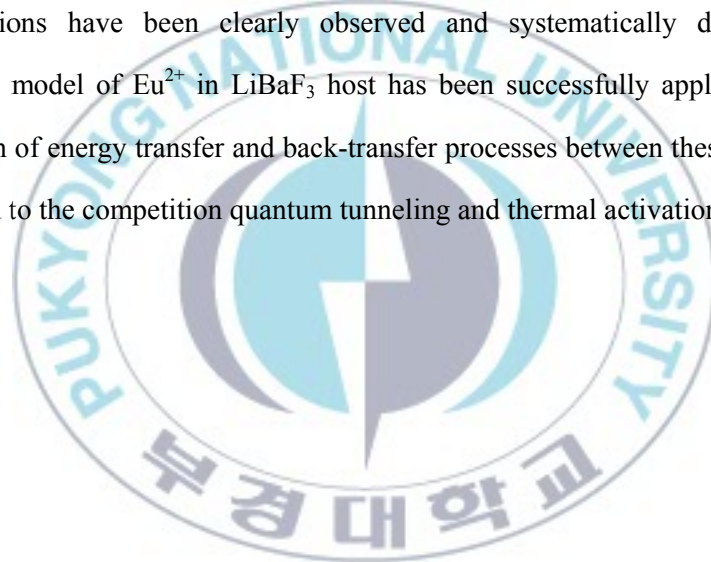
Recently, rare earth ions doped LiBaF_3 materials have been obtained much more attentions for their good luminescent and optical properties [11-14]. Moreover, the structure of LiBaF_3 is relatively simple and the melting point is not very high, which means the LiBaF_3 single crystals can be easily obtained [15-18]. However, the luminescence of Eu^{2+} -doped LiBaF_3 was not often reported at

temperature region lower than 70 K. It is known that magnetic dipole $4f(^8S_{7/2}) \rightarrow 4f(^6P_{7/2}, ^6P_{5/2})$ transitions and the vibronic coupling strengths of intra- $4f$ transitions of Eu^{2+} are similar with the properties of Gd^{3+} . The line emissions peaking at 359 nm were assigned to the intra- $4f$ transitions ($^8S_{7/2} \rightarrow ^6P_{7/2}$) of Eu^{2+} . But, another broad band emission with maximum at 410 nm was established. Meijerink [9] suggested that it is from the common $5d \rightarrow 4f$ transition, but no lifetimes were shown in the relation with this emission band and the $5d \rightarrow 4f$ transition. Mahlik [10] et al. reported it is from the impurity trapped excitons, but lacking of the low temperature (< 70 K) data makes this viewpoint not very clear. Therefore, to know the mechanism of this broad band emission is one of the key points of our study.

With the increasing market of solid state lighting, many literatures have been published focusing on the Eu^{2+} -doped materials with band emission for their potential applications [19-23]. However, doing research on the temperature-dependent luminescence dynamics or understanding relation between the excited $4f$ and the $5d$ states in low temperature (< 70 K) is also a very interesting and important work. Because, in such low temperatures, the phonon vibration effect is very weak and it makes clear of the some transition mechanisms by eliminating the thermal disturbance of the process.

In this thesis, Chapter 2 shows a brief introduction of backgrounds such crystal growth theory, crystal structure of LiBaF_3 host, nonradiative and radiative process, luminescence of Eu^{2+} , introduction of classic three-level system, and quantum tunneling process. Chapter 3 shows the experimental procedure of crystal growth by the Czochralski method and the spectroscopic measurements. The

Eu^{2+} -doped LiBaF_3 single crystals have been successfully grown. Chapter 4 indicates the main research in this thesis. In this Chapter, a series of line emissions near 359 nm and a broad band emission with a maximum at 410 nm have been also observed under 266 nm laser excitation. The time-resolved emission spectra and temperature dependent decays of $\text{LiBaF}_3:\text{Eu}^{2+}$ have been carefully measured and the energy transfer and back transfer between $4f(^6\text{P}_{7/2})$ and $5d(\text{E}_g)$ states was first reported. The initial rise times and non-exponential decay curves of 359 and 410 nm emissions have been clearly observed and systematically discussed. A three-level model of Eu^{2+} in LiBaF_3 host has been successfully applied, and the mechanism of energy transfer and back-transfer processes between these two states is assigned to the competition quantum tunneling and thermal activation effects.



2. Background of crystal growth and luminescence dynamics

2.1 Crystal growth by the Czochralski method

Crystal is the solid material whose constituent atoms, molecules, or ions are arranged in an orderly repeating pattern extending in all three spatial dimensions. Crystal growth is a major stage of a crystallization process, and consists in the addition of new atoms, ions, or polymer strings into the characteristic arrangement of a crystalline Bravais lattice. The growth typically follows an initial stage of either homogeneous or heterogeneous (surface catalyzed) nucleation, unless a ‘seed’ crystal, purposely added to start the growth, was already present. There are many methods for growing high quality crystals such as Czochralski method, Bridgman method, floating zone method, and hydrothermal synthesis.

The Czochralski method is a particular method of crystal growth, wherein a seed is touched on top of the melt contained in a crucible and drawn slowly at a controlled rate. Then the crystal grows below the seed. The seed and the crystal are often rotated to provide a uniform growth environment. The rate of rotation and pulling speeds can be changed to get single crystals with different diameters. Fluid motion within the melt is important because it affects the quality of the crystal. The flow driving forces considered are buoyancy, crystal rotation and surface-tension gradient.

The Bridgman method involves heating polycrystalline material above its melting point and slowly cooling it from one end of its container, where a seed crystal is located. A single crystal of the same crystallographic orientation as the seed material is grown on the seed and is progressively formed along the length of the container. The process can be carried out in a horizontal or vertical geometry. This method is a popular way of producing certain semiconductor crystals for which the Czochralski process is more difficult, such as gallium arsenide.

Floating zone method is a group of similar methods of purifying crystals, in which a narrow region of a crystal is molten, and this molten zone is moved along the crystal (in practice, the crystal is pulled through the heater). The molten region melts impure solid at its forward edge and leaves a wake of purer material solidified behind it as it moves through the ingot. The impurities concentrate in the melt, and are moved to one end of the ingot.

Hydrothermal synthesis can be defined as a method of synthesis of single crystals that depend on the solubility of minerals in hot water under high pressure. The crystal growth is performed in an apparatus consisting of a steel pressure vessel called autoclave, in which a nutrient is supplied along with water. A gradient of temperature is maintained at the opposite ends of the growth chamber so that the hotter end dissolves the nutrient and the cooler end causes seeds to take additional growth.

There are many methods to get high quality crystals, why we choose the Czochralski method to grow the LiBaF_3 single crystals in this work? Because using this method with precisely controlling the temperature gradients, pulling and

rotation speeds, it is possible to extract a large, single-crystal, cylindrical ingot from the melt. Occurrence of unwanted instabilities in the melt can be avoided by investigating and visualizing the temperature and velocity fields during the crystal growth process. It is known that the Bridgman method is also very good for growing high quality single crystal, but the growing process is relative slow. For the hydrothermal method, it needs expensive autoclaves, and the experimental repeating is very low. For Floating zone method, it is very hard to get single crystals. Therefore, the Czochralski method is the best choose for us to get the LiBaF_3 single crystals.

The instruction of the Czochralski method is shown in figure 2.1, wherein a seed crystal is touched on top of the melt contained in a crucible and drawn slowly at a controlled rate. The crystal grows below the seed. The seed and the crystal are often rotated to provide a uniform growth environment. Fluid motion within the melt is important because it affects the quality of the crystal. The flow driving forces considered are buoyancy, crystal rotation and surface-tension gradient. The detailed growing method will be discussed later.

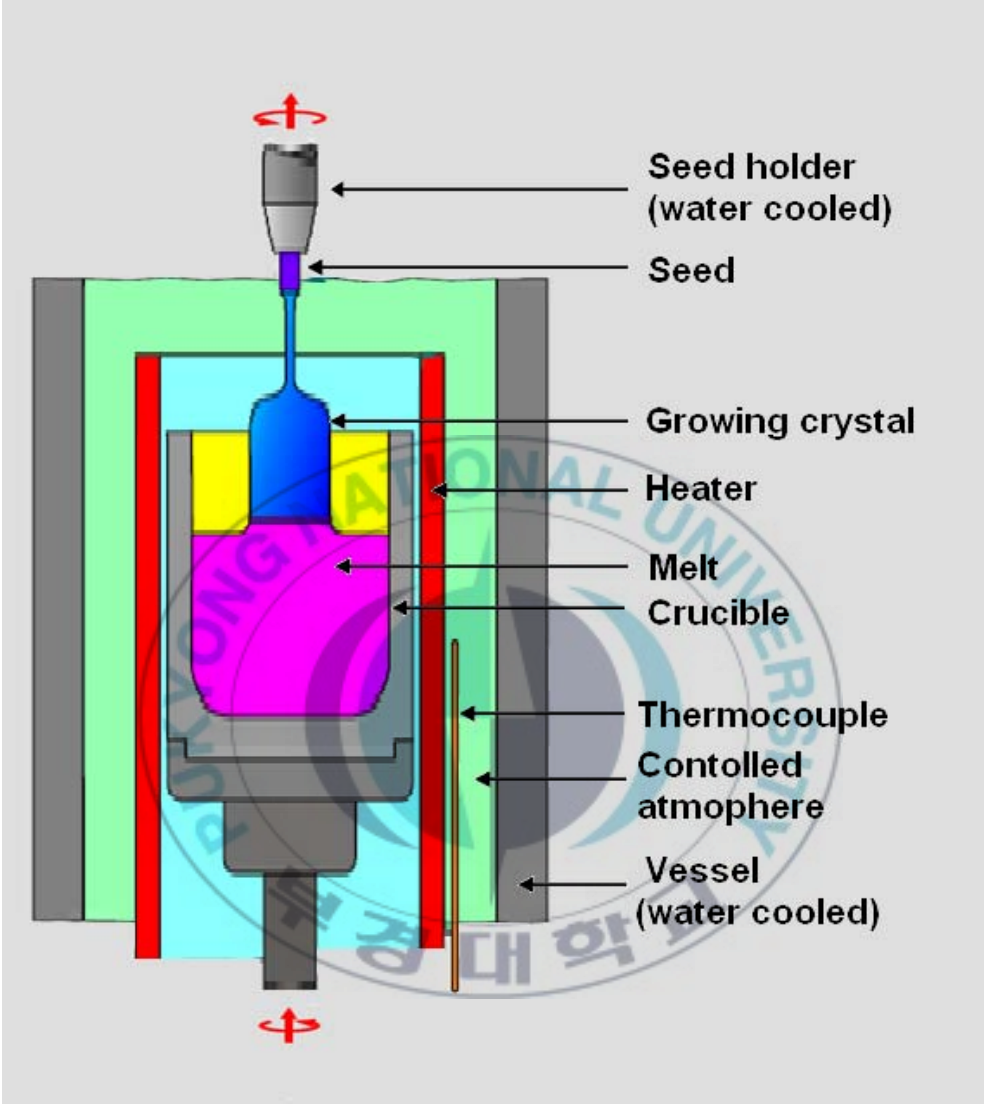


Figure 2.1 Instruction of the Czochralski method.

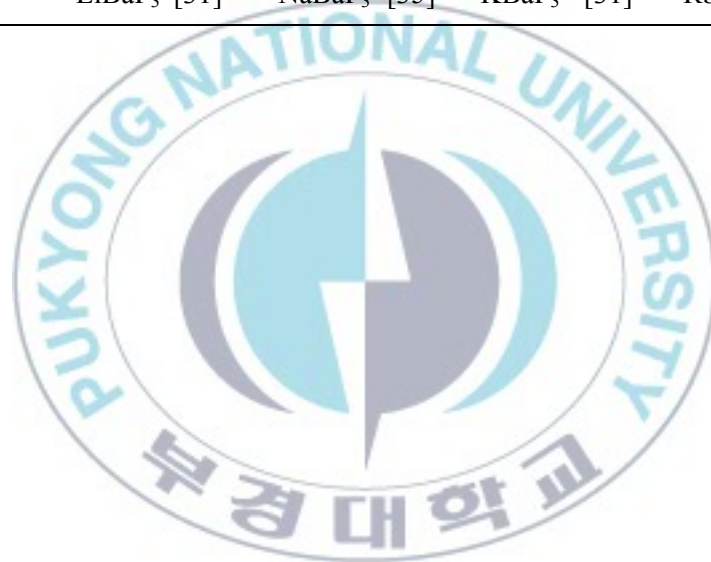
2.2 Crystal structure of ABF₃ type fluorides

The lattices ABF₃ (A = alkali, B = alkali-earth ion) have a structure of the perovskite-type with space group $Pm\bar{3}m$ (No. 221)[24-26]. Table 2.1 shows the compounds of typical ABF₃ compounds [1]. The perovskite structure is generally described as a three-dimensional arrangement of a corner-sharing octahedral BF_6 unit (which forms the ReO_3 -structure type), with the A ion placed in the cuboctahedral interstices. Therefore, the A⁺ ions are surrounded by twelve F⁻ ions and the B²⁺ ions by six F⁻ ions [27, 28]. In the ideal case, this structure is cubic as shown in figure 2.2. Generally, when the size of A⁺ > B²⁺, it is a typical perovskite-type such as KMgF₃ and RbMgF₃. Otherwise, it shows an inverse perovskite-type such as LiBaF₃ and NaSrF₃.

Recently, the applications of pure and rare earth ions doped ABF₃ type materials have been a lot reported. LiBaF₃ can be used as thermal neutron detectors [14]. KMgF₃:RE were investigated due to their potential applications in UV scintillators and dosimeters [29]. NaMgF₃:Ce³⁺ was researched as a solid state personal dosimeter [30]. Therefore, ABF₃ type materials will be obtained more and more attentions in future.

Table 2.1 Typical ABF₃ compounds.

B ²⁺ \ A ⁺	Li ⁺	Na ⁺	K ⁺	Rb ⁺
Mg ²⁺	LiMgF ₃ [31]	NaMgF ₃ [30]	KMgF ₃ [29]	RbMgF ₃ [32]
Ca ²⁺	LiCaF ₃ [31]	NaCaF ₃ [33]	KCaF ₃ [34]	RbCaF ₃ [34]
Sr ²⁺	LiSrF ₃ [31]	NaSrF ₃ [34]	KSrF ₃ [34]	RbSrF ₃ [34]
Ba ²⁺	LiBaF ₃ [31]	NaBaF ₃ [35]	KBaF ₃ [31]	RbBaF ₃ [36]



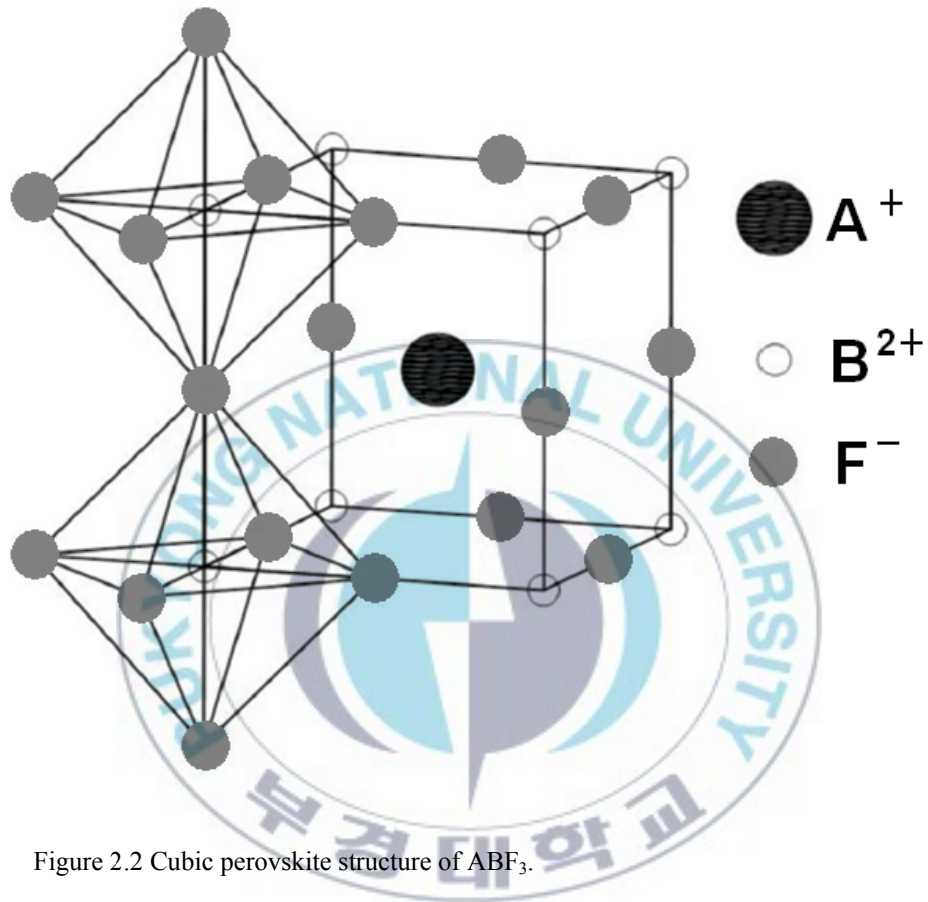
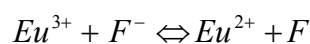


Figure 2.2 Cubic perovskite structure of ABF_3 .

2.3 Site-occupation of RE ions in ABF₃ lattices

Rare earth (RE) ions doped ABF₃ fluorides have been well studied during the last few decades such as Eu²⁺, Eu³⁺, Gd³⁺, Ce³⁺, and Yb²⁺ [37-41]. However, the site occupation of the rare earth ions in different ABF₃ fluorides is obviously different. For example, in KMgF₃ and KZnF₃ single crystals, the Eu²⁺ ion substitutes for the singly-charged cation (K⁺) with a twelvefold fluorine coordination and the charge-compensation defect is located in the second cation coordination sphere giving rise to complex with axial symmetry. The effective ionic radius of A⁺, B²⁺ and rare earth ions are shown in table 2.2 [42].

LiBaF₃ has a inverse-perovskite cubic structure ($a_0 = 3.988 \text{ \AA}$) [16, 43]. The Li⁺ ion is surrounded by six F⁻ ions while the Ba²⁺ ion by twelve F⁻ ions in this compound. The regular lattice site of Ba²⁺ ion in LiBaF₃ has the O_h point group symmetry [40] and the crystal structure of the LiBaF₃ is shown in figure 2.3. When Eu³⁺ (EuF₃ used) ion is incorporated in the LiBaF₃ lattice, on a regular site, it must be accompanied by a charge compensating defect. It was reported [44] that when Eu³⁺ ion enters the lattice, F⁻ ion will be oxidized to compensate the charge. The chemical equation is shown as follows,



The ionic radius of Eu²⁺ (>1.35 Å, CN=12) is closer to the Ba²⁺ radius (1.61 Å,

CN=12) and bigger than that of Eu^{3+} ($>1.12 \text{ \AA}$, CN=12) [42]. Moreover, the valence of Eu^{2+} ion is the same as that of Ba^{2+} ion. Therefore, the structure of Eu^{2+} substituting the Ba^{2+} site is more stable than Eu^{3+} ion. This is the reason why the EuF_3 is used and finally the Eu^{2+} ion is the main component substituting the Ba^{2+} ion in LiBaF_3 crystals. However, the complete reaction of the Eu^{3+} and F^- ion is impossible which indicates the existence of Eu^{3+} ion [37].



Table 2.2 Effective ionic radius [42].

	Alkali metals (Å)				Alkaline-earth metals (Å)			
	Li ⁺	Na ⁺	K ⁺	Rb ⁺	Mg ²⁺	Ca ²⁺	Sr ²⁺	Ba ²⁺
CN=6	0.76	1.02	1.38	1.52	0.72	1.00	1.18	1.35
7	*	1.12	1.46	1.56	*	1.06	1.21	1.38
8	0.92	1.18	1.51	1.61	0.89	1.12	1.26	1.42
9	*	1.24	1.55	1.63	*	1.18	1.31	1.47
10	*	*	1.59	1.66	*	1.23	1.36	1.52
11	*	*	*	1.69	*	*	*	1.57
12	*	1.39	1.64	1.72	*	1.34	1.44	1.61
Rare earth ions (Å)								
	Ce ³⁺	Pr ³⁺	Sm ³⁺	Sm ²⁺	Eu ³⁺	Eu ²⁺	Gd ³⁺	Dy ³⁺
CN=6	1.01	0.99	0.96	*	0.95	1.17	0.94	0.91
7	1.07	*	1.02	1.22	1.01	1.20	1.00	0.97
8	1.14	1.13	1.08	1.27	1.06	1.25	1.05	1.03

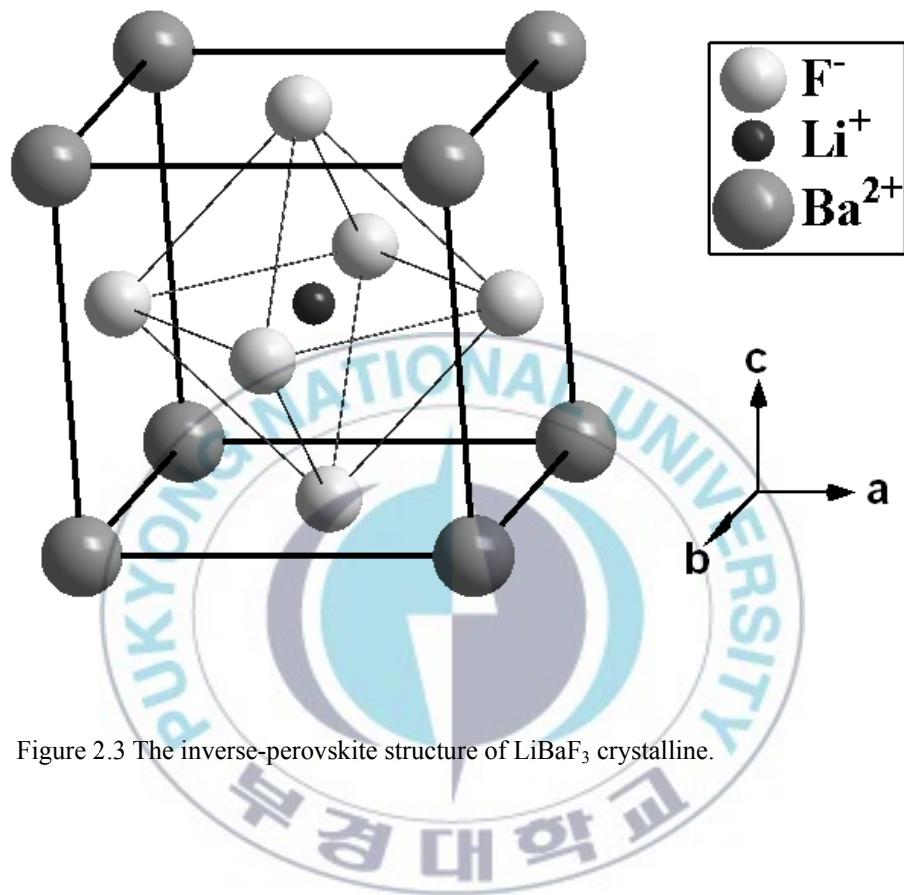


Figure 2.3 The inverse-perovskite structure of LiBaF_3 crystalline.

2.4 Radiative and nonradiative transitions

When a luminescence material absorbs energy from the surrounding and excited to a high energy state, how does it return to the ground state and release the additional energy? In general, there are two ways to return to the ground state, radiative and nonradiative transitions [5]. Figure 2.4 shows the configurational coordinate diagram. In the original Franck–Condon principle, after the electronic transition, the molecules which end up in higher vibrational states immediately begin to relax to the lowest vibrational state. Then, there are many ways to go back to ground state which will be discussed as follows:

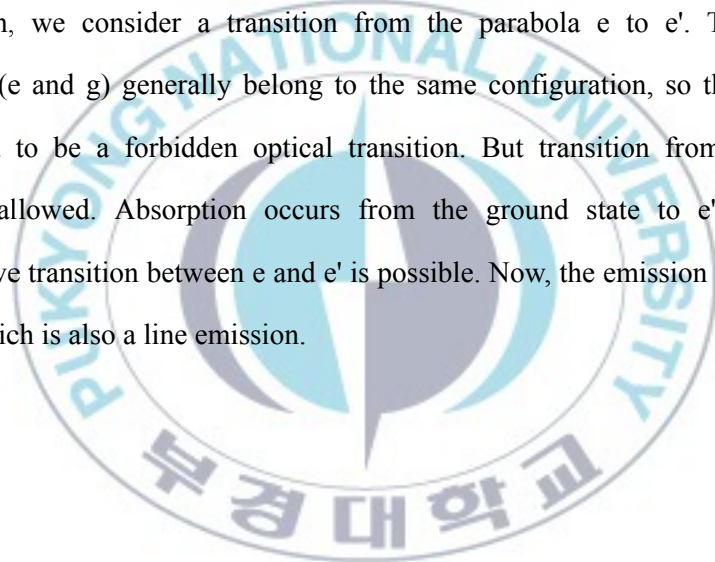
First, let's consider two parabolas *g* and *e*. In this diagram, from the same energy level, they are of the same shape, but parabola *e* is the excited state of the ground state (*g*). There is no offset ($\Delta R = 0$) between *g* and *e*, and they will never cross. When the luminescent ion absorbs energy and goes to the lowest vibrational level of the excited state (*e*), this ion can spontaneously emit energy to return to the ground state and this sharp emission line is called zero-phonon line (e.g. $4f \rightarrow 4f$ transition of Eu^{2+}). If the energy is a little high, this ion is excited to the high vibrational level. The excited ion has to relax the additional energy to the lowest vibrational level and returns to the ground state. This relaxation process is one of the nonradiative ways.

Second, we consider an electron which is excited to another orbit such as the $4f \rightarrow 5d$ absorption of the Eu^{2+} ion. Also, the electron can be excited from the

ground state (g) to the edge of the excited state (e') in this figure. There is an offset ($\Delta R > 0$) between the parabolas of the ground (g) and excited (e') state. Then the excited ion relaxes its additional energy and returns to the lowest vibrational level where the transition of the e' to g state occurs resulting in a broad band spectrum.

Third, if the temperature is high enough, the electron via the cross of e' and g states is possible to return to the ground state in a nonradiative way. The excited energy is then completely thermal quenched in host lattice.

Fourth, we consider a transition from the parabola e to e'. The parallel parabolas (e and g) generally belong to the same configuration, so that they are considered to be a forbidden optical transition. But transition from e' to g is normally allowed. Absorption occurs from the ground state to e'. Also, the nonradiative transition between e and e' is possible. Now, the emission occurs from e state, which is also a line emission.



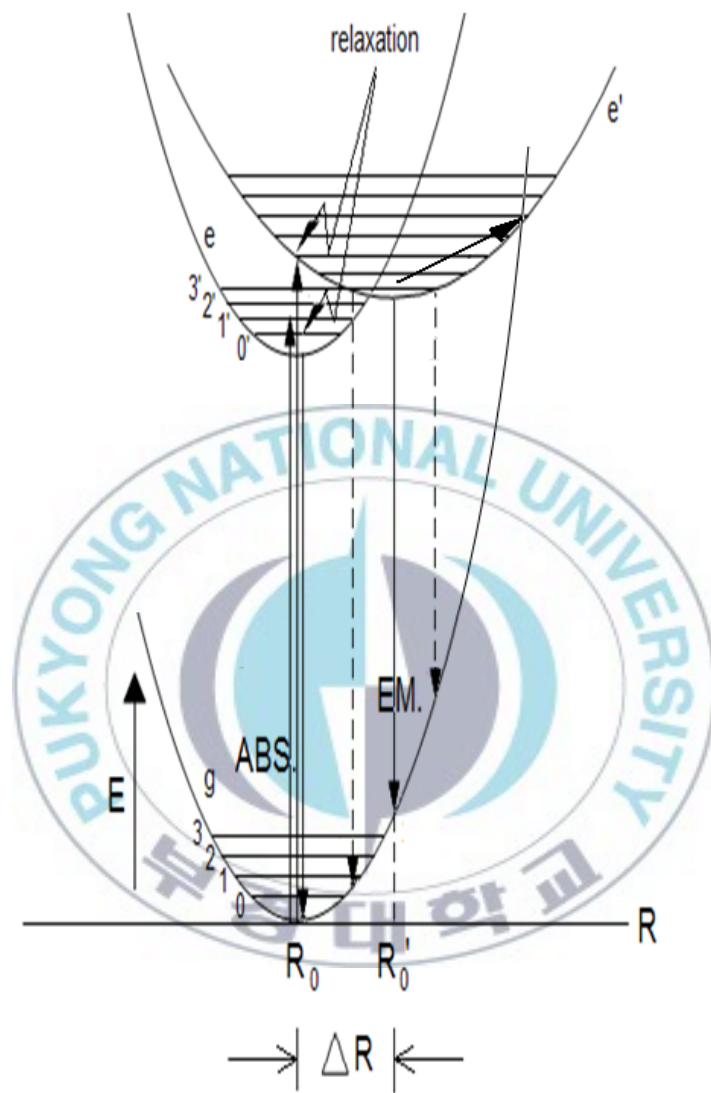


Figure 2.4 Configurational coordinate diagram. E is radiative energy. ABS is the absorption process. Em is the emission process. Parabola e is the excited state of the ground state g . e' is the excited state of another level.

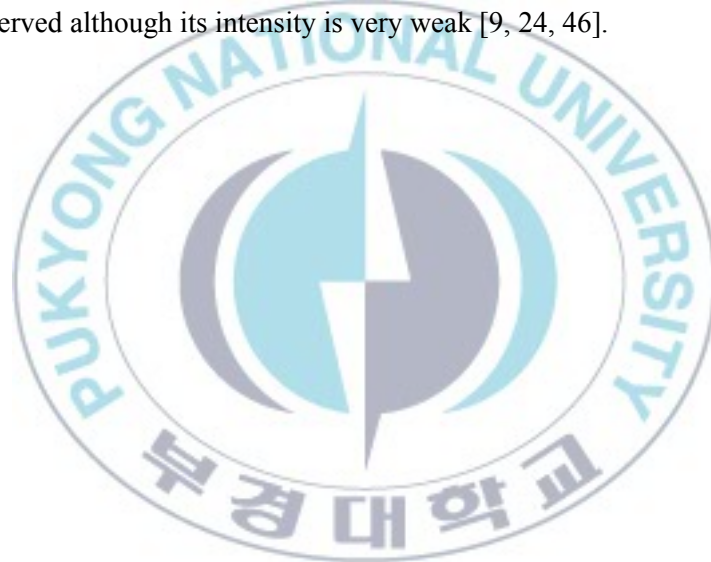
2.5 Energy levels and excited states of Eu^{2+} ions in solids

The Eu^{2+} ion is the well-known and widely used ion with the $[\text{Xe}]4f^7$ structure. Rubio [1] summarized the properties of the Eu^{2+} ion by comparing the absorption and emission spectra in different solids. The absorption spectra of Eu^{2+} ions in solids normally consist of two broad bands situated in the UV region. According to the ligand field theory, the degeneracy of the $5d$ level can be split into doubly-degenerate (E_g) and threefold-degenerate (T_{2g}) energy levels, which is due to the effect of crystal field acting on the Eu^{2+} ion. The separation between them is the well-recognized as 10 Dq splitting. For eightfold and twelvefold coordination of the ligands, the E_g level is situated at a lower energy compared with the T_{2g} level. However, in sixfold and fourfold coordination the situation is reversed [1]. Figure 2.5 is the schematic energy level diagram of the Eu^{2+} ion where the relation with the $4f$ and $5d$ levels can be observed clearly.

The intensity of these two broad band spectra is quite strong as compared to the intra- $4f$ transitions, since the transitions from the ground $4f$ state to the $4f5d$ state (hereafter, the $4f5d$ state is referred as $5d$ state) are allowed and no shielding of outer shell. The emission spectra of the Eu^{2+} ion can be obtained by excitation at either of the two absorption bands. Normally, there is only one emission band in the spectrum whose peak position depends strongly on the type of host crystal. The transition of this emission is allowed and its decay time is about 1 μs . The

luminescence color of Eu^{2+} strongly depends on the host lattice by the same factors as in that of the Ce^{3+} ion [5, 7, 45].

If the crystal field strength of the host is weak such as ionic crystals, the lowest component of the $5d$ configuration lies in such a position that the energy is higher than the excited $4f$ (referred as $4f'$ state) configuration. The excited Eu^{2+} ion also has a possibility to stay in the excited $4f$ level. Although $4f' \rightarrow 4f$ transition is parity forbidden, sharp-line emission spectra due to the $4f (^6P_{7/2}) \rightarrow 4f (^8S_{7/2})$ also can be observed although its intensity is very weak [9, 24, 46].



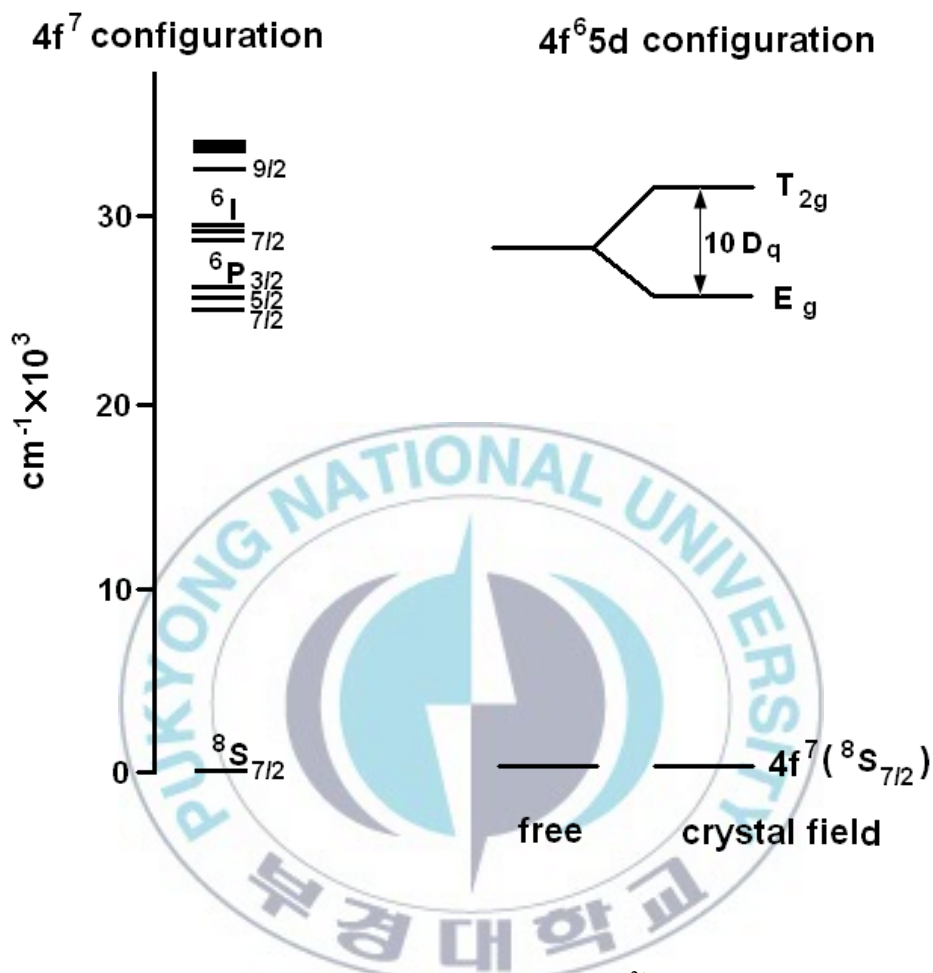


Figure 2.5 Schematic energy level diagram of the Eu^{2+} ion. Left side is the energy levels of $4f^7$ configuration. Right side is the energy levels of $4f^6 5d$ configuration. The degeneracy of the $5d$ level is split into the doubly-degenerate (E_g) and the threefold-degenerate (T_{2g}) energy levels in a crystal. $10 D_q$ is the energy gap between the T_{2g} and E_g levels.

2.6 Relaxation process of excited states in a three-level system

In a multilevel system with more than one luminescence (metastable) state the decays of lines originate from different states may be equal or different, depending on the circumstances.

Let us consider a three level system (fig. 2.6) with two metastable states, indicated by the indices 3 and 2, and a ground state 1 [47-52]. The decay rates from levels 3 and 2 are calculated using the rate equation of the population on levels 3 and 2. The change of the population of levels 3 and 2, n_3 and n_2 , is described by the rate equations,

$$\frac{dn_3}{dt} = k_3 - \frac{n_3}{\tau_3} - p_{32}n_3 + p_{23}n_2, \quad (2.6.1)$$

$$\frac{dn_2}{dt} = k_2 - \frac{n_2}{\tau_2} - p_{23}n_2 + p_{32}n_3$$

where k_3 and k_2 are the generation rates, p_{32} is the transition probability from level 3 and 2. With the assumption that the radiative decay rates ($1/\tau_3$, $1/\tau_2$) are much smaller than the lattice relaxation rates (p_{23} , p_{32}) the populations of levels 3 and 2 are described by a Boltzmann distribution, i.e.,

$$\frac{n_3}{n_2} = \frac{p_{23}}{p_{32}} = \exp\left(-\frac{\Delta E}{kT}\right) \quad (2.6.2)$$

where ΔE is the energy separation of levels 2 and 3.

Consider the radiative decay after excitation is switched off (i.e. $k_3 = k_2 = 0$). The emission spectrum from level 2 is the same as that from level 3. Therefore, the change of population is rewritten in the form

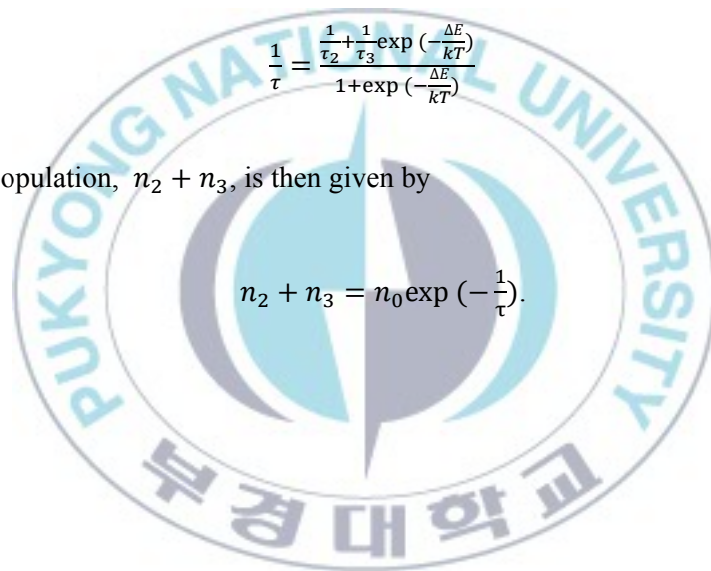
$$\frac{d(n_2+n_3)}{dt} = \frac{n_2}{\tau_2} - \frac{n_3}{\tau_3} = -\frac{n_2+n_3}{\tau} \quad (2.6.3)$$

where

$$\frac{1}{\tau} = \frac{\frac{1}{\tau_2} + \frac{1}{\tau_3} \exp\left(-\frac{\Delta E}{kT}\right)}{1 + \exp\left(-\frac{\Delta E}{kT}\right)} \quad (2.6.4)$$

The total population, $n_2 + n_3$, is then given by

$$n_2 + n_3 = n_0 \exp\left(-\frac{t}{\tau}\right). \quad (2.6.5)$$



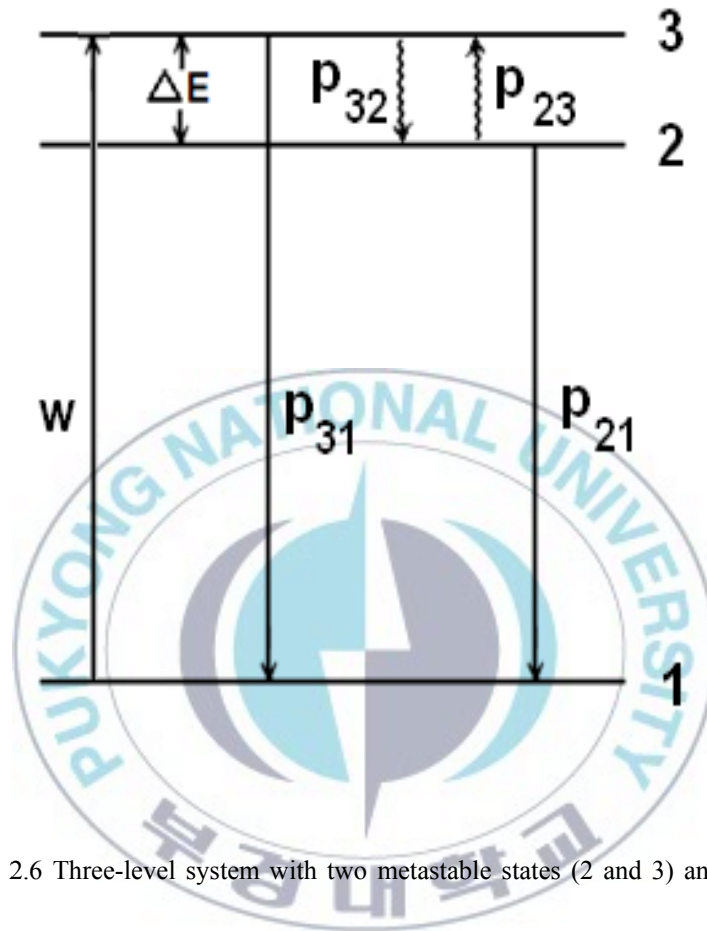


Figure 2.6 Three-level system with two metastable states (2 and 3) and one ground state (1).

2.7 Mixing of Eu^{2+} $4f$ (${}^6\text{P}_{7/2}$) and $5d$ (E_g) states by tunneling process

Quantum tunnelling refers to the quantum mechanical phenomenon where particles or energy tunnels through a barrier that it classically could not surmount. In a normal spectroscopy, the energy of $4f$ (${}^6\text{P}_{7/2}$) state has no probability to transfer energy to the $5d$ (E_g) state of Eu^{2+} at low temperature (< 70 K). Consider the barrier ΔE (fig. 2.6) is very big and separating the two states 2 ($4f$ (${}^6\text{P}_{7/2}$)) and 3 ($5d$ (E_g)) is lowered until it becomes comparable with the phonon energy, the adiabatic approximation becomes invalid and tunneling occurs between two potential minima resulting in a mixing of the excited states $4f$ (${}^6\text{P}_{7/2}$) and $5d$ (E_g) [52-54]. As a consequence, the slow decay component of band emission from $4f$ (${}^6\text{P}_{7/2}$) and $5d$ (E_g) mixing states can be observable even at very low temperature although the thermal energy is fairly small compared to the barrier height. We proceed to determine that the vibronic wavefunctions are mixed by tunneling. The tunneling splitting is calculated as an off-diagonal matrix element between $\psi_f(r, R)$ and $\psi_a(r, R)$ produced by the zero-point lattice vibration, which is equivalent to spin-orbit interaction. Here, we solve the perturbed operator including the tunneling term. The secular matrix is

$$\begin{matrix} \psi_f(r,R) \\ \psi_d(r,R) \end{matrix} \begin{bmatrix} E(f) & \delta \\ \delta & E(d) \end{bmatrix} \quad (2.7.1)$$

Therefore, the wavefunctions mixed by tunneling are given by,

$$\psi'_f(r,R) = \alpha\psi_f(r,R) + \beta\psi_d(r,R), \quad (2.7.2)$$

$$\psi'_d(r,R) = \beta\psi_f(r,R) - \alpha\psi_d(r,R)$$

where $\psi_f(r,R)$ and $\psi_d(r,R)$ are the pure vibronic wavefunctions of 4f (${}^6P_{7/2}$) and 5d (E_g) states without tunneling, and α and β are mixing coefficients which are determined by the energy separation between the 4f (${}^6P_{7/2}$) and 5d (E_g) states and the tunneling splitting. The transition probabilities from levels 4f (${}^6P_{7/2}$) and 5d (E_g) corresponding to the wavefunctions $\psi'_f(r,R)$ and $\psi'_d(r,R)$, and which are equal to the inverse of the lifetimes, are given under the assumption that $\psi_f(r,R)$ is orthogonalized to $\psi_d(r,R)$, by

$$\frac{1}{\tau_2} = \frac{\alpha^2}{\tau_f} + \frac{\beta^2}{\tau_d}, \quad (2.7.3)$$

$$\frac{1}{\tau_3} = \frac{\beta^2}{\tau_f} + \frac{\alpha^2}{\tau_d}$$

where τ_f and τ_d are the lifetimes of the pure vibronic states $\psi_f(r,R)$ and $\psi_d(r,R)$.

Equations (2.7.2) and (2.7.3) show that, at low temperatures, the slow

emission of 5d (E_g) state is mixed with the 4f (${}^6P_{7/2}$) state by tunneling process. At high temperature, occupation of the higher excited state $\psi'_d(r,R)$ occurs dominantly through the thermal activation process. In this case, the population is described by a Boltzmann distribution. The total intensities of the 4f sharp and 5d band emissions as a function of temperature are given by

$$\begin{aligned}
 I_f &= g_f I_0 \{ \alpha^2 / \tau_f + \beta^2 / \tau_f \exp[-\Delta E(T) / k_B T] \} \\
 I_d &= g_d I_0 \{ \beta^2 / \tau_d + \alpha^2 / \tau_d \exp[-\Delta E(T) / k_B T] \} \\
 \Delta E(T) &= E'_d(T) - E'_f(T)
 \end{aligned} \tag{2.7.4}$$

where g_f and g_d are degeneracy of 4f (${}^6P_{7/2}$) and 5d (E_g) states and I_0 is the constant intensity of the emission which is proportional to pumping power. The intensity ratio I_d/I_f is

$$\frac{I_d}{I_f} = \frac{g_d / \tau_d}{g_f / \tau_f} \cdot \frac{\beta^2 + \alpha^2 \exp[-\Delta E(T) / k_B T]}{\alpha^2 + \beta^2 \exp[-\Delta E(T) / k_B T]} \tag{2.7.5}$$

When the value of the reciprocal temperature goes to zero or infinity, the ratio I_d/I_f approaches $(g_d \tau_f / g_f \tau_d)$ or $(g_d \tau_f / g_f \tau_d) (\beta^2 / \alpha^2)$, respectively. The results is completely different with the classic thermal activation transition theory with the equation $I_d = I_f \exp[-\Delta E(T) / k_B T]$.

3. Experimental procedure

3.1 Preparation of single crystals

The instruction of preparation procedure for preparing LiBaF₃ single crystal is shown in figure 3.1. The detailed procedure for each step is described as follows,

(1) Pure and Eu-doped LiBaF₃ powders were prepared by solid state reaction method at high temperature. The starting ratio of LiF:BaF₂ is 3:2 and the reaction temperature is 650 °C.

(2) Phase identification and lattice parameters were measured by X-ray powder diffraction measurement (PHILIPS, X'Pert-MPD System). The result will be check by the standard JCPDs card.

(3) Determination of the melting point of LiBaF₃ powders and the heating rate temperature were carried out by differential thermo-gravimetric analysis (PERKIN-ELMER, DTA 7e) measurement. The melting point is confirmed to be around 790 °C.

(4) Then, LiBaF₃ single crystals were grown by the Czochralski method. The pulling speed is low than 1 mm/h, and the sharp of crystal is controlled by variety of rotation speed.

(5) Finally, the LiBaF₃ single crystals were cut to the standard size (3×4×5 mm).

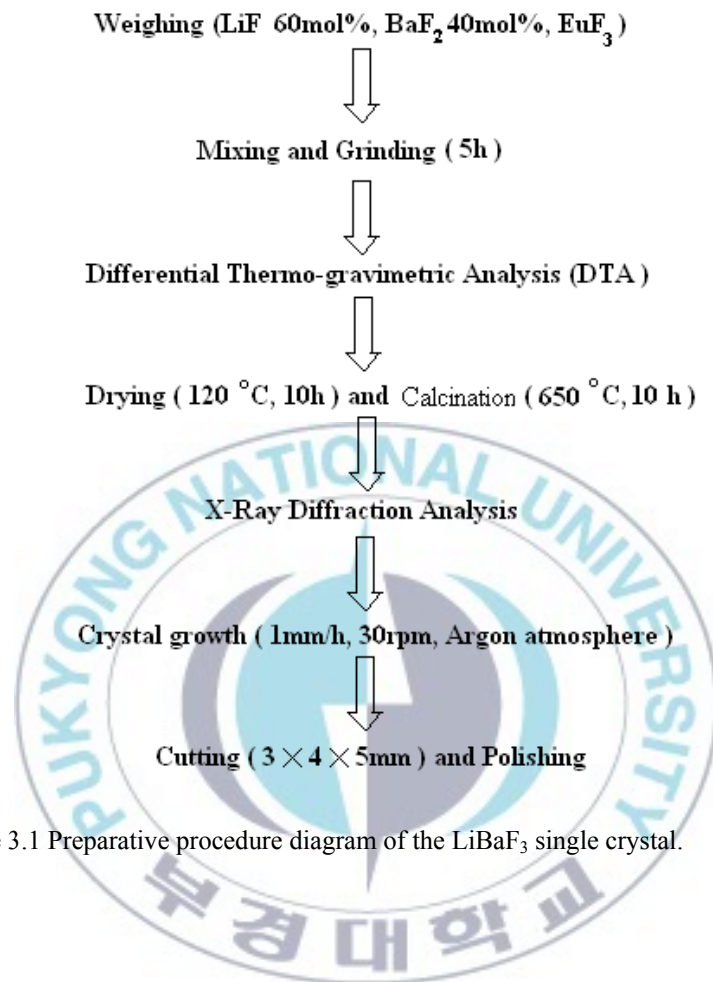


Figure 3.1 Preparative procedure diagram of the LiBaF₃ single crystal.

3.1.1 Synthesis procedure of LiBaF₃ powder

Before growing the single crystal, the as-prepared LiBaF₃ powder was synthesized by using solid state reaction. Leckebusch et al. [15] introduced a phase diagram of the LiF-BaF₂ system in figure 3.2. Region 1 is the mixture of LiF (solid) and LiBaF₃ (liquid); region 2 is LiBaF₃ (solid and liquid); 3 is LiF (solid) and LiBaF₃ (solid); 4 is BaF₂ (solid) and LiBaF₃ (liquid); 5 is LiBaF₃ (solid) and BaF₂ (solid); Curve CE is the Two-phase Curve (melting Curve). Therefore, from this diagram, we can find that LiBaF₃ melts incongruently and its single crystal must be grown from a non stoichiometric melt to avoid other phase precipitation. It is well known that, at high temperature, LiF powder is easy to volatilize. Therefore, we confirm that the approximate ratio of the LiF:BaF₂ is near 3:2 and the possible melting point of the LiBaF₃ is from 750 to 810 °C. In order to get pure LiBaF₃ powder and be convenient to dope Eu ions into the host lattice, we select 650 °C as reaction temperature for the as-prepared powder preparation.

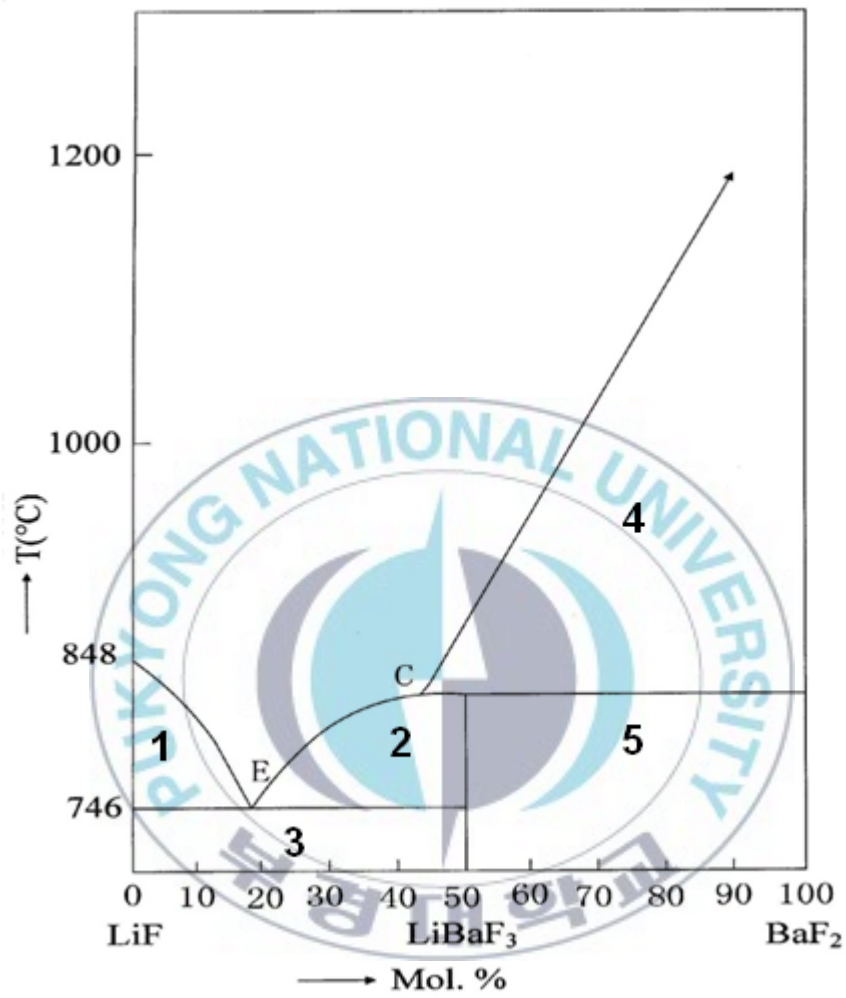
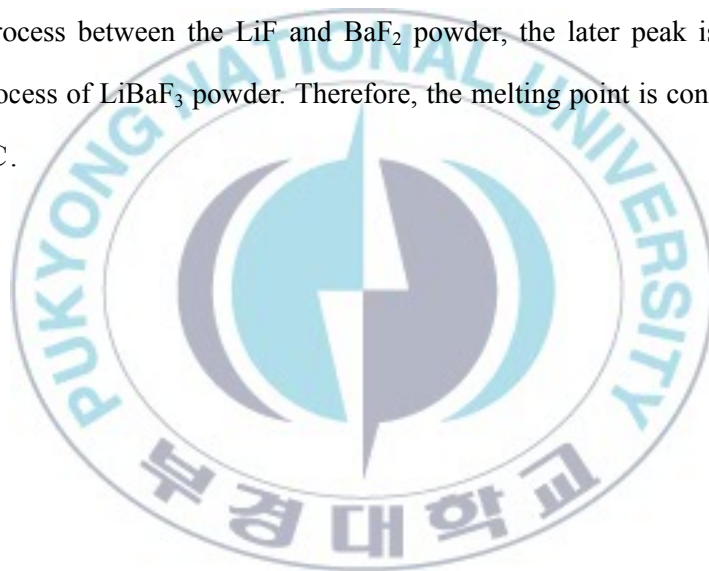


Figure 3.2 Phase diagram of the LiF-BaF₂ system [15].

The starting mole ratio of LiF (99.9%, Aldrich) and BaF₂ (99.9%, Aldrich) was fixed to be 3:2, and the concentrations of the doped EuF₃ (99.99%, Aldrich) were 0.1, 0.5, and 2 mol%. The admixture was placed in a reagent bottle. Then, the reagent bottle was laid in a ball miller in order to mix the powder completely. 10 h later, the mixed powder was obtained and measured by differential thermal analysis (DTA) analysis and the result was shown in figure 3.3. In this curve, two strong absorption peaks can be clearly observed. The former peak is due to the strong reaction process between the LiF and BaF₂ powder, the later peak is due to the melting process of LiBaF₃ powder. Therefore, the melting point is confirmed to be near 790 °C.



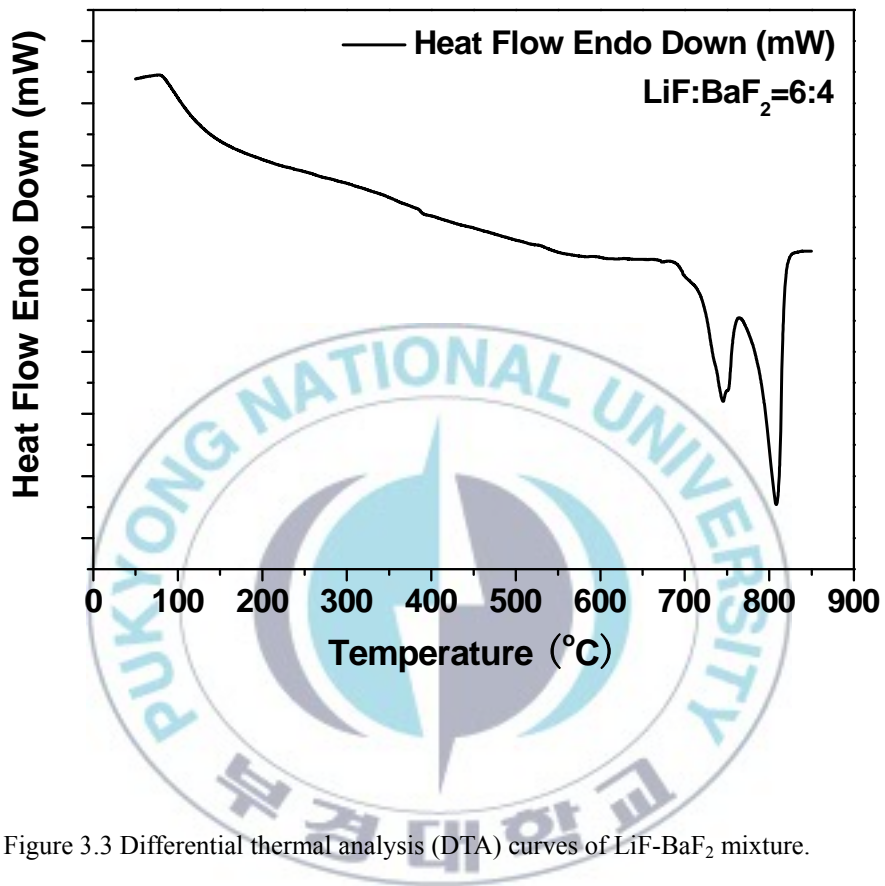


Figure 3.3 Differential thermal analysis (DTA) curves of LiF-BaF₂ mixture.

Then, the powder was loaded into a platinum crucible covered by a ceramic cover. The crucible was placed in the center of a growth chamber (fig. 3.4) and encased with some small alumina balls. Finally, the chamber was sealed and pumped to get a vacuum atmosphere. The powder must be dried at 300 °C for about 10~20 h in the chamber and the vacuum pump was always opened in this step. After drying, the powder was heated up to 650 °C at a speed of 2 °C/min. Finally, the compound was grinded and heated again to get single-phased LiBaF₃ powder.

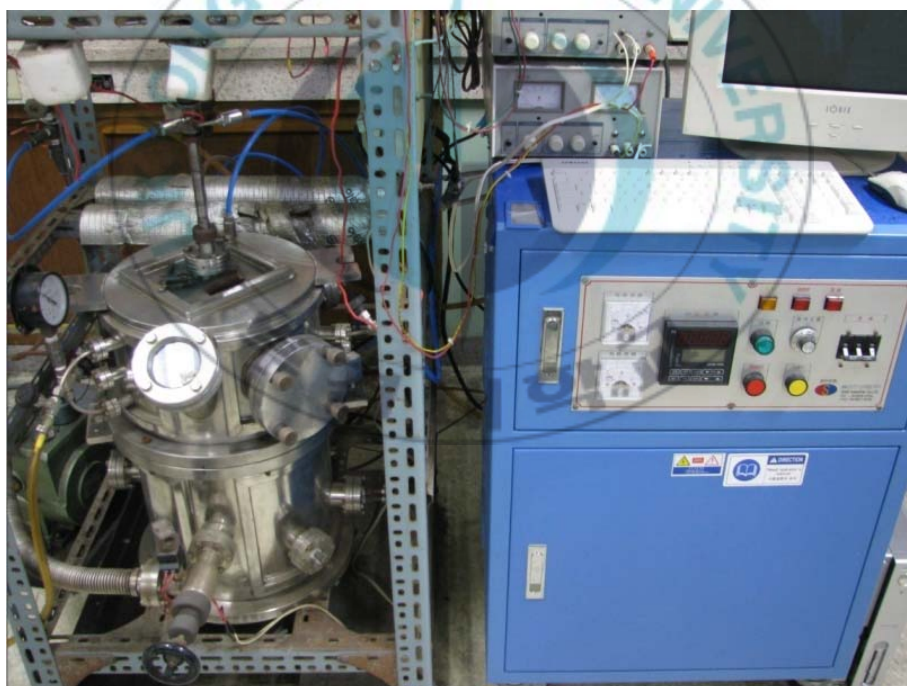
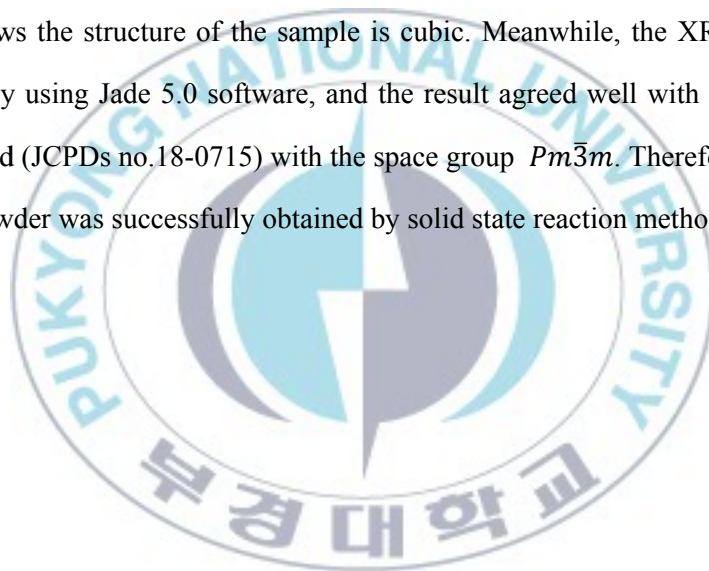


Figure 3.4 The crystal growth system for the Czochralski method.

3.1.2 X-ray diffraction analysis

Determination of the lattice parameters and phase identification of powder sample were carried out by the X-ray powder diffraction system (XRD). The data was collected by a scanning mode with a step of 0.02 degree in the 2θ range from 20 to 90 degrees. The lattice parameters a, b, and c are of the same value (3.995 Å), which shows the structure of the sample is cubic. Meanwhile, the XRD data was analyzed by using Jade 5.0 software, and the result agreed well with the standard LiBaF₃ card (JCPDs no.18-0715) with the space group $Pm\bar{3}m$. Therefore, the pure LiBaF₃ powder was successfully obtained by solid state reaction method.



3.1.3 Growth of LiBaF₃ single crystals

The Crystal growth began with pure or Eu-doped LiBaF₃ powders which were prepared by solid state reaction method. The apparatus of the Czochralski method is shown in the figure 3.5. Firstly, pure powder was placed in a large platinum crucible. Then, the crucible was put in a steel chamber and encased with some aluminum balls. Next, the chamber was closed and the pump was turned on to get a vacuum atmosphere. When the powder was heated to 300 °C, the chamber was filled with argon gas (1~1.5 kgf/cm²) and the gas was pumped out for 3 times to get a pure argon gas atmosphere. The powder was heated up to a set temperature which is 20 or 30 °C lower than melting point, then we increased the temperature to the melting point slowly (1~2 °C/min).

When the powder was melted, a small seed crystal mounted on the end of a rotating shaft was slowly lowered until it just dipped the surface of the red-hot melt. Then, the rotating rod was drawn upwards with a speed (1 mm/h). In this process, we can adjust temperature, rotation speed and pulling speed to change shape of crystal. The crystal can be grown from two to four centimeters or long, depending on the powder available in the crucible. At the end of growth process, we slowly increased the pulling speed to a high value (3 mm/h or high) to separate the crystal from hot melt. Then, we kept the crystal at a position which is 0.5~1 cm higher than the melt for 2 h to get symmetrical temperature gradient. Finally, the crystal was slowly cooled to room temperature at a speed of 1 °C/min.

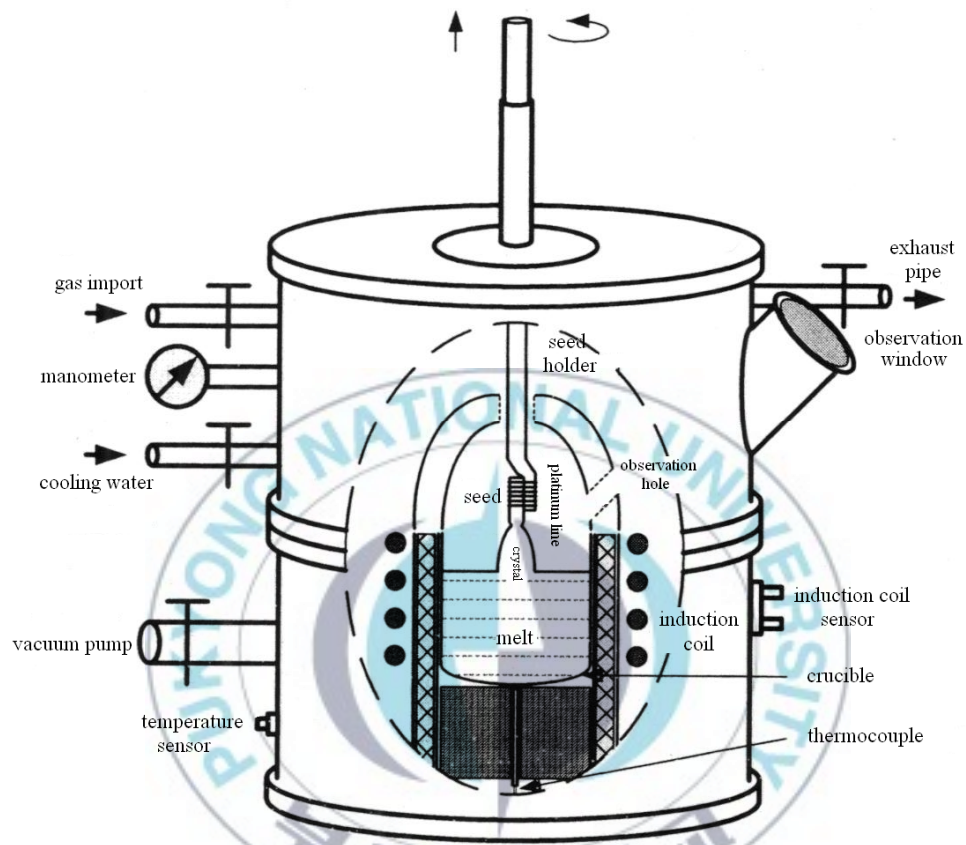


Figure 3.5 Illustration of crystal growth chamber. Pure LiBaF_3 crystal seeds were used to grow single crystals.

LiBaF_3 single crystals with three concentrations (0.1, 0.5, and 2 mol%) of Eu^{2+} ions were grown. One of the crystals is shown in figure 3.6. Although there are some small cracks inside the crystal, it is transparent and the size is enough to cut. In fact, we can choose the center part of it to test. The crystals were cut to standard samples ($3 \times 4 \times 5$ mm). Then we polished it to get good optic performance.



Figure 3.6 Photo of a LiBaF_3 single crystal.

3.2 Spectroscopic measurements

3.2.1 Measurements of absorption spectrum

Absorption spectra were measured by UV-VIS/NIR spectrophotometer (JASCO, V-670). Figure 3.7 shows a schematic diagram with the main elements of a single-beam spectrophotometer. Basically, it consists of the following elements: a light source (usually a deuterium lamp for the UV spectral range and a tungsten lamp for the VIS and IR spectral ranges) that is focused on the entrance to a monochromator, which is used to select a single frequency (wavelength) from all of those provided by the lamp source and to scan over a desired frequency range; a sample holder, followed by a light detector (usually a photomultiplier for the UV-VIS range and a SPb cell for the IR range) to measure the intensity of each monochromatic beam after traversing the sample; and finally a computer, to display and record the absorption spectrum.

The optical density is defined as $OD = \log(I_0/I)$, so that according to following equation, the absorption coefficient is determined by

$$\alpha = \frac{(OD)}{x \log e} = \frac{2.303(OD)}{x}$$

That is, by measuring the optical density and the sample thickness, the absorption coefficient can be determined.

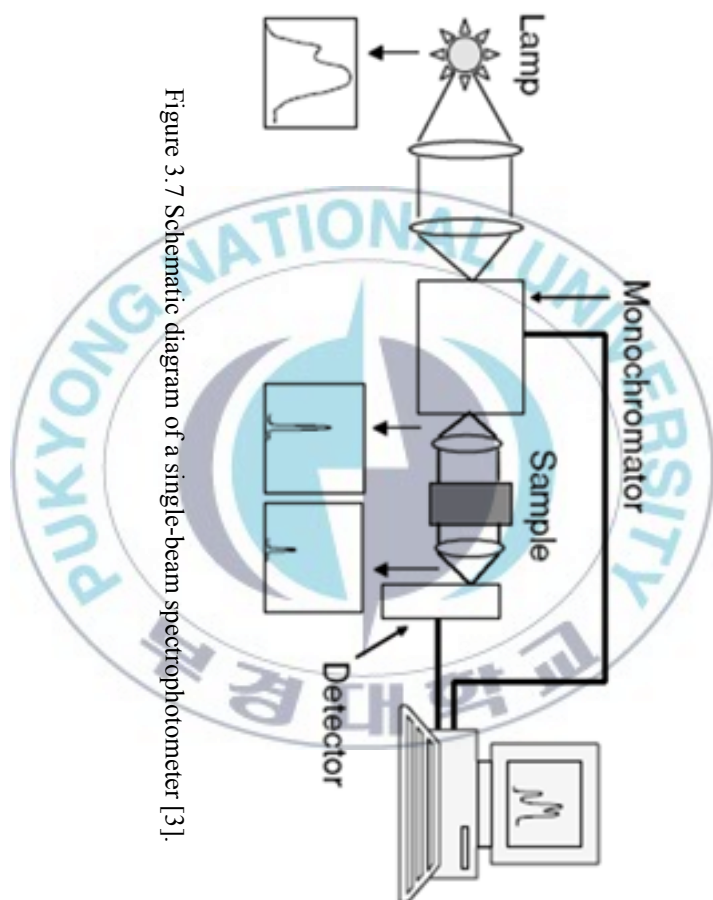


Figure 3.7 Schematic diagram of a single-beam spectrophotometer [3].

3.2.2 Luminescence excitation and emission spectra

The photoluminescence excitation and emission spectra were measured by using the spectrofluorimeter (Perkin-Elmer, LB-500). A typical experimental arrangement to measure photoluminescence spectra is sketched in figure 3.8. The sample is excited with a Xenon lamp (150 W), which is followed by a monochromator (the excitation monochromator). The emitted light is collected by a focusing lens and analyzed by means of a second monochromator (the emission monochromator), followed by a suitable detector connected to a computer. Two kinds of spectra, emission and excitation spectra can be registered: In emission spectra, the excitation wavelength is fixed and the emitted light intensity is measured at different wavelengths by scanning the emission monochromator. In excitation spectra, the emission monochromator is fixed at any emission wavelength while the excitation wavelength is scanned in a certain spectral range.

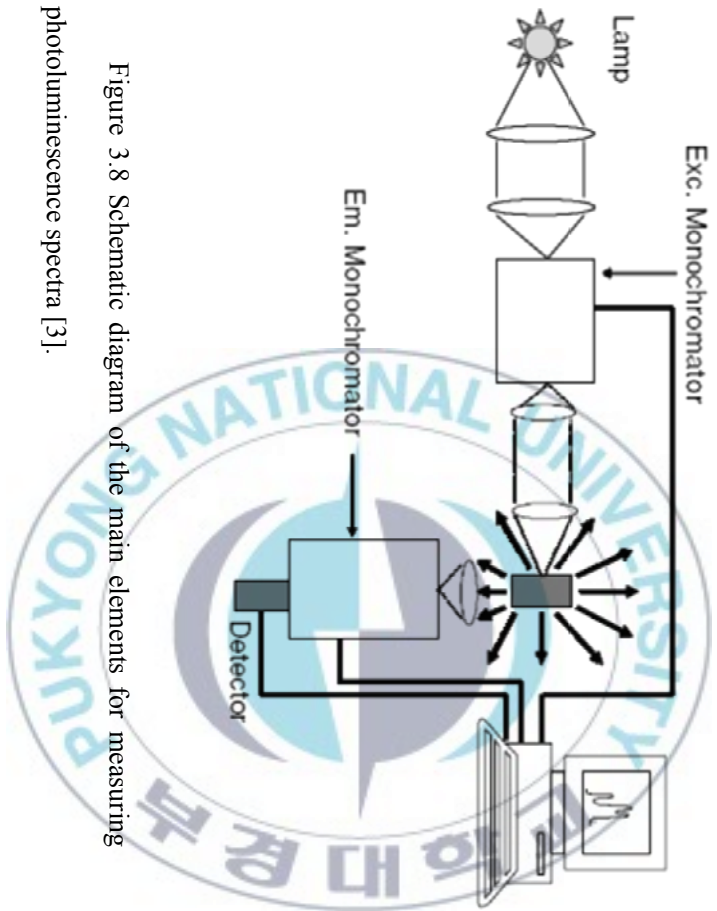


Figure 3.8 Schematic diagram of the main elements for measuring photoluminescence spectra [3].

3.2.3 Luminescence spectra and decay measurements by the pulsed laser excitation

The high resolution spectral measurements of $\text{LiBaF}_3:\text{Eu}^{2+}$ single crystals were performed by the pulsed Nd:YAG laser at 266 nm (Spectron Laser System SL802G). The samples were attached to a holder, which was placed in a helium gas flow cryostat in a variable temperature region (10-300 K) for low temperature measurements or heated by a homemade ceramic heater in the region of 300-600 K for high temperature measurements. The 266 nm laser beam with 25 mJ pulse energy was focused and crossed the polished faces of single crystals. The luminescence was dispersed by the 75 cm monochromator (Acton Research Corp. Pro-750) and multiplied by the PMT (Hamamatsu R928). The slit width of the monochromator was regulated to get suitable emission spectra. The data was displayed and recorded with the digital storage oscilloscope (LeCroy 9301). The emission spectra were measured by monitoring the luminescent intensity in different wavelengths under the pulsed laser excitation, and the lifetimes were measured in a selected wavelength after the excitation of $\text{LiBaF}_3:\text{Eu}^{2+}$ samples. The equipment diagram of this spectroscopy system is showed in figure 3.9.

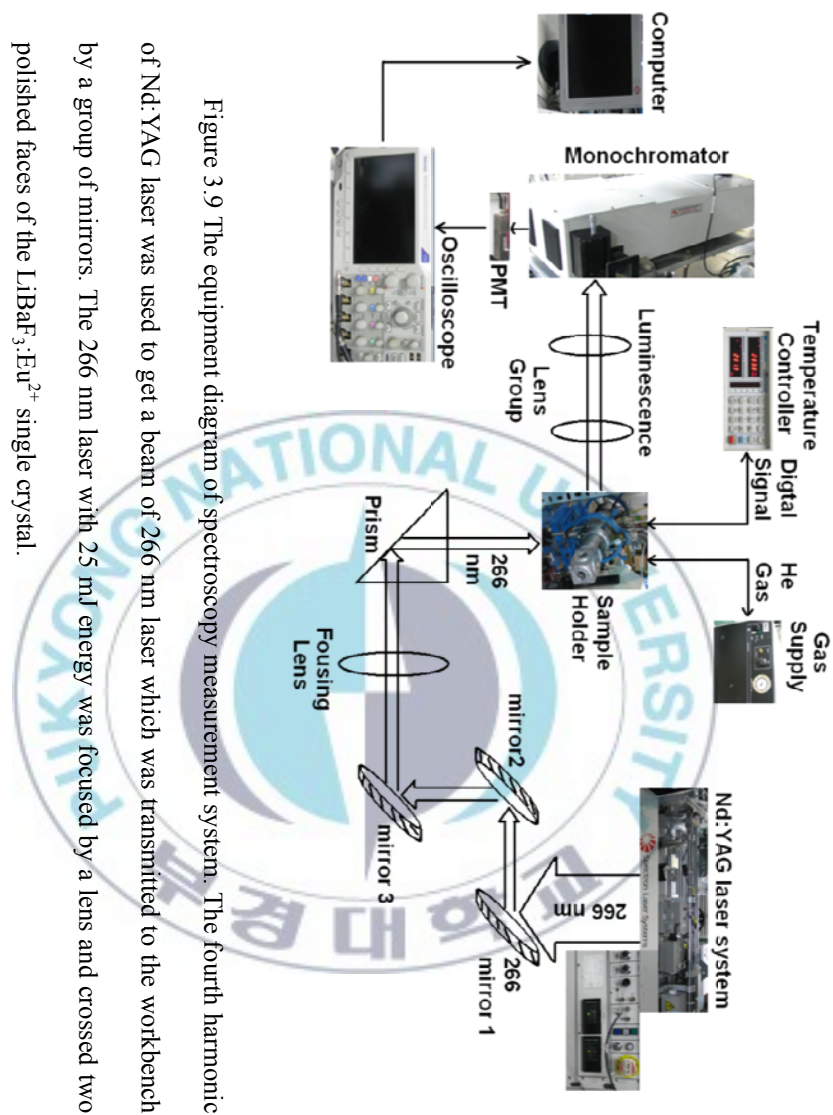


Figure 3.9 The equipment diagram of spectroscopy measurement system. The fourth harmonic of Nd:YAG laser was used to get a beam of 266 nm laser which was transmitted to the workbench by a group of mirrors. The 266 nm laser with 25 mJ energy was focused by a lens and crossed two polished faces of the $\text{LiBaF}_3:\text{Eu}^{2+}$ single crystal.

4. Results and discussion

4.1 Growth of $\text{LiBaF}_3:\text{Eu}^{2+}$ single crystals

4.1.1 Different degrees of calcinations

Before discussing the influence of calcination degree to the powder, preparation of two samples are described. The Li/Ba ratio and weight of powders were the same. The calcination temperature of them we set was 650 °C. The XRD diagrams of the calcined powders (a) and (b) are shown in figure 4.1 and figure 4.2, respectively. Sample (a) was calcined only one time and sample (b) was done two times. We can see the differences of these two figures clearly. Because of the uncompleted solid state reaction, there are two phases in sample (a). One phase is LiBaF_3 (JCPDs no. 18-0715 card) and another is BaF_2 (JCPDs no. 04-0452 card) which makes defects in the crystal. The strong diffraction intensity of BaF_2 indicates that the BaF_2 -concentration is high (figure 4.1). The peaks in figure 4.2 are in good agreement with the JCPDs no. 18-0715 card with the lattice parameter $a=0.3996$ nm. Therefore, we can conclude that the different degree of calcination is a very important factor for raw material.

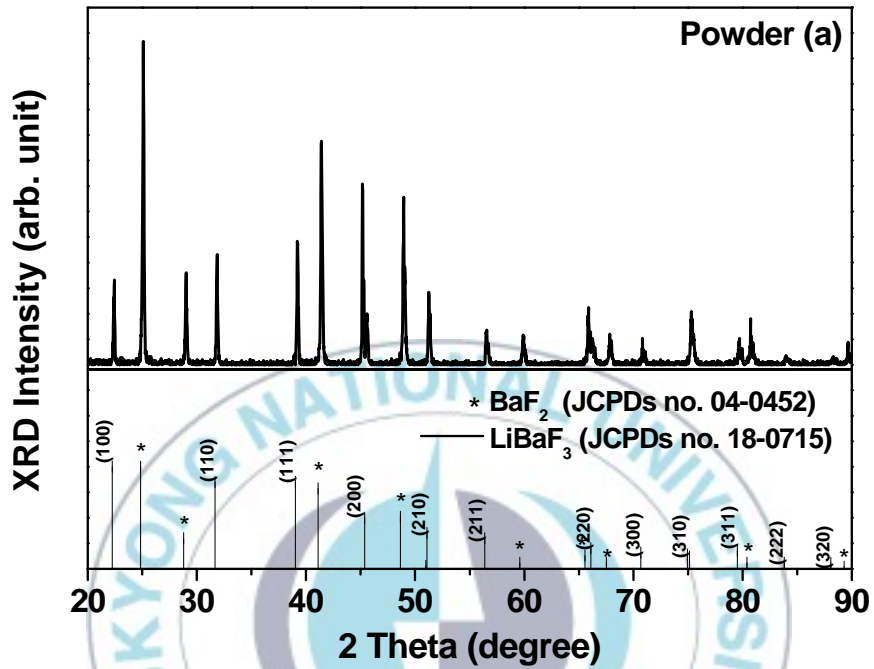


Figure 4.1 XRD diagram of the LiBaF₃ powder (a) with LiF 60 mol% after one time calcination.

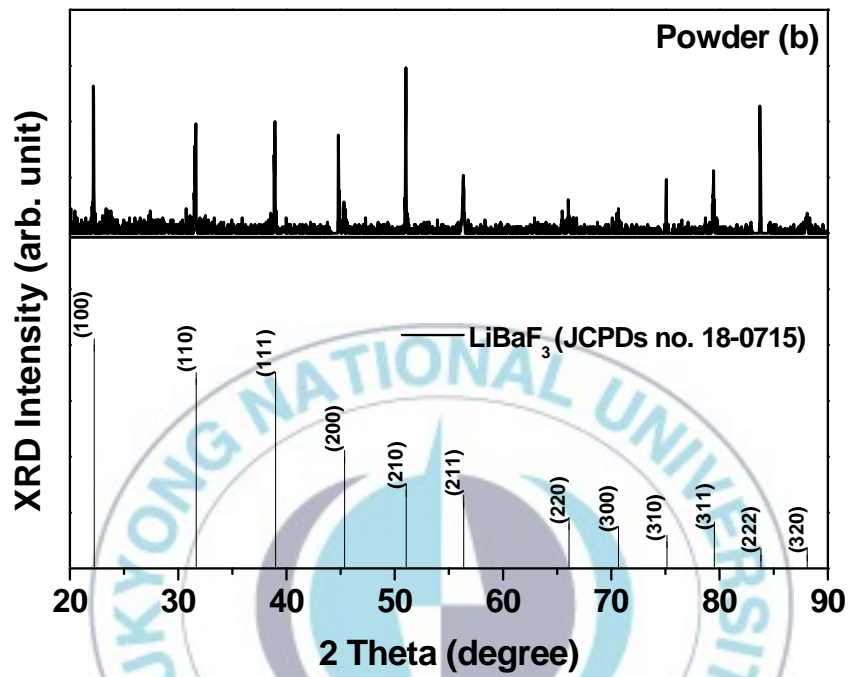


Figure 4.2 XRD diagram of the LiBaF_3 powder (b) with LiF 60 mol% after two times calcinations.

4.1.2 Results of different ratio of the LiF and BaF₂ powders

In order to compare the effect of the concentration of LiF and BaF₂ raw materials, we prepared another compound with the mole ratio of LiF/BaF₂ as 55:45. The XRD diagram is shown in figure 4.3. Also, it was calcined two times, but the component of BaF₂ is still found. For the volatility of the LiF and the incongruently meltability of LiBaF₃, the non-stoichiometric compound was prepared to avoid other phases in LiBaF₃ melt. However, it is very hard to match the mole ratio of these raw materials. According to the phase diagram of LiF-BaF₂ system, we can fix a possible ratio to do the experiment. In this case, we need to prepare different concentration mixture. Comparing the figure 4.2 and figure 4.3, we found that 60 mol% of LiF is better than 55 mol% one.

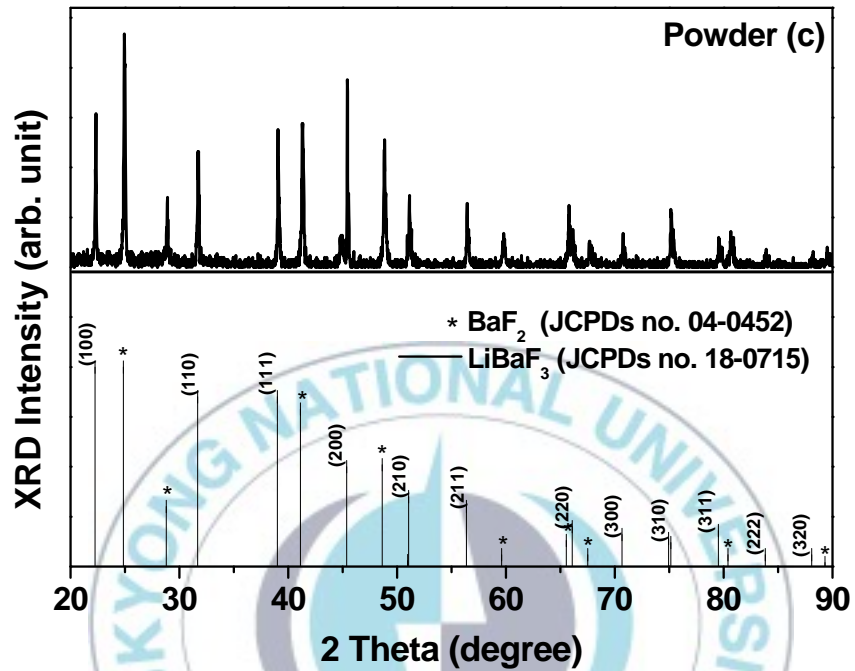


Figure 4.3 XRD diagrams of the LiBaF₃ powder (c) with LiF 55 mol% after two times calcinations.

4.1.3 The initial temperature cooling rate

Firstly, we grew the crystal with $\langle 001 \rangle$ seed with a constant rotation of 30 rpm. The initial temperature cooling rate was $-1 \text{ }^\circ\text{C/h}$. The diameter of crystal grew gradually reaching a final constant value of 16 mm. The length of it was about 15 mm. The temperature was kept for 10 h to get an equal-diameter crystal. Then, we changed the temperature rate to $-1.5 \text{ }^\circ\text{C/h}$. 5 h later we finished the process with $-2 \text{ }^\circ\text{C/h}$ to separate the crystal from the melt.

As the initial rate of temperature cooling rate was faster, the neck of the crystal was very short and wide. The increase of the weight resulted in the appearance of the cracks which affect the crystalline homogeneity and optical transmission. We also began the crystal growth with a lower cooling rate in the same condition. In this case ($-0.5 \text{ }^\circ\text{C/h}$), a better diameter control was obtained. The final constant value was 10 mm with 12 mm length. The shape of the neck was better than before. The most important is the decrease of defects. Considering the thermal condition of the chamber and the dimensions of the crucible, we have to increase the diameter of the crystal in order to get a bigger size, which needs a faster temperature cooling rate. But, this results in more defects.

4.1.4 Rotation and pulling speeds

Different rotation speeds result in different interface shapes of the growing crystal. For the LiBaF_3 single crystal grown by the Czochralski method, the solid interface becomes concave towards the melt for high rotation rate, flat for middle rate and convex for low rotation rate [16]. We can get a bigger crystal by changing the rotation speed. For different points at the face of the melt, the temperatures are different. Using faster speed might cause asymmetry of the temperature which results in more defects inside the growing crystal. But the crystal is very difficult to grow at low rotation speed. After repeating many times, we found 30-40 rpm is the best choose.

Pulling speed is also a very important factor for crystal grown by the Czochralski method. The difference of the temperature from button to top of the crucible is very big without platinum attemperator. Thus, the pulling speed we used is lower than 1 mm/h. Otherwise, the optic properties of the crystal will not be good.

4.2 Energy level structure of Eu^{2+} in LiBaF_3

4.2.1 Absorption and excitation spectra of Eu^{2+} in LiBaF_3

The absorption spectrum of the $\text{LiBaF}_3:\text{Eu}^{2+}$ single crystal obtained at ambient conditions are presented in figure 4.4 (a). Two absorption bands (dash line) peaking at 245 and 285 nm can be observed due to the best fitting of the absorption curve, which is similar with the reported excitation spectrum of $\text{LiBaF}_3:\text{Eu}^{2+}$ [9]. These two absorption bands are assigned to the allowed $4f \rightarrow 5d$ transition of Eu^{2+} ion. The $5d$ level is split into two bands, one between 225 and 280 nm and another between 280 and 350 nm due to the crystal-field splitting of the $5d$ electron. The crystal-field splitting ($10 Dq$) is about 6500 cm^{-1} which is smaller than that in oxide lattices [55].

Figure 4.4 (b) shows the excitation spectra of the $\text{LiBaF}_3:\text{Eu}^{2+}$ single crystal obtained at room temperature. The excitation spectrum has the same shape monitored at the sharp line emission or broad band luminescence, which also shows the similar pattern with the absorption spectrum presented in figure 4.4 (a). The structure in the excitation spectrum with peaks in the range 220 to 350 nm has been related to parity allowed transitions from the ground state $4f$ ($^8S_{7/2}$) to the states of the excited electronic configuration $5d$ of Eu^{2+} ion [7]. Consider the figure 4.4 (a) and (b), the absorption or excitation diagram of Eu^{2+} ion in LiBaF_3 can be obtained and shown in figure 4.5.

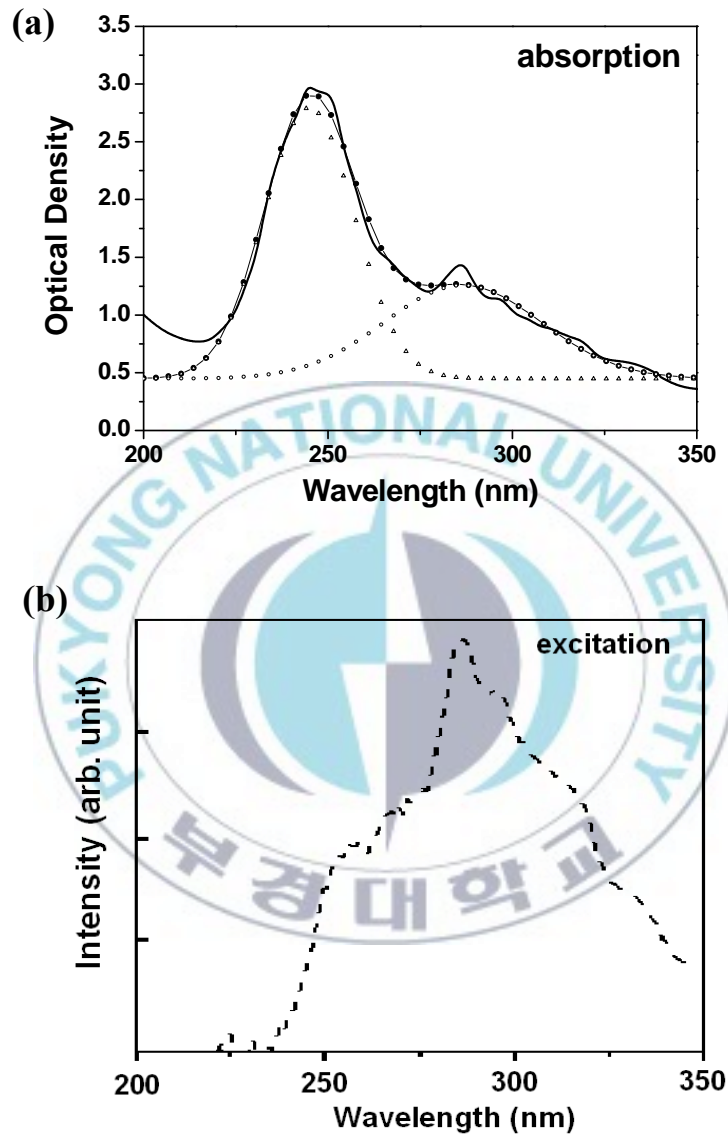


Figure 4.4 (a) Absorption spectrum (solid line) of LiBaF₃:Eu²⁺ single crystal. (b) Excitation spectrum of the Eu²⁺ obtained by monitoring at sharp line or broad band emissions.

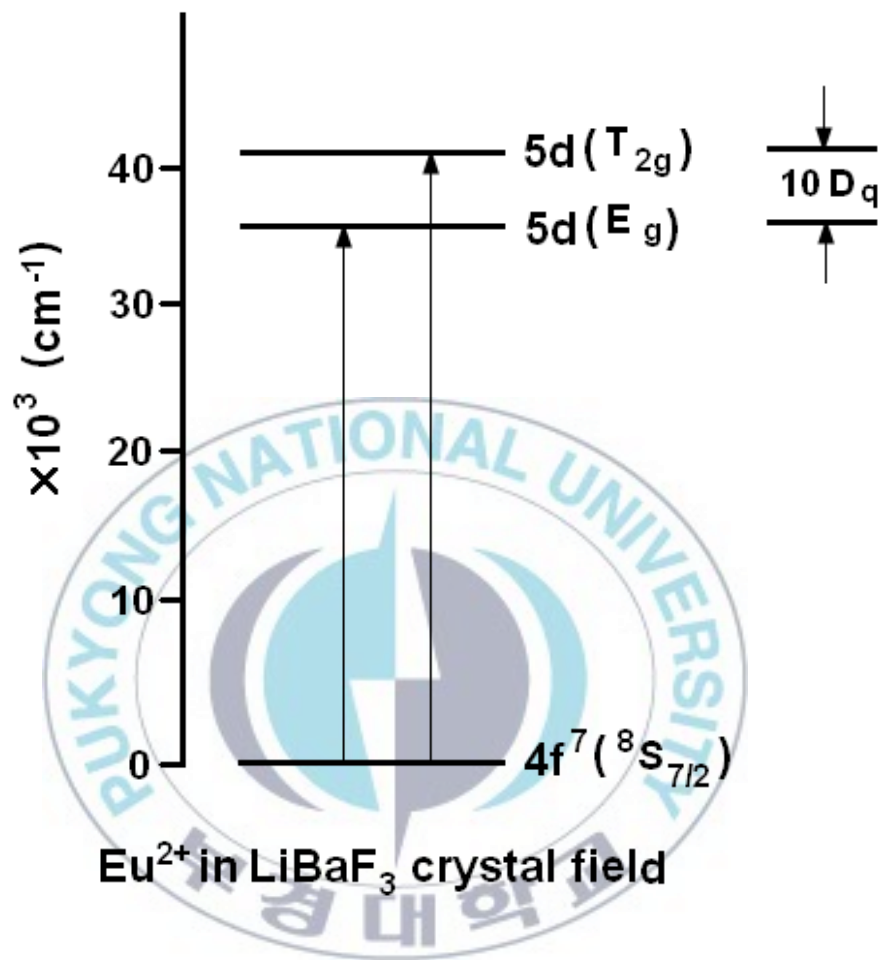


Figure 4.5 Energy level diagram of the $4f \rightarrow 5d$ transition for absorption or excitation of Eu^{2+} in LiBaF_3 .

4.2.2 Emission spectra of Eu^{2+} in LiBaF_3

Figure 4.6 (a) and (b) shows the emission spectra of the $\text{LiBaF}_3:\text{Eu}^{2+}$ single crystal obtained at room temperature (RT) and 15 K. These two spectra are obtained under excitation at 266 nm which consists of sharp lines in the spectral range 357–365 nm related to the $4f(^6P_{7/2}) \rightarrow 4f(^8S_{7/2})$ transition of the Eu^{2+} ion. In figure (a), apart from these sharp lines, a broad band emission peaked at 410 nm also can be observed. This broad band emission is attributed to transition from the excited $5d$ state to ground $4f(^6P_{7/2})$ state of Eu^{2+} [8, 44]. Depending on difference of host lattices, the $5d$ state stays at higher or lower state comparing with the $4f(^6P_{7/2})$ state. Only when the $4f(^6P_{7/2})$ level is at lower energy, sharp line emissions can be observed [9]. In figure (b), the emission at 15 K, the phonon side bands can be observed clearly around the line emission which is due to the Stokes and anti-Stokes vibrations. The intensity of the band emission is very weak and the full width at half maximum (FWHM) is narrower than room temperature because of the small thermal activation effect. Together with the absorption and excitation spectra, the energy levels of Eu^{2+} ion in LiBaF_3 can be obtained and shown in figure 4.7.

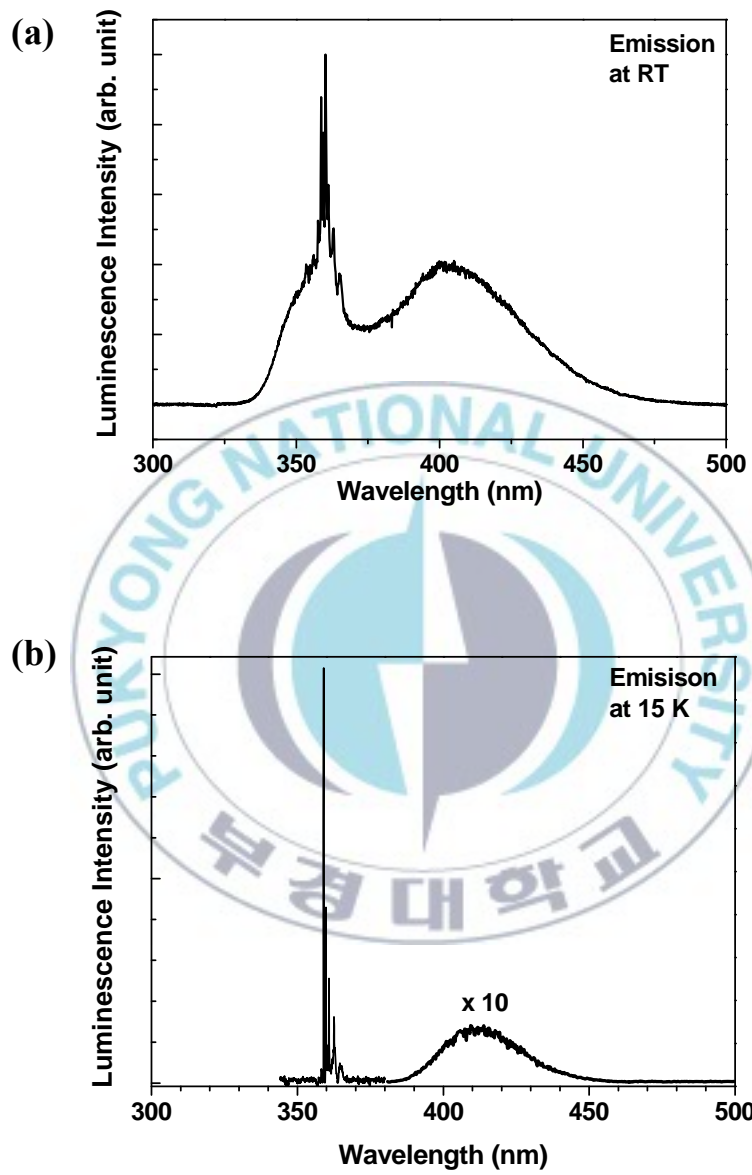


Figure 4.6 Emission spectrum of LiBaF₃:Eu²⁺ single crystal obtained at (a) RT and (b) 15 K.

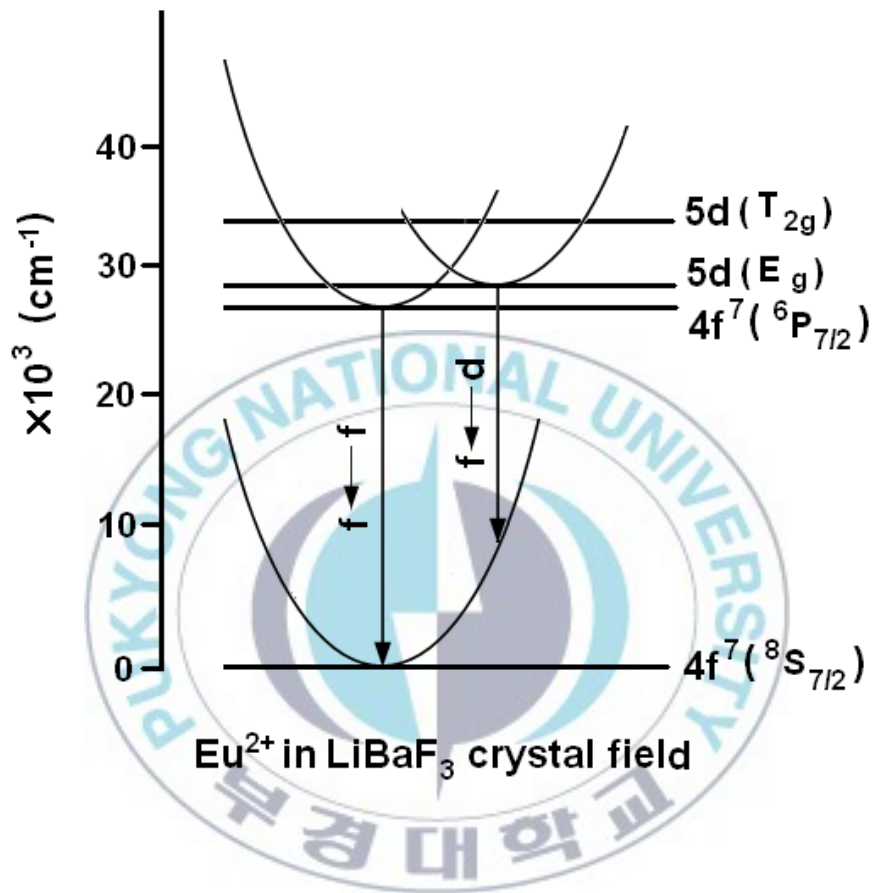


Figure 4.7 Energy levels of Eu²⁺ ion in LiBaF₃.

4.3 Zero-phonon lines and phonon side bands of the

${}^6P_{7/2} \rightarrow {}^8S_{7/2}$ transition

The high resolution emission spectrum of the ${}^6P_{7/2} \rightarrow {}^8S_{7/2}$ transition of Eu^{2+} in LiBaF_3 single crystals at 15 K is shown in the figure 4.8. In this figure, a series of line emissions and a broad band emission are clearly observed. The line emissions are confirmed related to $4f ({}^6P_{7/2}) \rightarrow 4f ({}^8S_{7/2})$ transitions and the broad band emission is attributed to the $5d \rightarrow 4f'$ transition of Eu^{2+} ion.

Figure 4.9 shows some emission lines of $\text{LiBaF}_3:\text{Eu}^{2+}$ single crystals for different Eu^{2+} concentrations. The $4f \rightarrow 4f$ transition is a parity forbidden transition, and the $4f$ orbit is well shielded by the $5d$ orbit. Therefore, the emission from the intra- $4f$ transition shows sharp lines and the position is stable in different host lattices ($\Delta R = 0$) and the strongest line peaking at 359 nm is the zero-phonon line (ZPL) of the ${}^6P_{7/2} \rightarrow {}^8S_{7/2}$ transition of Eu^{2+} in $\text{LiBaF}_3:\text{Eu}^{2+}$ single crystals [5]. The other lines in the spectral range 357–365 nm were reported to be the Stokes and anti-Stokes vibrations [9]. Moreover, with increasing Eu^{2+} -concentrations, the vibration lines are of the same pattern, which indicates the Stokes and anti-Stokes vibrations are independence of Eu^{2+} -concentration in $\text{LiBaF}_3:\text{Eu}^{2+}$ single crystals.

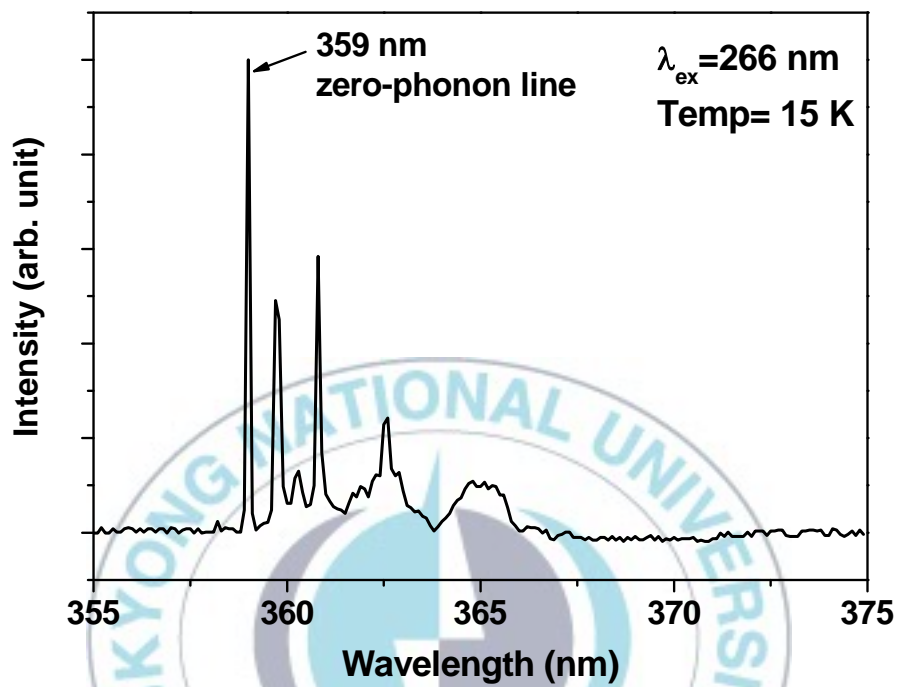


Figure 4.8 The high resolution emission spectrum of the ${}^6P_{7/2} \rightarrow {}^8S_{7/2}$ transition of Eu^{2+} in LiBaF_3 single crystal at 15 K.

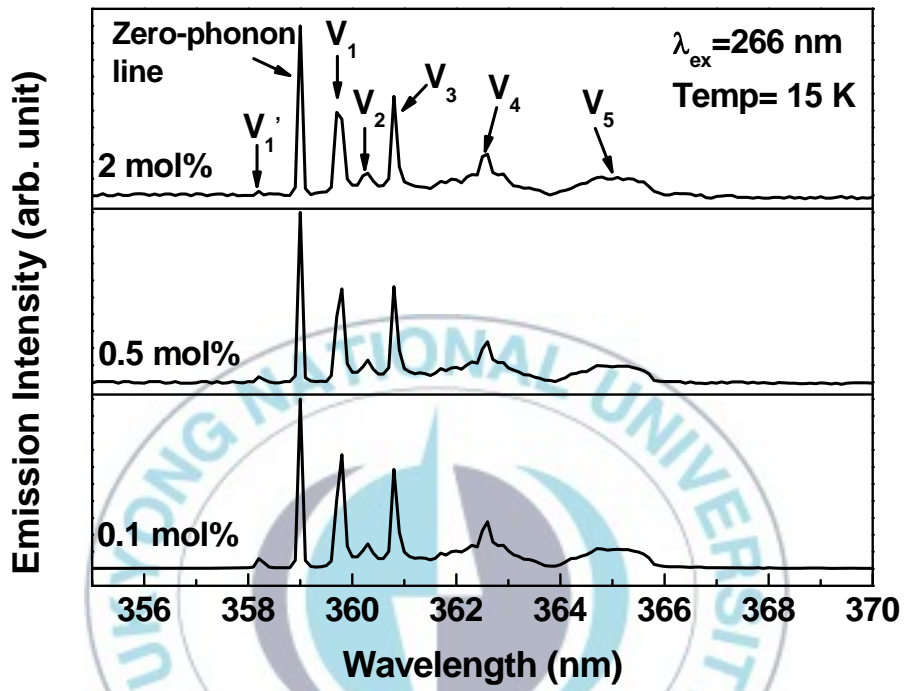


Figure 4.9 The zero-phonon line (359 nm), Stokes and anti-Stokes vibration lines of $\text{LiBaF}_3:\text{Eu}^{2+}$ single crystals.

Meijerink has reported some low resolution emission spectra in the temperature range between 4 and 150 K for detecting the anti-Stokes and Stokes vibrations near the zero-phonon line emission of Eu^{2+} in LiBaF_3 [9]. In our samples, the zero-phonon line emission, the Stokes and anti-Stokes vibrations were also clearly observed in the wavelength range between 356 and 370 nm in figures 4.10 and 4.11. The anti-Stokes ($\nu_1' - \nu_3'$) and Stokes vibrations ($\nu_1 - \nu_3$) are situated at high and low energy sides of the zero-phonon line (359 nm), respectively. With increasing temperature, these lines show a little temperature dependence and the detailed positions are shown in table 4.1.

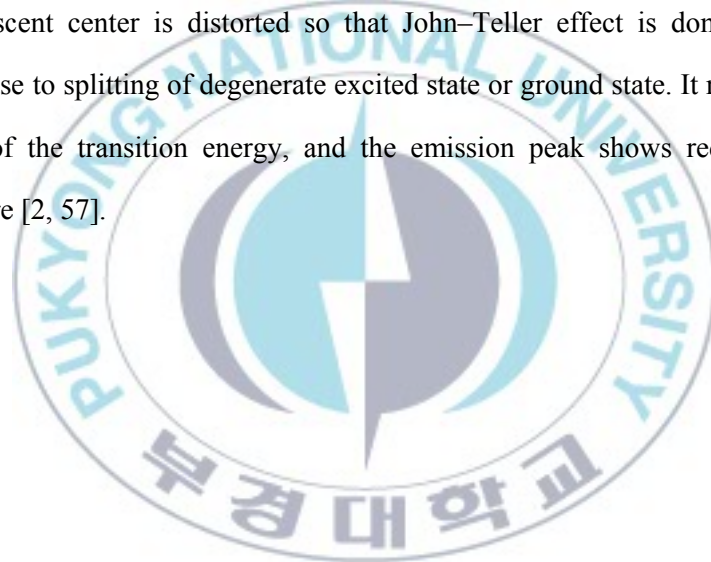
In figure 4.11, with increasing of temperature, the emission lines show a small red shift due to the effect of the crystal field and the integrated intensity of them shows a gradually variation. In the region of 10 to 150 K, the integrated intensity increases gradually and then decreases from 150 K as shown in the inset of this figure. This unusual phenomenon may have a strong relation with the $5d \rightarrow 4f$ transition and a detailed mechanism will be discussed later.

At very low temperature (< 100 K), the intensity of Stokes vibration lines are very strong and the anti-Stokes vibration lines are not easy to observe. Above 100 K, the anti-Stokes vibration lines appear at the high energy sides of the zero-phonon line. Moreover, the intensity of vibration lines show stronger at higher temperature, which is due to the stronger thermal vibration. Another interesting phenomenon is that all vibration lines and zero-phonon line have a small red shift with increasing of temperature. This behavior can be explained by the Varshni equation for temperature dependence [56]:

$$E(T) = E_0 - \frac{aT^2}{T+b} \quad (4.3.1)$$

where $E(T)$ is the energy difference between excited state and ground state at a temperature T , E_0 is the energy difference at 0 K, and a and b are fitting parameters.

At higher temperature, the bond length between a luminescent center and its ligand ions is increased, resulting in the decreased crystal field. Also the symmetry of luminescent center is distorted so that John–Teller effect is dominant. Two effects cause to splitting of degenerate excited state or ground state. It results in the decrease of the transition energy, and the emission peak shows red shift with temperature [2, 57].



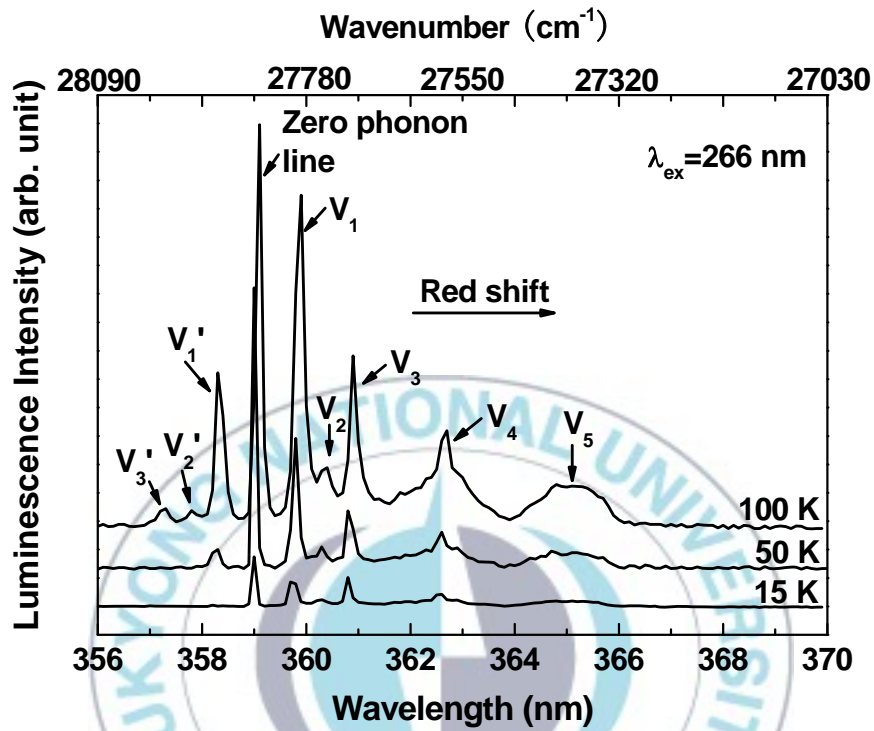


Figure 4.10 Line emission spectra of the $\text{LiBaF}_3:\text{Eu}^{2+}$ single crystal at low temperatures. The zero-phonon line was observed at 359 nm. The other peaks were due to Stokes and anti-Stokes vibrations.

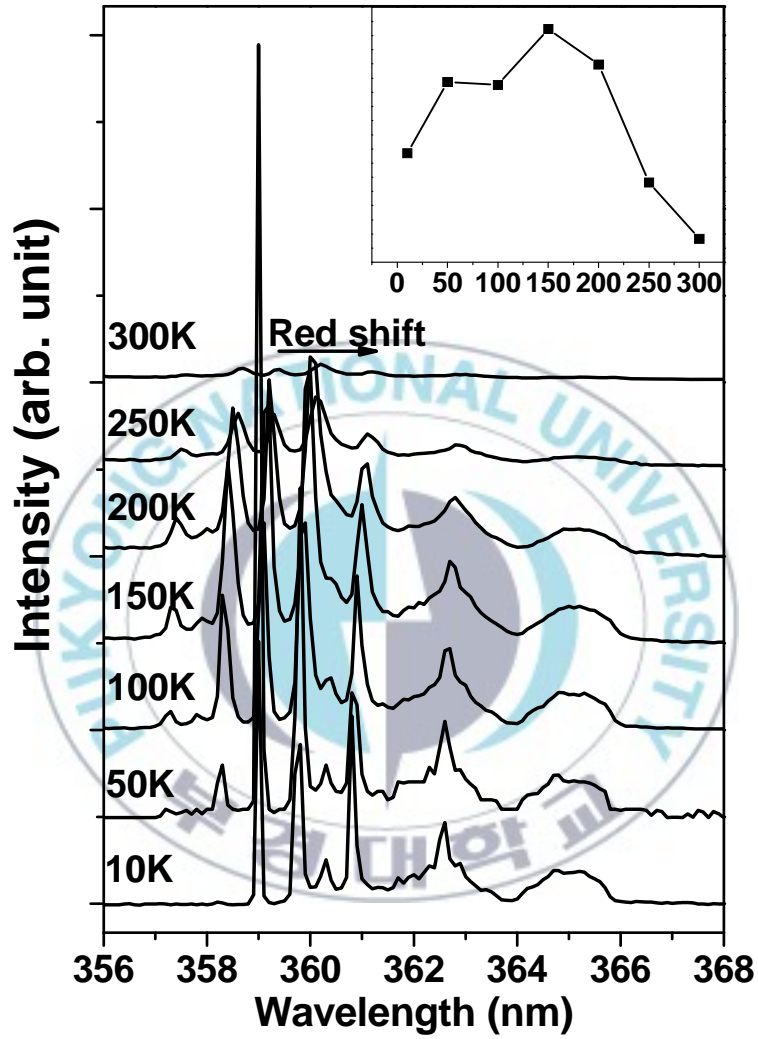


Figure 4.11 Temperature-dependent line emission spectra of $4f \rightarrow 4f$ transitions under 266 nm excitation at different temperatures and the inset is variation of their integrated intensity.

Table 4.1 The positions of the Stokes and anti-Stokes vibration lines of LiBaF₃: Eu²⁺ single crystal.

Temperature (K)	Zero-phonon line (cm ⁻¹)	Stokes vib. (cm ⁻¹)	anti-Stokes vib. (cm ⁻¹)
15	27855	$\nu_1 = 27801$	$\nu_1' = 27917$
		$\nu_2 = 27755$	-
		$\nu_3 = 27716$	-
		$\nu_4 = 27579$	-
		$\nu_5 = 27405$	-
100	27847	$\nu_1 = 27785$	$\nu_1' = 27910$
		$\nu_2 = 27745$	$\nu_2' = 27949$
		$\nu_3 = 27709$	$\nu_3' = 27989$
		$\nu_4 = 27571$	-
		$\nu_5 = 27390$	-
200	27840	$\nu_1 = 27778$	$\nu_1' = 27894$
		$\nu_3 = 27693$	$\nu_3' = 27980$
		$\nu_4 = 27563$	$\nu_4' = 28106$
		$\nu_5 = 27382$	-
300	27824	$\nu_1 = 27762$	$\nu_1' = 27886$
		$\nu_3 = 27685$	$\nu_3' = 27972$
		$\nu_4 = 27556$	$\nu_4' = 28090$
		$\nu_5 = 27375$	-

4.4 Relaxation process of excited states of Eu^{2+} in LiBaF_3

4.4.1 Thermal activation and quenching of the excited $4f$ (${}^6\text{P}_{7/2}$) and $5d$ (E_g) states in LiBaF_3

Figure 4.12 shows the decay curves of 359 nm emission of $\text{LiBaF}_3: \text{Eu}^{2+}$ single crystal between 15 and 300 K under 266 nm excitation. It is well known that the intra- $4f$ transition is parity forbidden and the $4f$ shell is shield by the $5s^25p^6$ shells. Therefore, the pattern of its emission shows sharp lines with long decay time [5]. In this figure, all the decay curves are single exponential, which indicates that the Eu^{2+} ions are isolated in the host lattice and no energy migration occurs for the Eu^{2+} -concentration under study. With increasing temperature, the decay values decrease regularly due to the thermal activation process. All decay curves can be fitted by using the equation $I=A\exp(-t/\tau)$ and their values as a function of temperature are shown in figure 4.13.

Figure 4.14 (a) shows the initial part of line emissions at 359 nm. The rise time can be observed clearly at 50 and 60 K. Figure (b) shows the calculated values of rise time. In the temperature of 10-30 K and 80-100 K, the rise time is very weak to be detected. But in 30-80 K, the rise time increases with maximum at 50 K and the values ($\sim \mu\text{s}$) are similar with the values of fast decay component of band emission which will be discussed later. Therefore, the energy transitions may occur between the excited $4f$ and $5d$ states at low temperature. Figure (c) shows the

energy transfer model between the excited $4f$ and $5d$ states. At 10 K, the line emission ($4f \rightarrow 4f$ transition) is fed only from the relaxation process from high energy level (arrow 1), and no rise time can be observed. From 30 to 80 K, the line emission is also fed from the excited $5d$ level by the thermal activation transition (arrow 2), and the rise time can be observed clearly. At 50 K, the energy back transfer occurs from the excited $4f$ to $5d$ levels (arrow 3), and the rise time of decay curve decreases again.

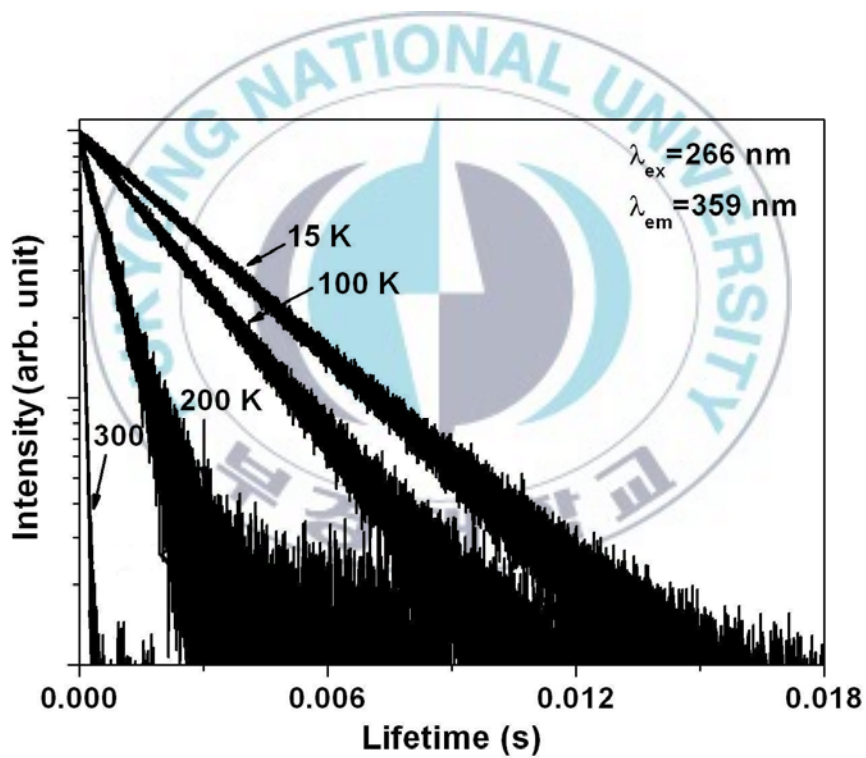


Figure 4.12 Decay curves of 359 nm emission of $\text{LiBaF}_3: \text{Eu}^{2+}$ single crystal at temperature range between 15 and 300 K under 266 nm excitation.

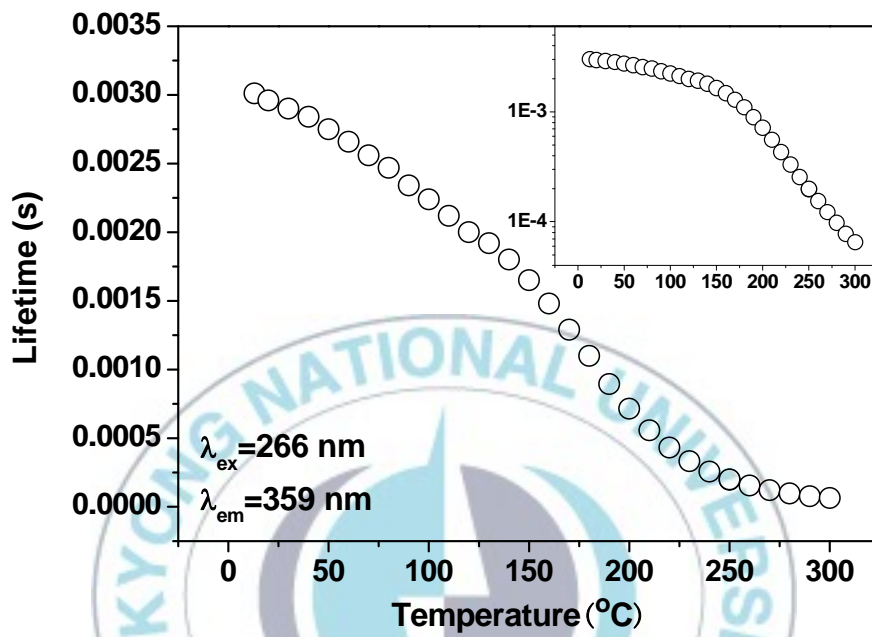
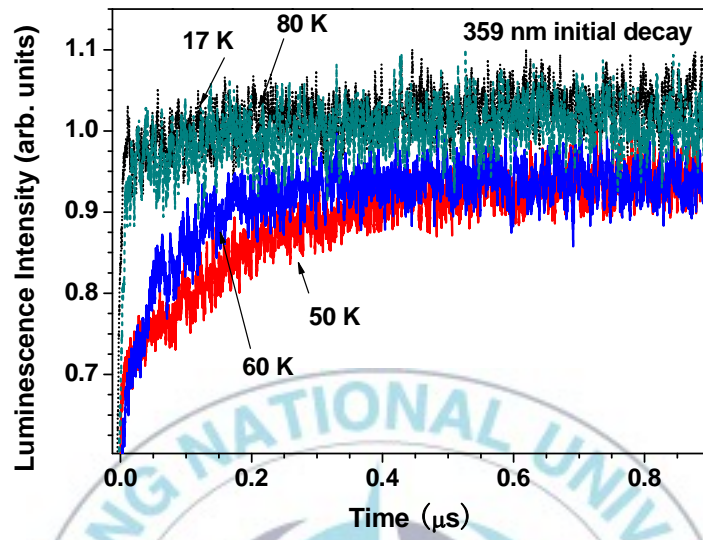
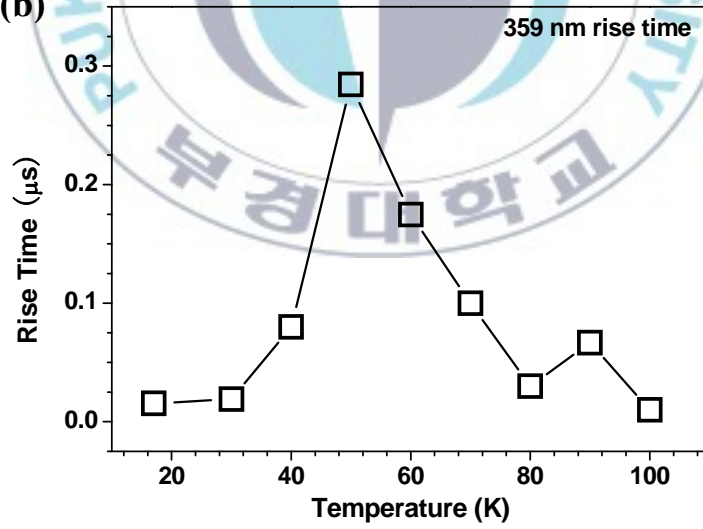


Figure 4.13 The experimental decay values of line emissions as a function of temperature. The inset is the logarithmic scale of decay values.

(a)



(b)



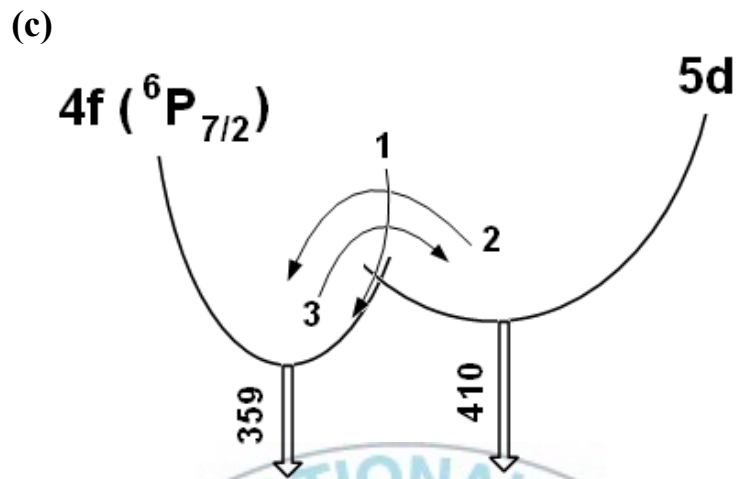


Figure 4.14 (a) rise time of line emissions at 359 nm at low temperatures. (b) the calculated values of rise time as a function of temperature. (c) the energy transfer model between the excited $4f$ and $5d$ states.

Figure 4.15 (a) and (b) show another evidence of the energy transfer and back transfer processes between the excited $4f$ and $5d$ states by thermal activation. It is compared the normalized initial and integrated intensities of emissions at 359 nm in the temperature region of 15-100 K. In this figure, the temperature dependence of initial intensity and integrated intensity are nearly the same, which means the energy lost of line emission is very small. In 15-75 K, the intensity of line emission increases due to the thermal activation transfer from the $5d$ level (arrow 1). In this temperature region 15- 70 K, thermal activation from $4f$ (${}^6P_{7/2}$) to $5d$ (E_g) is so hard because of the large energy barrier of $E1$ (bottom of ${}^6P_{7/2}$ to crossing point). This will be discussed in detail in next Chapter. At higher temperatures (in 75-100 K), the thermal activation back transfer from the excited $4f$ to $5d$ levels begins to occur and increases with temperature (arrow 2). Therefore, the initial and integrated intensities decrease.

Figures 4.16 show the integrated intensity and decay curves of line emissions at 359 nm in the temperature region of 15-300 K. In this figure, the decay value of line emissions shows good temperature quenching property, whereas the intensity shows an irregular trend as in figure 4.15 (a). In 15-65 K, the increase in intensity is explained by the energy transfer from the $5d$ state. In 70-300 K, the intensity decreases by thermal quenching. The difference between emission intensity and lifetime of 359 nm as a function of temperature is due to the very short decay time of $5d$ state. The thermal activation of $5d$ (E_g) \rightarrow $4f$ (${}^6P_{7/2}$) affects only the initial stage of 359 nm decay.

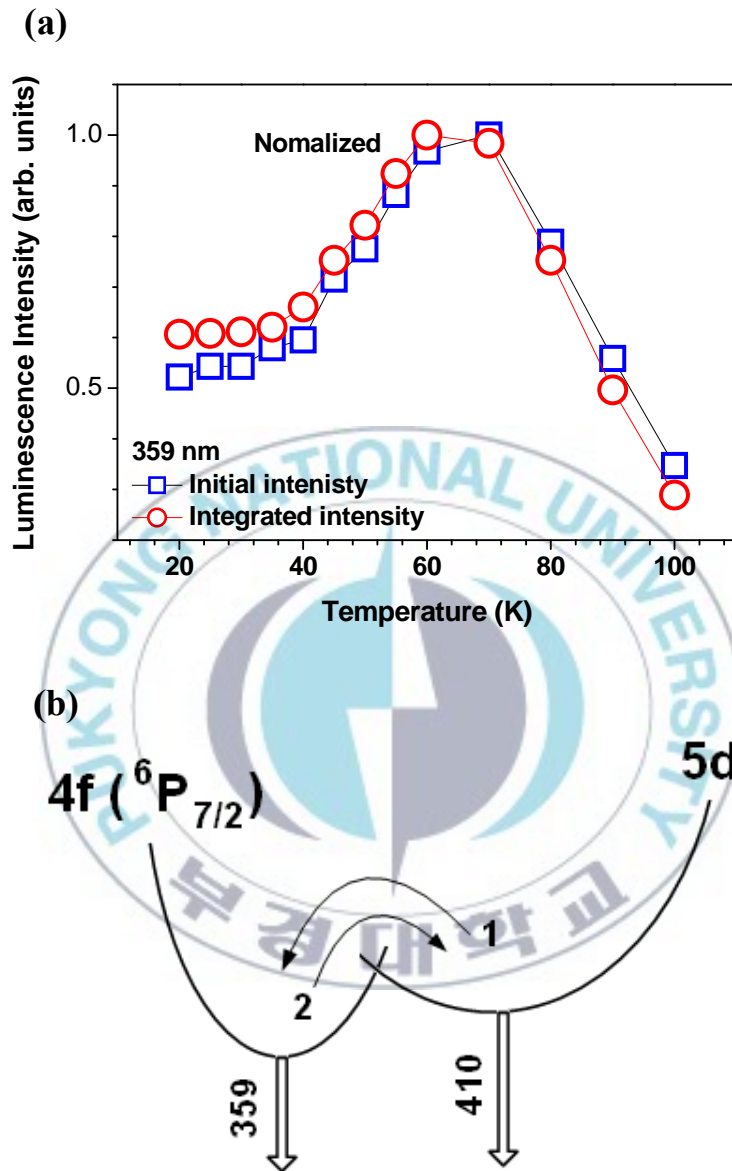


Figure 4.15 (a) The normalized initial and integrated intensities of emissions at 359 nm in the temperature region of 15-100 K. (b) The transfer model between the excited $4f$ and $5d$ states.

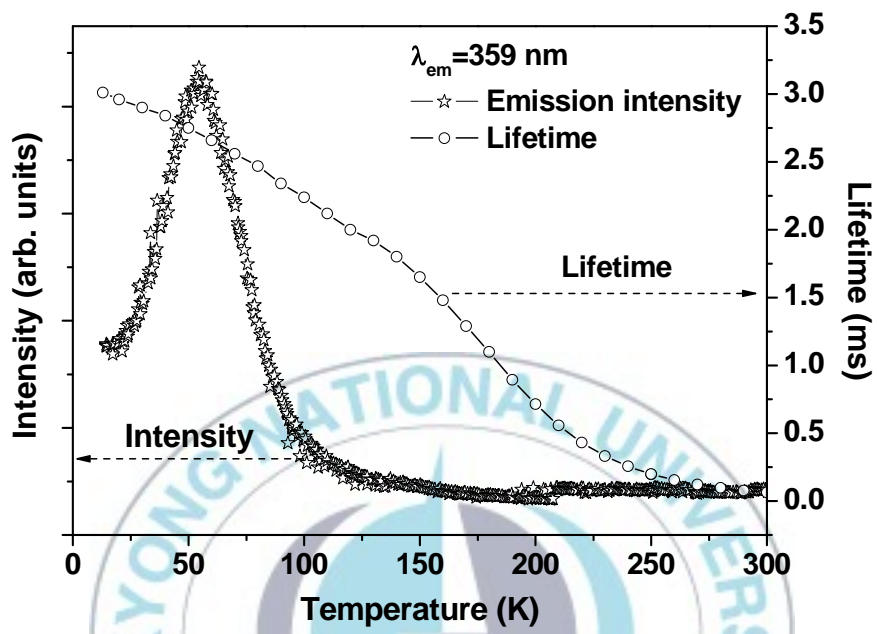


Figure 4.16 The integrated intensity and decay values of line emissions at 359 nm in the temperature region of 15-300 K.

Figure 4.17 shows the decay curves of the band emission (monitoring at 410 nm) of LiBaF₃: Eu²⁺ single crystal at temperature range between 15 and 100 K under 266 nm excitation. This emission comes from the allowed $5d \rightarrow 4f$ transition, therefore, the lifetime is very fast (< 1 us) [5]. In this figure, the decay curves are single exponential from 15 to 45 K. Above 50 K, the decay curves show tails at late time with very fast exponential decay at initial stage. The fast component is in the initial part of decay and the slow component is the long tail after fast decay. The decay with fast component can be separated from the decay curve and fitted by using the equation $I=A\exp(-t/\tau)$. With increasing temperature, the decay values of fast component decrease very fast. The values of fast decay as a function of temperature are shown in figure 4.18.

Figure 4.19 shows the integrated intensity and decay curves of fast component in 15-100 K. The intensity and decay curves are consistent well with nearly the same temperature dependence, which indicates that the fast component is ‘isolated’ with other ions. The single exponential decay curves, fast decay values and band emissions indicate the fast decay component is typical for the normal $5d \rightarrow 4f$ transition.

Figure 4.20 shows time-resolved ($t=0-0.5$ μ s) emission spectra of the fast decay component of LiBaF₃:Eu²⁺ single crystal at the temperature range between 10 and 100 K. The intensity of band emissions normally decreases with increasing temperature and no emission shift is observed. The integrated values of intensities are shown in the inset of this figure. Above 100 K, the decay of this emission is very fast and becomes weak which is hard to be detected.

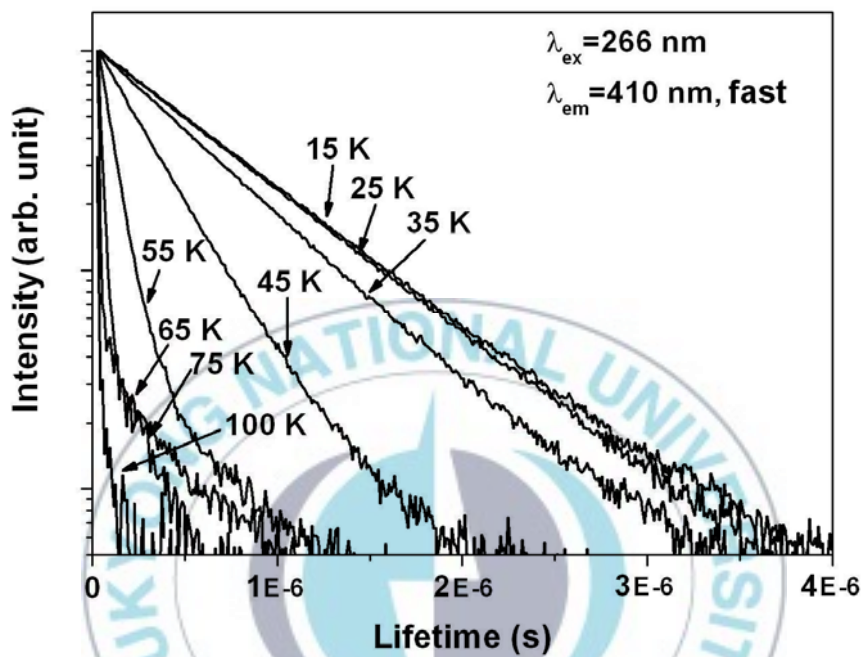


Figure 4.17 Decay curves of broad band emissions (monitoring at 410 nm) of $5d \rightarrow 4f$ transition at the temperature range between 15 and 100 K under 266 nm excitation.

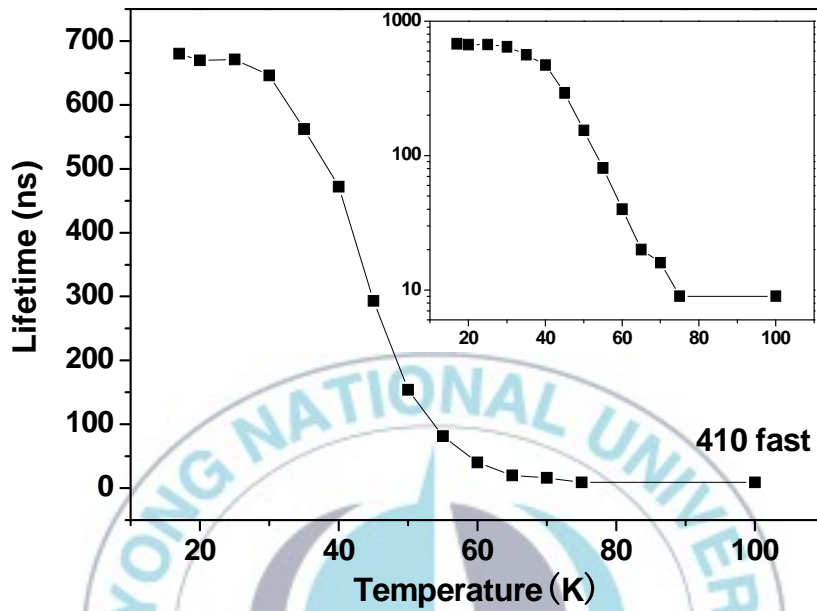


Figure 4.18 The experimental decay values of fast component as a function of temperature. The inset is the logarithmic scale of decay values.

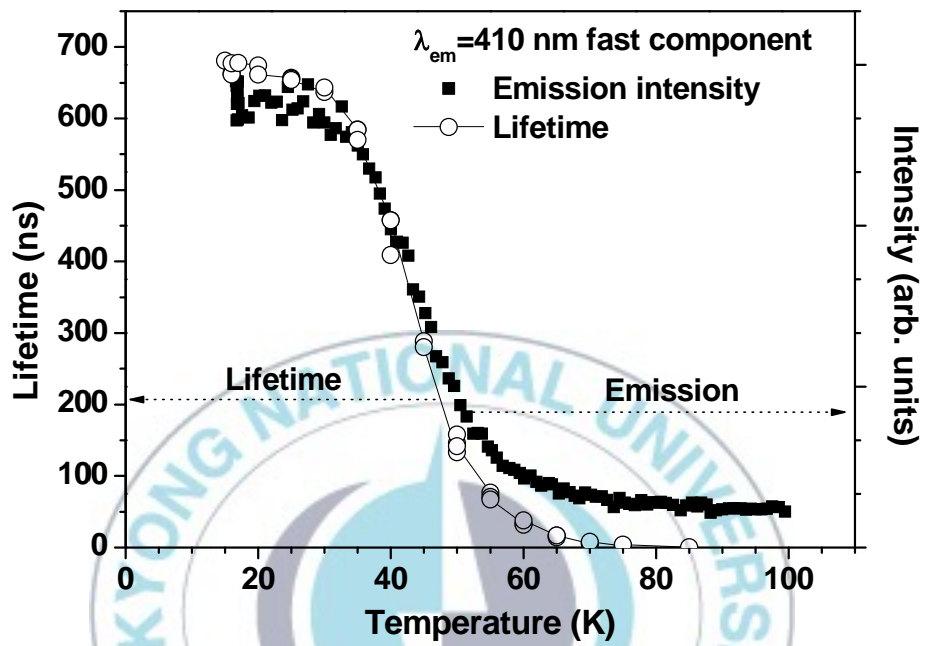


Figure 4.19 The integrated intensity and decay curves of fast component in the temperature region of 15-100 K.

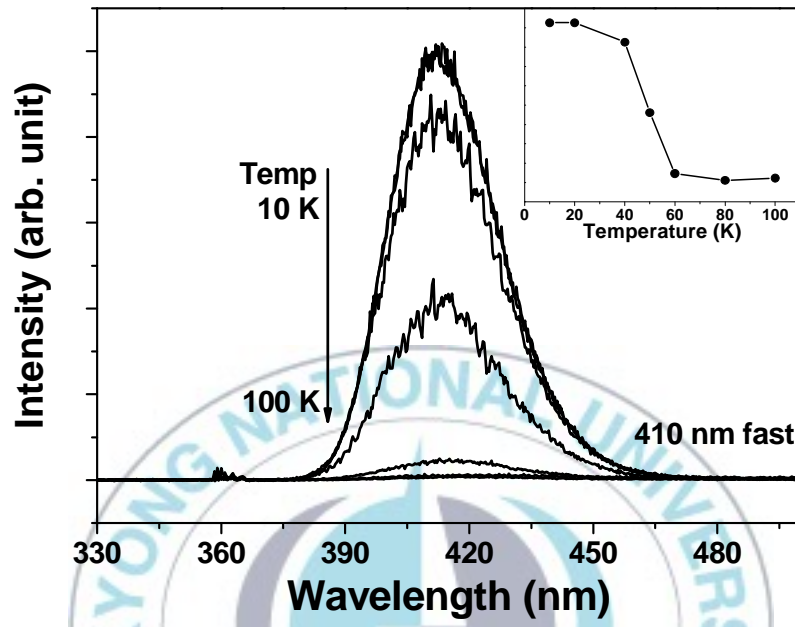


Figure 4.20 Time-resolved ($t=0-0.5 \mu\text{s}$) emission spectra with fast decay component at different temperatures and the inset is variation of their integrated intensity.

Figure 4.21 shows the decay curves of slow component of emission band (monitoring at 410 nm) at temperature range between 15 and 300 K under 266 nm excitation. The decay curves are slightly nonexponential with steep decay at initial stage. The decays of slow component were calculated by using the average lifetime equation $\tau_{\text{avg}} = \frac{\int I(t)tdt}{\int I(t)dt}$ and their values as a function of temperature is shown in figure 4.22. It is surprising that, with increasing temperature, the decay value of this slow component shows anomaly at the temperature region 50-60 K. In the region of 10-70 K, the decay decreases, then it increases slowly. A dip in the curve of decay values is observed in this figure. Generally, decay should decrease with temperature due to the effect of thermal activation process [58-60]. The decay values of slow component are similar to those of line emissions at 359 nm. It is confirmed that the decay with fast component is from the normal $5d \rightarrow 4f$ transition. The emission with slow component shows band, which is nearly the same spectral feature as $5d \rightarrow 4f$ emission. This indicates that the slow component also originates from the $5d \rightarrow 4f$ transition. Therefore, it is suggested that the anomalous decay is caused by quantum tunneling from $4f (^6P_{7/2})$ to $5d (E_g)$ levels accompanying with thermal activation process from $5d (E_g)$ to $4f (^6P_{7/2})$ levels. This result will be discussed in next Chapter.

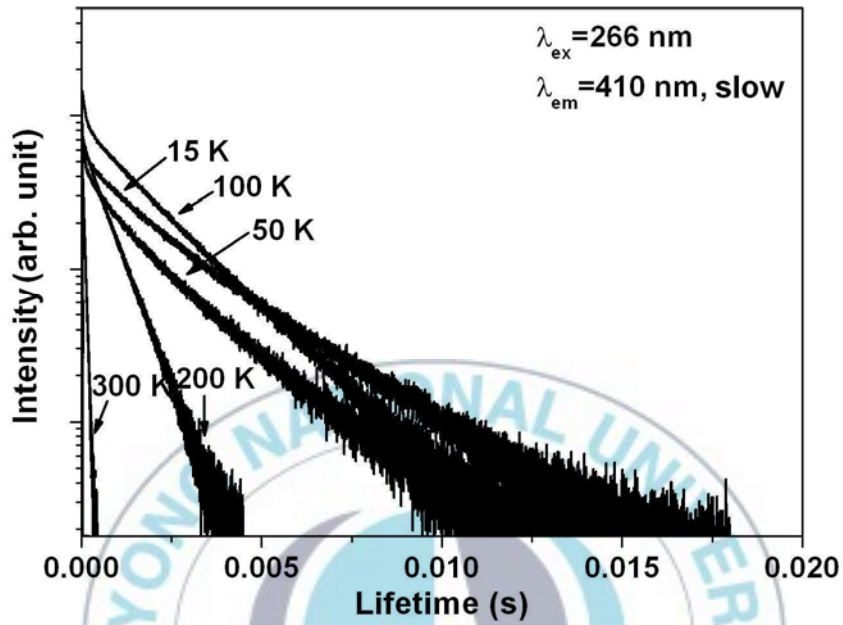


Figure 4.21 Decay curves of slow component of emission band (monitoring at 410 nm) of LiBaF₃: Eu²⁺ single crystal in the temperature range between 15 and 300 K under 266 nm excitation.

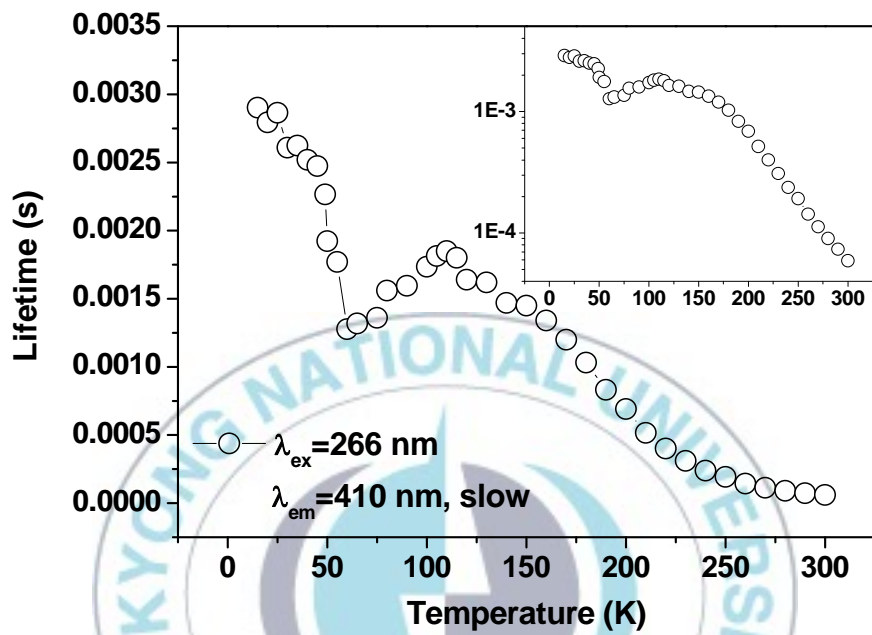


Figure 4.22 The calculated decay values of slow component as a function of temperature. The inset is the logarithmic scale of decay values.

The 410 nm band emission exhibits two components, i.e. fast and slow components. Therefore, the slow decay component is attached as a tail of the fast component due to the slow decay of 359 nm emission and time delay of the energy transfer from $4f \rightarrow 5d$ state. If this assumption is correct, the decay curve of band emission combining with fast and slow component should be well fitted by following equation,

$$I(t) = I_{0,fast}(t)\exp(-t/\tau_{fast}) + I_{0,slow}(t)\exp(-t/\tau_{slow}) \quad (4.4.1)$$

where the total intensity $I(t)$ of this emission consists of two part $I_{fast}(t)$ and $I_{slow}(t)$, respectively. $I_{0,fast}(t)$ and $I_{0,slow}(t)$ are the initial intensity of emissions with fast and slow lifetimes.

Figure 4.23 shows the fitting of mixed decay curves with fast and slow components of band emission at 410 nm at 20 K. A best fit is obtained by using equation 4.4.1, and the result shows that the fitting values for fast and slow components are 588 ns and 2.4 ms, respectively. This result also matches well with the decays of $5d \rightarrow 4f$ and $4f \rightarrow 4f$ transitions, which shows that the band emission with slow decay is really from the energy back transfer of the excited $4f$ state. However, in this figure, the fitting of the slow decay part is not very well in the initial stage indicating slightly nonexponential decay. It is assumed that the wavefunctions of $4f$ (${}^6P_{7/2}$) and $5d$ (E_g) states are mixed by tunneling process.

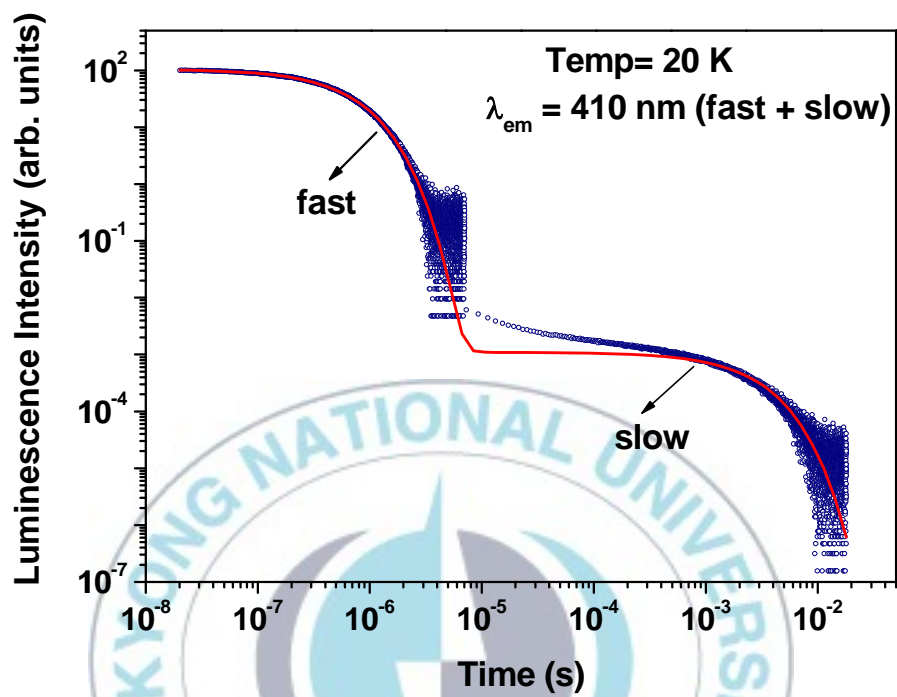


Figure 4.23 Mixed decay curves with fast and slow components of band emission at 410 nm at 20 K. Solid line is the best fitting for the equation 4.4.1.

4.4.2 Calculations of energy barriers E1 and E2

The decay of band emissions with fast and slow components indicate that the energy transfer and back transfer process between the $4f$ (${}^6P_{7/2}$) and $5d$ (E_g) states of Eu^{2+} in LiBaF_3 single crystal. Considering the spectra and decays of line and band emissions between 15 and 300 K, a configurational coordinate diagram of Eu^{2+} was built in figure 4.24. E1 is the energy barrier between the excited $4f$ and cross point of two parabolas, while E2 is the energy barrier between the $5d$ and cross point of two parabolas. Under the excitation at 266 nm, the excited Eu^{2+} ions firstly relax to the cross point between the excited $4f$ and $5d$ states. Then, the energy is divided into two parts. The part goes through the parabola to the lowest level of the $5d$ state. Then, a band emission occurs and the excited Eu^{2+} ion returns to the bottom of the ground state (P_d). The other part for the energy go back to the ground state is the excited Eu^{2+} ions relaxed to the excited $4f$ state from the cross point with low probability (P_f). Then, the line emission from the excited $4f$ state to the ground state occurs. The decay curves of these two transitions should be single exponential except for some interactions.

The rise time of line emissions and the non-exponential decay of band transitions with fast and slow components at low temperature give a strong evidence of the interactions between $4f$ (${}^6P_{7/2}$) and $5d$ (E_g) states. In figure 4.24, the excited $4f$ and $5d$ levels are separated by two energy barriers E1 and E2. After the removal of an externally applied perturbing influence (i.e. without quantum

tunneling process and with only thermal activation process), the two sets of configurations are therefore only accessible to each other by two competing relaxation ways: energy transfer and energy back transfer processes (W_{df} and W_{fd}).

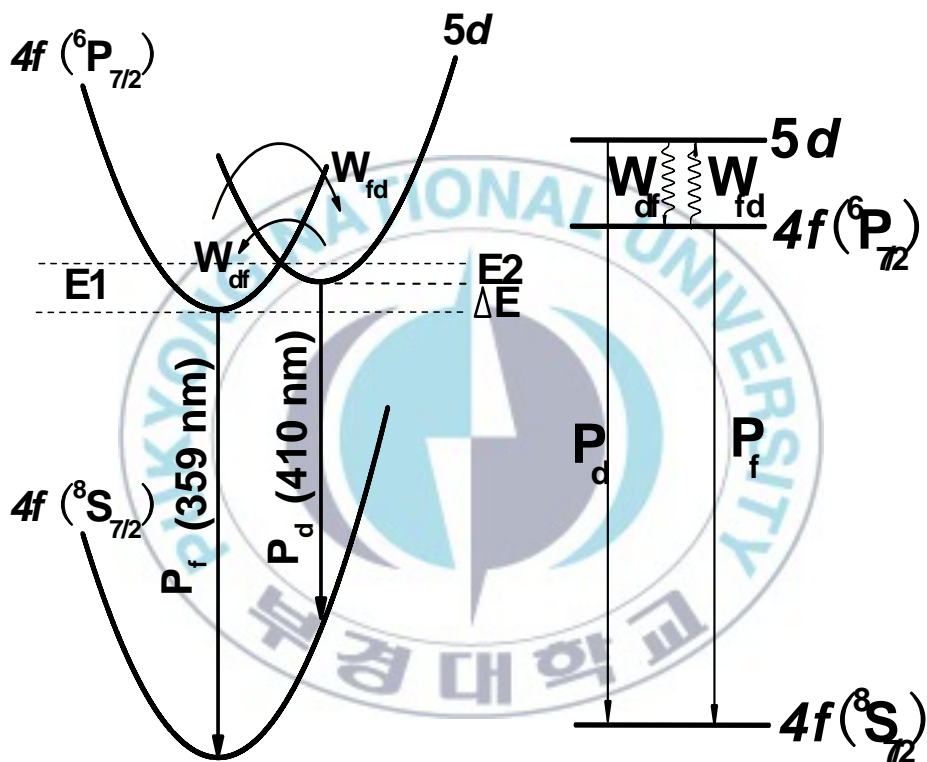


Figure 4.24 Configurational coordinate diagram of the $\text{LiBaF}_3:\text{Eu}^{2+}$ single crystal. ΔE is the energy difference between the excited $4f$ and $5d$ levels. P_d , P_f , W_{df} , and W_{fd} are the radiative and nonradiative probabilities between the $5d$ level and excited $4f$ level, respectively.

When the energy transfer and back transfer processes between the excited $4f$ and $5d$ states are established, these two states play a role of luminescence quenching state to each other. The quenching process of one emission is described by the form [60]

$$\tau_{\text{exp}}^{-1} = \tau_0^{-1} + Ke^{-E/kT} \quad (4.4.2)$$

where τ_0 is the intrinsic lifetime of the emission, K is the nonradiative rate factor, and E is the activation energy of nonradiative recombination.

Figure 4.25 (a) and 4.26 (a) show the best-fit of decay of line emission and band emission with fast component using the equation 4.4.2. The best-fit describes the main feature of the temperature dependence. The fitting parameters are obtained to be $\tau_0=3$ ms, $\Delta E=800$ cm^{-1} and $\tau_0=690$ ns, $\Delta E=350$ cm^{-1} for line and band emissions, respectively. Therefore, the energy barriers E_1 and E_2 for corresponding transitions $4f \rightarrow 4f$ and $5d \rightarrow 4f$ are 800 and 350 cm^{-1} , respectively. The energy difference between the excited $4f$ and $5d$ states are $E_1 - E_2 = 450$ cm^{-1} .

Consider the nonradiative transitions between the excited $4f$ and $5d$ states in figure 4.24. The nonradiative rate from the $5d$ to excited $4f$ level is called W_{df} and from the excited $4f$ to $5d$ is W_{fd} . The radiative rate from the $5d$ to the ground state is named P_d and from the excited $4f$ to the ground state is P_f . The lifetime of the excited $4f$ state is τ_f and $5d$ is τ_d . N_d and N_f are the initial populations just after the excitation pulse.

The nonradiative transition from the $5d$ to excited $4f$ states occurs with a probability W_{df} , while the reverse process has a probability as

$$W_{fd} = W_{df} \exp\left(-\frac{\Delta E}{kT}\right) \quad (4.4.3)$$

The rate equations for the populations N_d and N_f in the $5d$ and excited $4f$ levels are given as follows [51], respectively,

$$\frac{dN_d}{dt} = -(W_{df} + P_d)N_d + W_{fd}N_f \quad (4.4.4)$$

$$\frac{dN_f}{dt} = -(W_{fd} + P_f)N_f + W_{df}N_d \quad (4.4.5)$$

Equation (4.4.4) and (4.4.5) lead to a quadratic equation for lifetime t :

$$[W_{fd}P_d + P_f(W_{df} + P_f)\tau^2] - (W_{df} + W_{fd} + P_f + P_d)\tau + 1 = 0 \quad (4.4.6)$$

The two solutions of this equation give two constants of lifetime: the $5d$ (E_g) $\rightarrow 4f$ (${}^8S_{7/2}$) transition τ_d and the $4f$ (${}^6P_{7/2}$) $\rightarrow 4f$ (${}^8S_{7/2}$) transition τ_f . The decay curves of emission at 359 and 410 nm also can be fitted by using this model, and the results are shown in figure 4.25 (b) and 4.26 (b). The configurational coordinate diagram with energy levels and energy barriers of Eu^{2+} in LiBaF_3 is shown in figure 4.27, and the values fitted by the thermal quenching and three-level models are shown in table 4.2.

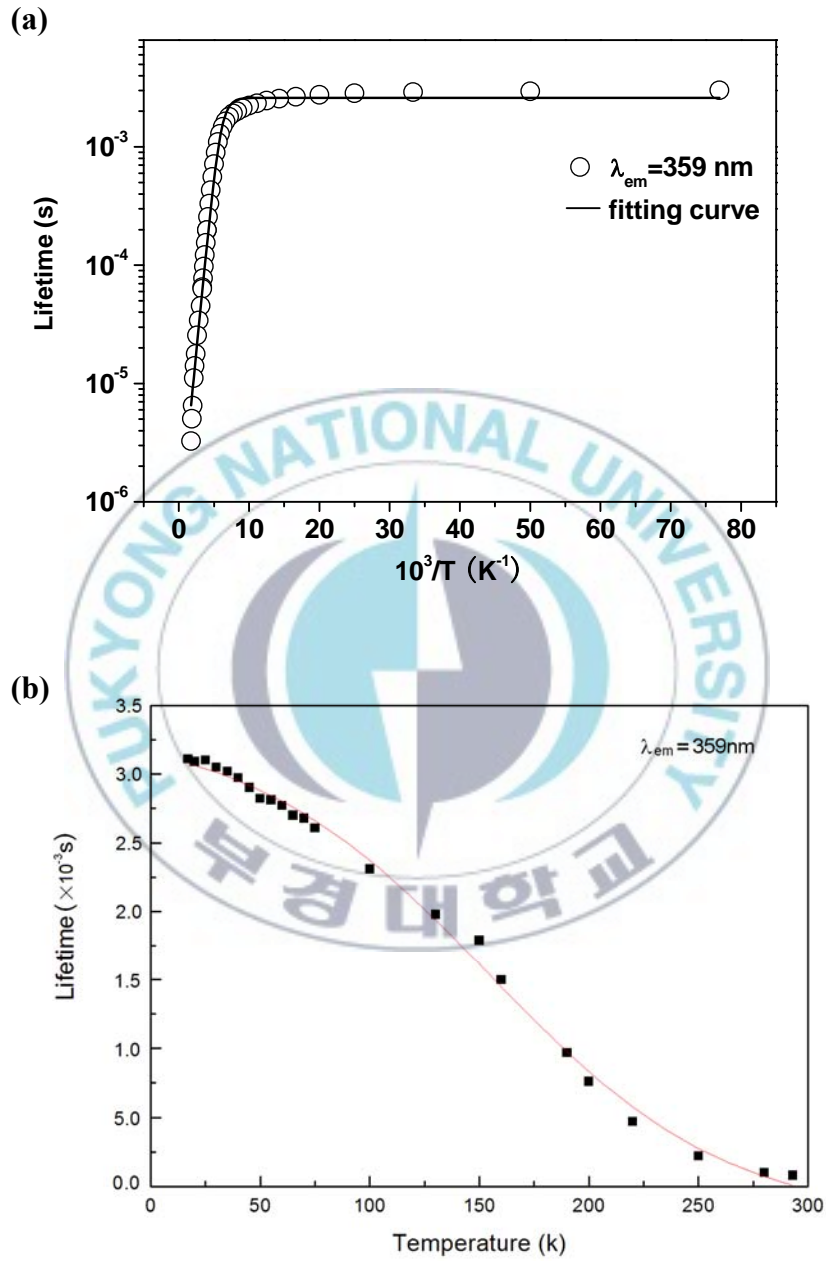


Figure 4.25 decay values of line emission (359 nm) (single points). The solid lines are the best fitting of the thermal activation (a) and three-level (b) models.

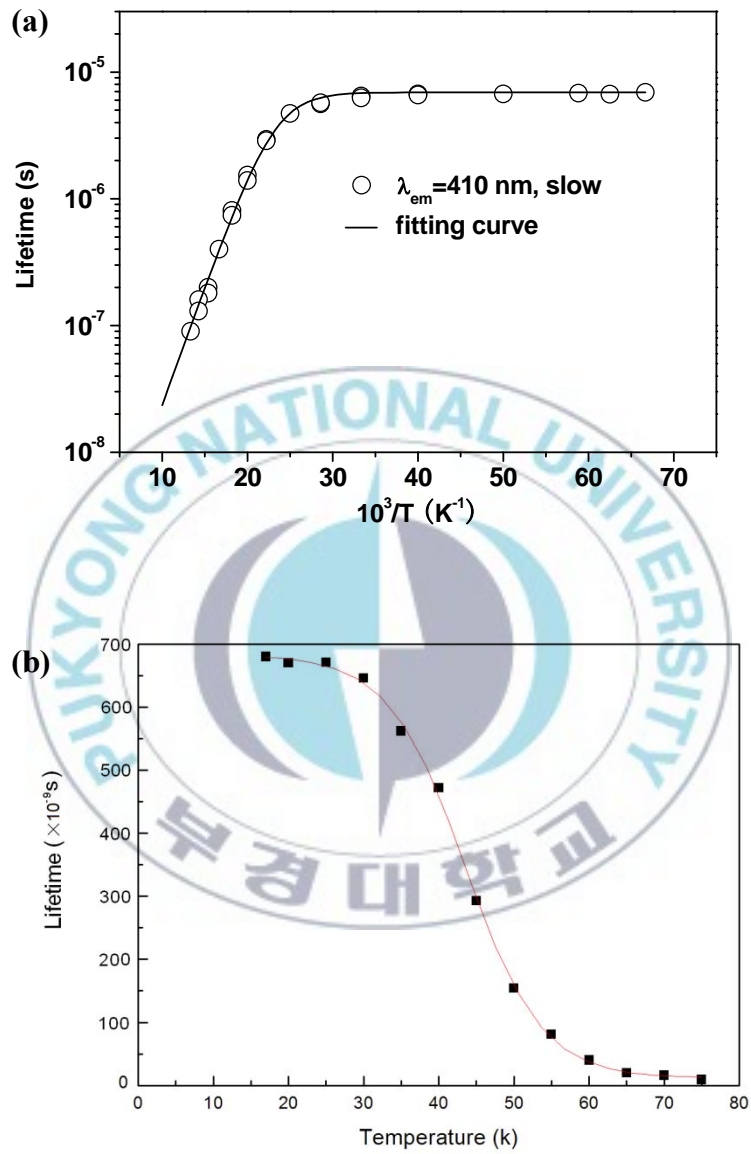


Figure 4.26 Decay values of fast component of broad band emission (410 nm) (single points). The solid lines are the best-fit of the thermal activation (a) and three-level (b) models.

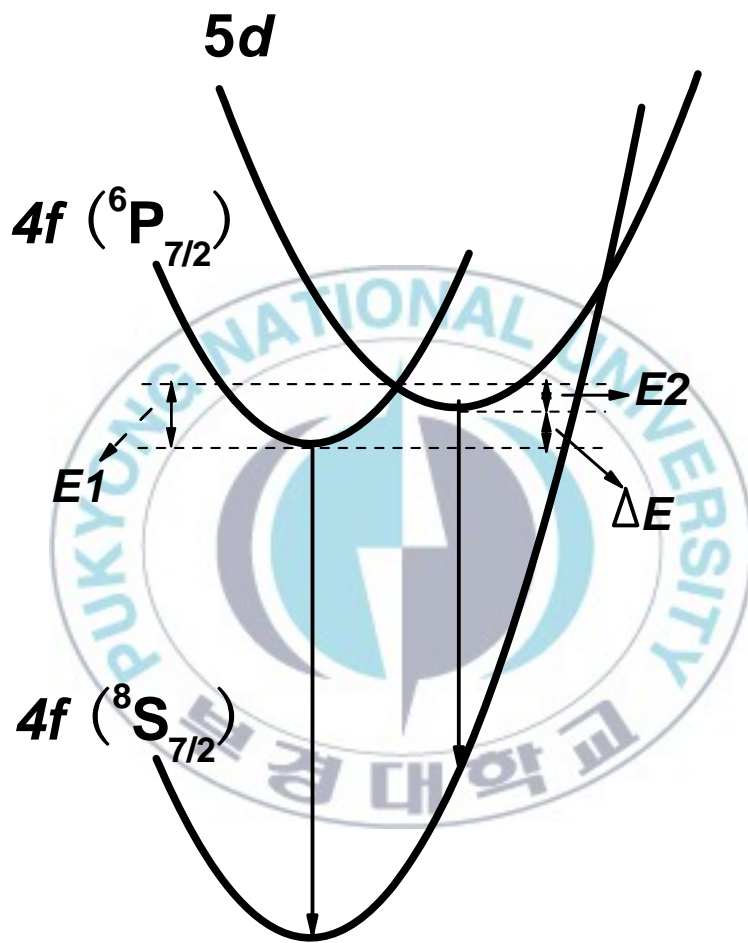
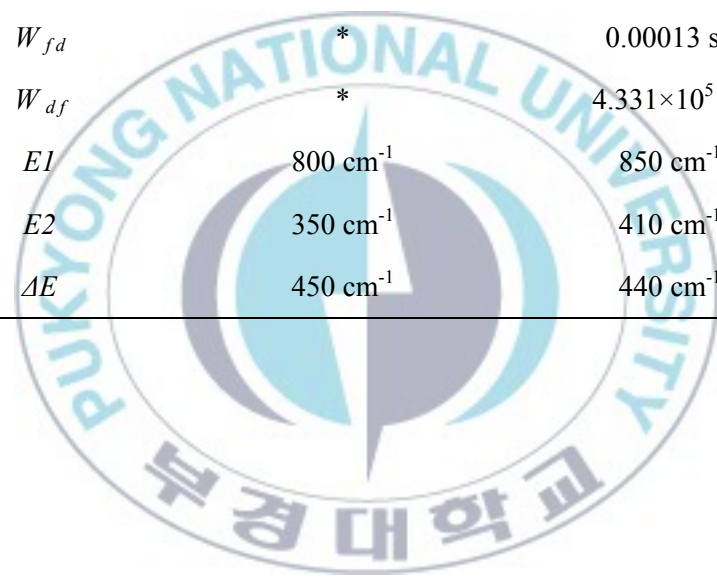


Figure 4.27 Configurational coordinate diagram of energy levels of Eu^{2+} in LiBaF_3 .

Table 4.2 Fitting values of Eu^{2+} in LiBaF_3 by the three-level and thermal activation models.

	Thermal activation model	Three-level model
P_f	333 s^{-1}	318 s^{-1}
P_d	$1.449 \times 10^6 \text{ s}^{-1}$	$1.465 \times 10^6 \text{ s}^{-1}$
W_{fd}	*	0.00013 s^{-1}
W_{df}	*	$4.331 \times 10^5 \text{ s}^{-1}$
$E1$	800 cm^{-1}	850 cm^{-1}
$E2$	350 cm^{-1}	410 cm^{-1}
ΔE	450 cm^{-1}	440 cm^{-1}



4.5 Quantum tunneling process in double wells of the 4f (${}^6P_{7/2}$) and 5d (E_g) states of Eu^{2+} in LiBaF_3

4.5.1 410-nm slow component by tunneling process

The population changes between the 4f (${}^6P_{7/2}$) and 5d (E_g) states depend strongly on temperature and energy barriers E1 and E2. The larger difference in the barrier energy between E1 (800 cm^{-1}) and E2 (350 cm^{-1}) and the significantly different transition rates between the 4f (${}^6P_{7/2}$) ($\sim 300\text{ s}^{-1}$) and 5d (E_g) ($\sim 2 \times 10^6\text{ s}^{-1}$) states lead us to analyze the population and depopulation processes in each state, especially in the 5d (E_g) state. Just after the 266 nm pulsed laser excitation the depopulation of the 5d (E_g) state occurs within very shorter time ($\sim 0.5\ \mu\text{s}$) and then the other population of the 5d (E_g) state occurs from the 4f (${}^6P_{7/2}$) state via thermal activation and quantum tunneling processes. The population process of the 5d (E_g) state from the 4f (${}^6P_{7/2}$) state takes place in the millisecond region because the transition from the 4f (${}^6P_{7/2}$) state to the ground 4f (${}^6P_{7/2}$) occurs in the millisecond region. In this Chapter the anomalies such as the decay time values as function of temperature, the nonexponential decay curves, and different spectral feature of the 410-nm slow component by (late relaxation process of the 5d (E_g) state) are discussed in relation with quantum tunneling process.

On the discussion of the spectra and decay curves of line emission, and band emission, we have often mentioned that the energy transfer and energy back transfer processes between the excited $4f$ and $5d$ states. Now, the question is “what the mechanism of transfer and back transfer processes at low temperature (< 100 K)”? Considering the maximum Stokes and anti-Stokes shift of the vibrations, the maximum phonon energy of $\text{LiBaF}_3:\text{Eu}^{2+}$ single crystal is $h\nu_5 = 450 \text{ cm}^{-1}$, therefore, the energy barrier E_1 (800 cm^{-1}) is very hard to be activated by thermal energy at low temperature (< 60 K). However, we observe 410-nm slow component with unusual decay values as a function of temperature. So, the point is to understand how the energy transfers happen between the excited $4f$ and $5d$ states even at low temperature.

Figure 4.28 (a) shows the integrated intensities of band emissions at 410 nm of slow decay component. The intensity firstly decreases from 20 to 60 K and then increases from around 70 K. Suppose that the energy transfer from the excited $4f$ to $5d$ states is only due to the thermal activation process, the integrated intensity of 410-nm slow component should increase with the temperature because the thermal transfer is very fast. Therefore, the decrease in intensity up to 60 K means there is an unusual way to transfer energy from the excited $4f$ state to $5d$ state. Consider the average decay values of band emission with slow component, the quantum tunneling process from the excited $4f$ state to $5d$ state can be confirmed in the temperature region of 15-60 K [52-54] and shown in figure 4.28 (b). The straight arrow 1 is the tunneling process from the excited $4f$ to $5d$ levels and the crooked arrow 2 is the thermal activation process. In 15-65 K, the thermal activation of $4f$

→ $5d$ transition cannot occur, the $4f(^6P_{7/2}) \rightarrow 5d(E_g)$ energy back transfer is due to the tunneling process. Therefore, the decay curve of fast component shows a tail, which means the time delay of the $4f \rightarrow 5d$ transition.

Figure 4.29 (a) and (b) shows comparison of decay curves of band emissions at 410 nm with fast and slow lifetime components and a transfer model between the excited $4f$ and $5d$ states in temperature region of 15-180 K. The fast component shows usual temperature dependence due to the thermal activation from the $5d$ to $4f$ states (arrow 1). The decay of the slow component shows the similar trend with the fast components in the region of 15-60 K because of the very fast quantum tunneling process (arrow 2). However, when the temperature increases, the tunneling process is insensitive but the thermal activation process (3) from the excited $4f$ level becomes dominant. Therefore, the dip is observed in the decay values of slow component as a function of temperature and the values (\sim ms) close to the line emission at 359 nm.

Figure 4.30 shows the calculated decay values of emission at 359 nm (circle) and 410 nm (triangle) with slow decay component of $\text{LiBaF}_3:\text{Eu}^{2+}$ single crystal between 15 and 300 K under 266 nm excitation. It is noted that the decay values of these two curves (359 nm and 410-nm slow) have similar trend; and at higher temperature (> 150 K), the decay values are the same. The result at high temperature indicates thermal equilibrium is reached at temperature around 150 K.

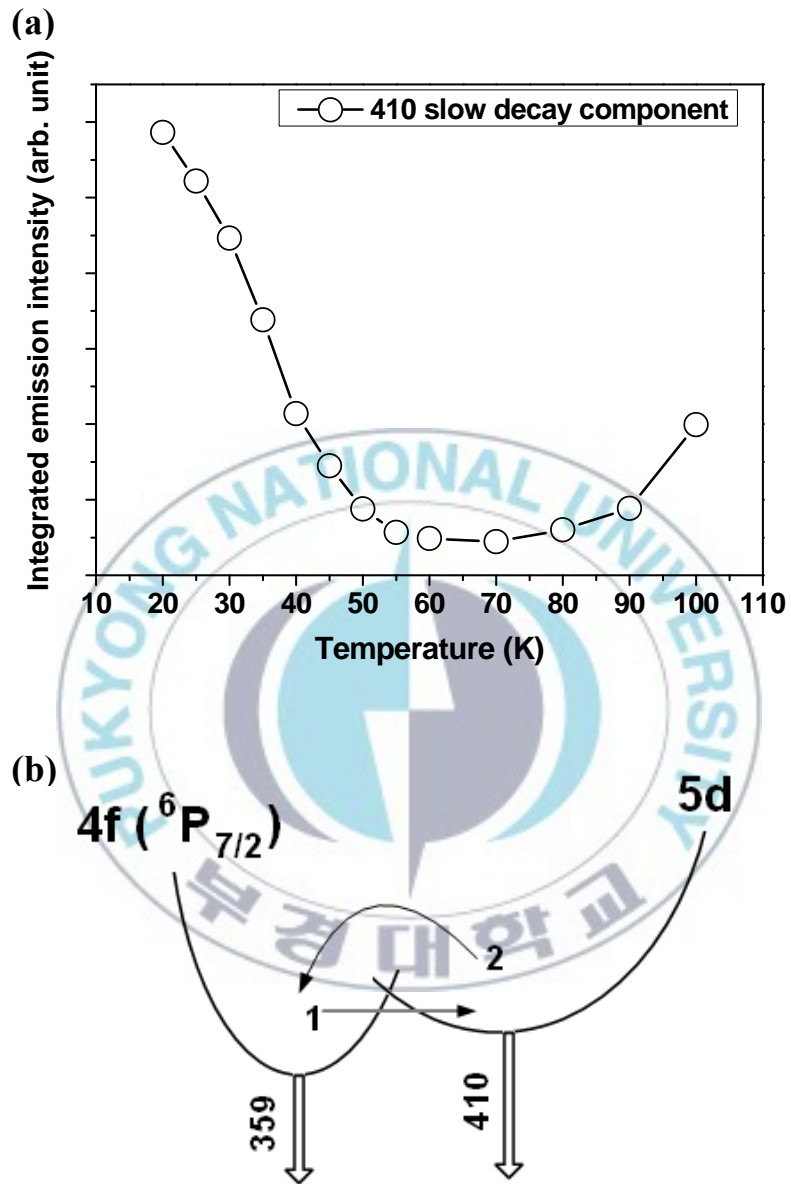


Figure 4.28 (a) Integrated intensities of band emissions at 410 nm with slow decay component. (b) The thermal activation (2) and tunneling (1) transfers between the excited $4f$ and $5d$ states.

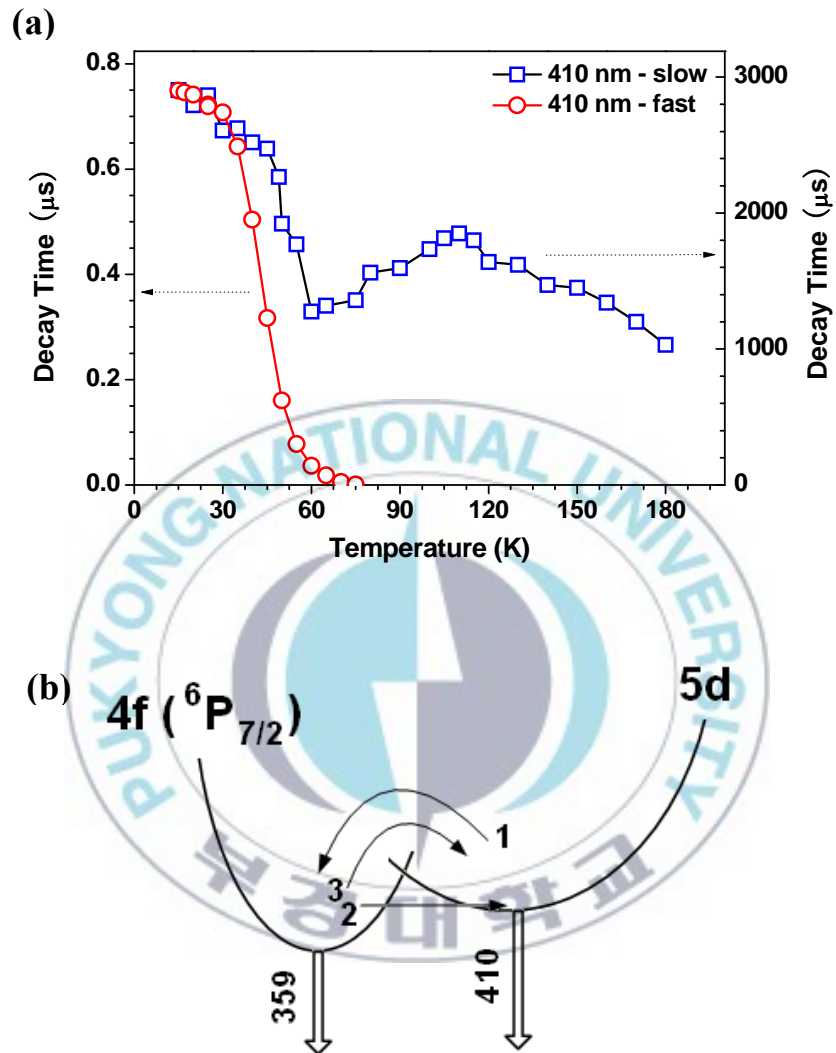


Figure 4.29 (a) Decay values of band emissions at 410 nm with fast and slow decay components in temperature region of 15-180 K. (b) The thermal activation (arrows 1 and 3) and tunneling (2) transfers between the excited $4f$ and $5d$ states.

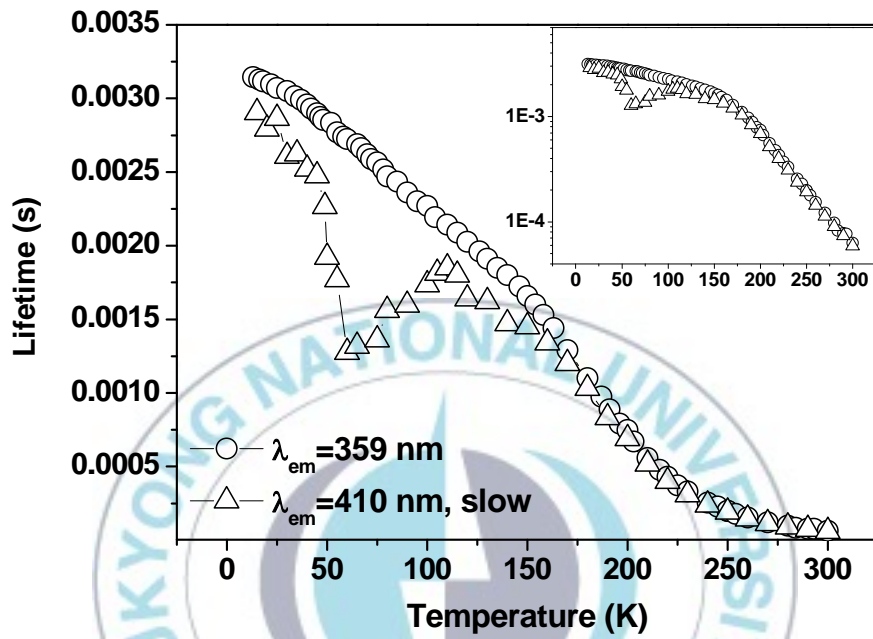


Figure 4.30 The calculated decay values of emission at 359 nm (circle) and 410 nm (triangle) with slow decay component of LiBaF₃:Eu²⁺ single crystal between 15 and 300 K under 266 nm excitation. The inset is logarithmic scale of decay values.

Figure 4.31 (a) shows the normalized initial and integrated intensities of emission at 410 nm with fast decay component in the temperature region of 15-100 K. The initial intensity means the populated excited ions in the $5d$ state at initial time after laser pulse. The integrated intensity shows the usual effective energy transfer from the $5d$ state to ground state. With increasing temperature, the integrated intensity decreases fast, while the initial intensity is nearly in the same value. The results show that the population of the $4f(^6P_{7/2})$ state moves very fast to the $5d(E_g)$ state via tunneling process. It is assumed that, as increasing temperature from 20 K to 60 K, the tunneling probability from $4f(^6P_{7/2})$ to $5d(E_g)$ is nearly the same, while energy transfer from $5d$ to $4f$ state increases due to the thermal activation process.

Figure 4.31 (b) shows an unusual increase of the initial intensity of fast component at 410 nm in 15-40 K. The result shows that the populated excited ions in the $5d$ state at initial time after laser pulse increases slightly as a function of temperature. The increase of initial intensity is very small (10 %) in 15-40 K. The increase in initial intensity of 410-nm fast component means that the feeding of the $5d(E_g)$ state is larger than the quenching due to the thermal activation from the $5d(E_g)$ to $4f(^6P_{7/2})$ state.

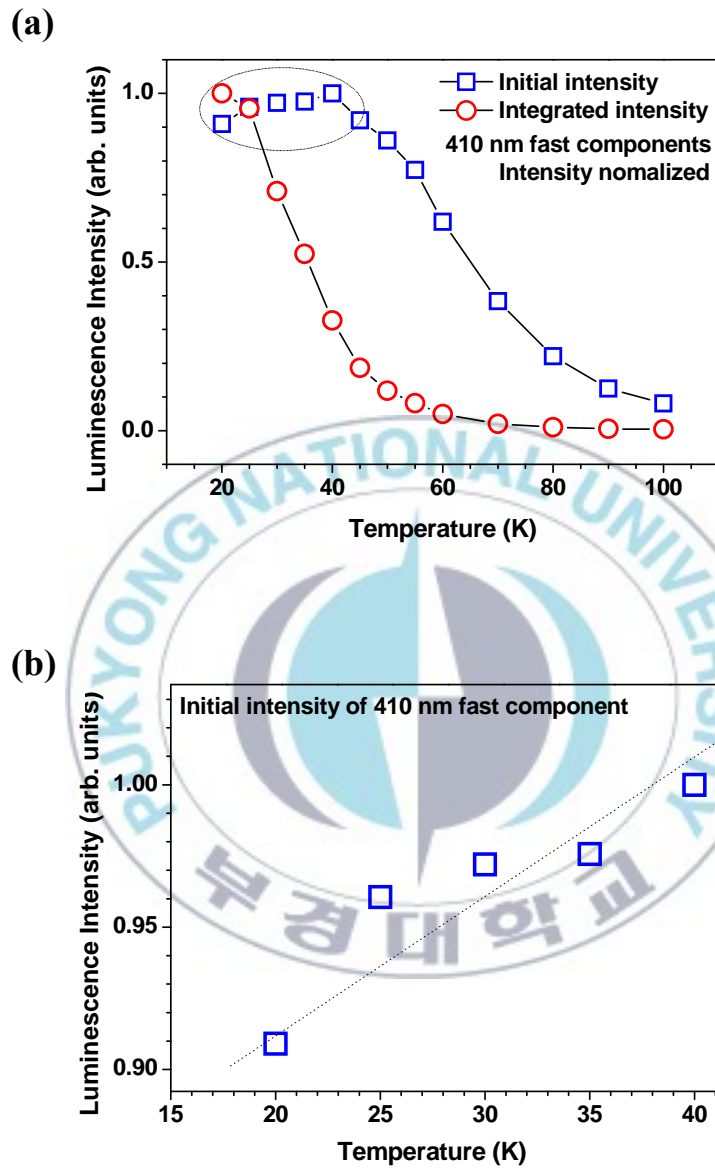


Figure 4.31 (a) the normalized initial and integrated intensities of fast component at 410 nm in 15-100 K. (b) the normalized initial intensity of fast component at 410 nm in 15-40 K.

Figure 4.32 shows an integrated intensity curve of emission band at 410 nm with slow decay component. This decay is explained a rise time of line emission before (Chapter 4.4.1, p. 79). Thus, its behavior should be similar to decay of line emission, i.e., the similar temperature-dependent quenching behavior. However, the integrated intensity shows irregular in this figure. At low temperature (< 100 K), the intensity decreases fast (figure b), which is explained by the thermal quenching process. However, at higher temperature (> 100 K), the intensity of emission with slow decay shows an anomalous increase with temperature and saturates nearly at 300 K. This phenomenon gives a strong evidence of the energy back transfer from the excited $4f$ to $5d$ state.

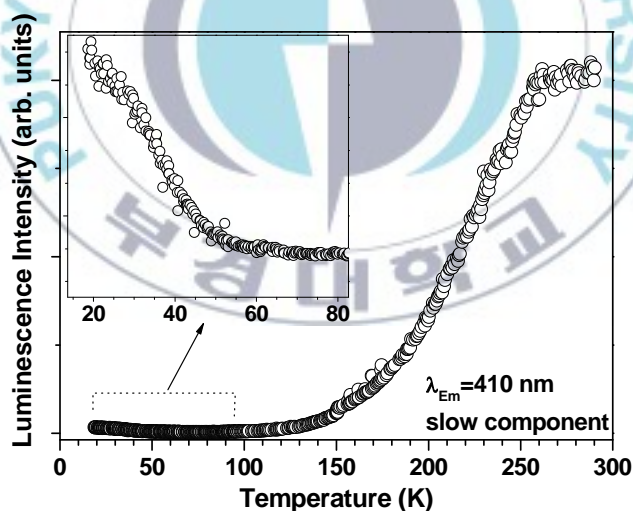


Figure 4.32 The integrated intensity curve of band emission at 410 nm with slow decay component in the temperature region of 15-300 K. The inset is the intensity curve in 15-80 K.

4.5.2 Anomalous spectral feature and nonexponential decay curves of 410-nm slow component

Figure 4.33 shows the decay curves of 359 nm emission and 410 nm emission with slow component at 15 K. The decay of 359 nm emission ($4f(^6P_{7/2})$) is single exponential whereas the 410 nm emission with slow component is nonexponential. We should understand the reason why the 410-nm slow component is slightly nonexponential although the 359 nm shows single exponential.

Normally, the decay of band emission from $5d(E_g)$ to ground state are very short ($\sim \mu\text{s}$), but the slow component is in order of millisecond because the feeding is due to the energy transfer from the excited $4f$ state. Except for the initial part of the decay curve of 410-nm slow component, the decay time values are similar with that of 359 nm. We attribute this result to the mixing of the $4f(^6P_{7/2})$ and $5d(E_g)$ states [52-54].

Considering a usual energy transfer from the excited $4f$ to $5d$ states by thermal activation process, this process is so fast ($\sim \text{fs}$) to observe in decay curve with the lifetime of a few milliseconds. Therefore, the decay curve of slow component should be single exponential. As discussed in Chapter 2.7, when energy transfer from $4f(^6P_{7/2})$ to $5d(E_g)$ state takes place via the quantum tunneling process, it forms a tunneling state with new wavefunction $\psi'_d(r, R)$ by mixing of the $4f(^6P_{7/2})$ and $5d(E_g)$ states. This is given by

$$\psi'_d(r, R) = \beta\psi_f(r, R) - \alpha\psi_d(r, R).$$

The lifetime of tunneling 5d (E_g) state can be also modified. We suggest that the nonexponential decay curve of 410-nm slow component is ascribed to the tunneling process.

The intensity of two emissions by monitoring at different time gates was normalized. By comparison with the emission bands with the fast and slow decay components, the wavelength position of these two emissions is nearly the same. However, the full width at half maximum (FWHM) of slow decay component is narrower than the fast one at the same temperature, which means that this type transition is different with the normal $5d \rightarrow 4f$ transition (i.e. emission with fast decay). An anomalous band emission with slow decay component at low temperature is also suggested from the mixing of the excited $4f$ and $5d$ states. The mixed 5d (E_g) state (called 5d (E_g)_{mix}) for 410-nm slow component modifies the normal 5d (E_g) state and so the emission due to the $5d (E_g)_{\text{mix}} \rightarrow 4f (^8S_{7/2})$ transition resulting in slightly different spectral feature as in figure 4.34. The time-resolved emission spectra monitoring at the fast and slow decay components by using the time gate (Δt) = 0-3.6 μs and 0.4-1.8 ms are shown in figure 4.34. It is necessary further study for the band shape of 410-nm slow component which is narrow than the 410-nm fast component.

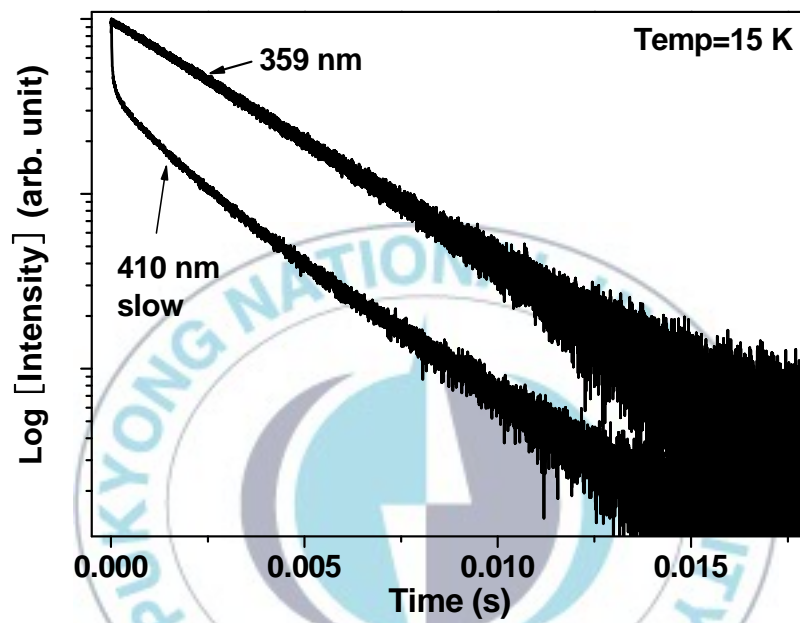


Figure 4.33 Decay curves of 359 nm emission and 410 nm emission with slow component at 15 K.

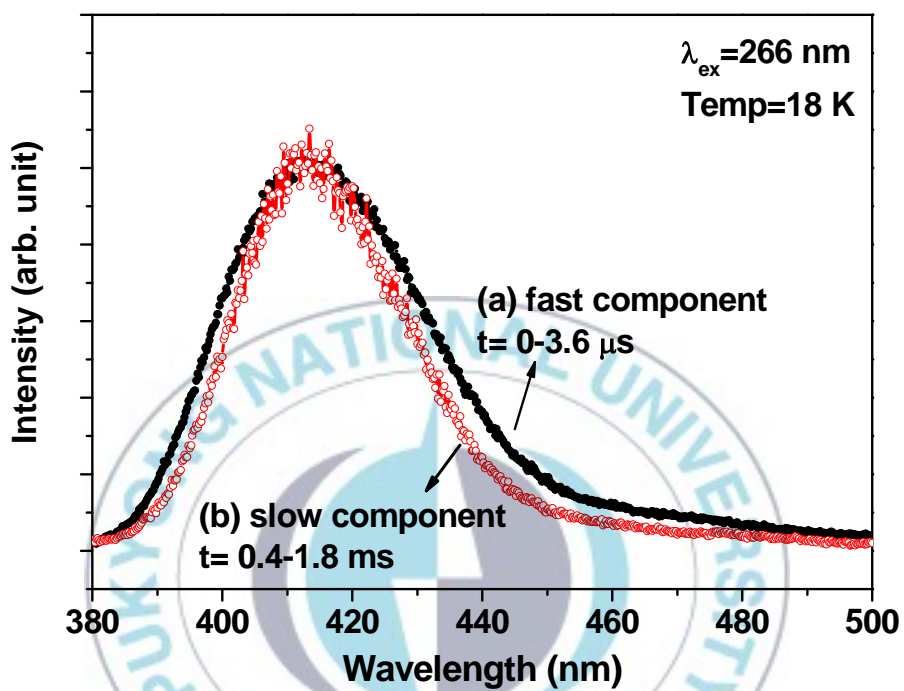


Figure 4.34 Time-resolved emission spectra of the $\text{LiBaF}_3:\text{Eu}^{2+}$ single crystal at 18 K excited by 266 nm laser. (a) and (b) are the band emissions monitoring at the fast and slow decay components by using the time gate (Δt) = 0-3.6 μs and 0.4-1.8 ms, respectively.

5. Conclusions

The Eu-doped LiBaF₃ single crystals were prepared by the Czochralski method. The LiBaF₃ melted incongruently and the crystals were grown from a non-stoichiometric melt to avoid other phase precipitations. The different mole ratios of the LiF and BaF₂ powder greatly influence the purity of the LiBaF₃ compounds. The best mole ratio is 3:2. Also, the effect of two times calcinations can enhance the purity of the compounds. It is found that the initial temperature cooling rate should be lower than 1 °C/h and a good initial part of the crystal is very important which requires the neck of the crystal should be long and small. Since the crucible is big without a platinum attenuator and the LiBaF₃ single crystal is grown from the non-stoichiometric melt, the pulling speed should be lower than 1 mm/h. Otherwise, there would be many cracks inside the crystal. Different rotation speeds yield the different temperature fields which also influence the optical properties of the LiBaF₃ single crystal.

The sharp line and broad band emission spectra from the excited $4f \rightarrow 4f$ and the $5d \rightarrow 4f$ transitions have been clearly observed at different temperatures, respectively. The energy level of the excited $4f$ state is confirmed lower than the $5d$ state. The intensity of emission spectra increases with the concentration of Eu²⁺ ions below 2 mol%. The zero-phonon line of the $4f \rightarrow 4f$ transition is observed with some Stokes and anti-Stokes vibrations, and their intensity shows strong temperature-dependence.

The time-resolved emission spectra and temperature-dependent decays of Eu²⁺

in LiBaF₃ show an anomalous energy transfer process. The initial rise times of 359 nm emission and nonexponential decay curves of 410-nm slow are clearly observed and compared systematically. The rise time of 359 nm emission is considered from the *5d* state and that of the slow component of 410 nm is from the excited *4f* state. A best-fit is used to temperature-dependent decay values and the three-level model is applied for Eu²⁺ in LiBaF₃ host to describe the dynamic transfer mechanism. The results give many evidences of the existence of quantum tunneling transition from the excited *4f* to *5d* states. It is confirmed that these energy transfer and energy back-transfer processes between the excited *4f* and *5d* levels are originated from competition between the quantum tunneling and thermal activation processes at low temperature.

Considering the time-resolved emission spectra, temperature-dependent decays, and integrated intensities of Eu²⁺ in LiBaF₃, the luminescent dynamics is concluded as follows:

(1) $T < 75$ K, quantum tunneling process is effective for *5d* → *4f* transition as evidenced from the nonexponential decay curves of slow component and the increase of initial intensity of band emission with fast decay. The tunneling process for *5d* → *4f* transition is dominative although it is insensitive with temperature, and the energy transfer from *5d* to *4f* states is very weak.

(2) Between 75 and 150 K, tunneling process competes with the thermal activation process. In this temperature region, the excited *4f* state obtains the energy from *5d* state easily through the thermal activation process and also losses

the small energy by the tunneling process. The energy back transfer from the excited $4f$ to $5d$ state also exists by thermal activation process.

(3) $T > 150$ K, It is reached thermal equilibrium between the $4f(^6P_{7/2})$ and $5d(E_g)$ states. The decays of line emission and band emission (no fast component) are the same. At higher temperature, the slow decay curves of band emissions become single exponential.



References

- [1] J. Rubio O., *J. Phys. Chem. Solids* **52**, 101 (1991).
- [2] S. Shionoya and W.M. Yen, “Phosphor Handbook”, CRC Press (1998).
- [3] J. G. Solé, L. E. Bausá, and D. Jaque, “An Introduction to the Optical Spectroscopy of Inorganic Solids”, Wiley (2005).
- [4] G. K. Liu and B. Jacquier, “Spectroscopic Properties of Rare Earths in Optical Materials”, Springer (1994).
- [5] G. Blasse and B. C. Gramaier, “Luminescent Materials”, Springer (1994).
- [6] T. Tsuboi and A. Scacco, *J. Phys.: Condens. Matter* **10**, 7259 (1998).
- [7] P. Dorenbos, *J. Lumin.* **104**, 239 (2003).
- [8] B. Tanguy, P. Merle, M. Pezat, and C. Fouassier, *Mater. Res. Bull.* **9**, 831 (1974).
- [9] A. Meijerink, *J. Lumin.* **55**, 125 (1993).
- [10] S. Mahlik, M. Grinberg, L. Shi, and H. J. Seo, *J. Phys.: Condens. Matter* **21**, 235603 (2009).
- [11] A.V. Gektin, *J. Lumin.* **87-89**, 1283 (2000).
- [12] C. T. Xia and C. S. Shi, *Mater. Res. Bull.* **32**, 107 (1997).
- [13] A. Meijerink and G. J. Dirksen, *J. Lumin.* **63**, 189 (1995).
- [14] P. Kulis, I. Tale, I. Gromuls, M. Nikl, N. Ichinose, and K. Shimamura, *Radiat. Meas.* **38**, 723 (2004).
- [15] R. Leckebusch, A. Neuhaus, and K. Recker, *J. Cryst. Growth* **16**, 10 (1972).
- [16] S. L. Baldochi and J. Y. Gesland, *Mater. Res. Bull.* **27**, 891 (1992).
- [17] S. L. Baldochi, V. L. Mazzocchi, C. B. R. Parente, and S. P. Morato, *Mater.*

- Res. Bull. **29**, 1321 (1994).
- [18] A. Bensalah, K. Shimamura, T. Fujita, H. Sato, M. Nikl, and T. Fukuda, J. Alloys Compd. **348**, 258 (2003).
- [19] H. L. Li, R. J. Xie, N. Hirosaki, and Y. Yajima, J. Electrochem. Soc. **155**, J378 (2008).
- [20] C. H. Huang, Y. C. Chen, T. W. Kuo, and T. M. Chen, J. Lumin. **131**, 1346–1349 (2011).
- [21] S. Y. Zhang, Y. Nakai, T. Tsuboi, Y. L. Huang, and H. J. Seo, Chem. Mater. **23**, 1216 (2011).
- [22] K. S. Sohn, S. J. Lee, R. J. Xie, and N. Hirosaki, Appl. Phys. Lett. **95**, 121903 (2009).
- [23] T. W. Kuo, W. R. Liu, and T. M. Chen, Opt. Express **18**, 8187 (2010).
- [24] J. L. Sommerdijk, J.M.P.J. Verstegen, and A. Bril, J. Lumin. **10**, 411 (1975).
- [25] C. H. Li, X. G. Lu, W. Z. Ding, L. M. Feng, Y. H. Gao, and Z. M. Guo, Acta Crystallogr. B **64**, 702 (2008).
- [26] W.L.W. Ludekens and A.J.E. Welch, Acta Crystallogr. **5**, 841 (1952).
- [27] P. Hagenmuller, “Inorganic Solid Fluorides”, Academic Press (1985).
- [28] Z. L. Wang and Z. C. Kang, “Functional and Smart Materials”, Plenum Press (1998).
- [29] Yamaga M, Honda M, Kawamata N, Fujita T, Shimamura K, and Fukuda T, J. Phys.: Condens. Matter **13**, 3461 (2001).
- [30] N. J. M. Le Masson, A. J. J. Bos, C. W. E. Van Eijk, C. Furetta, and J. P. Chaminade, Radiat. Prot. Dosim. **100**, 229 (2002).

- [31] S. Ono, R. E. Ouenzerfi, A. Quema, H. Murakami, N. Sarukura, T. Nishimatsu, N. Terakubo, H. Mizuseki, Y. Kawazoe, A. Yoshikawa, and T. Fukuda, *Jpn. J. Appl. Phys.* **44**, 7285 (2005).
- [32] R. Alcalá, D. K. Sardar, and W. A. Sibley, *J. Lumin.* **27**, 273 (1982).
- [33] P. J. Edwardson, L. L. Boyer, R. L. Newman, D. H. Fox, J. R. Hardy, J. W. Flocken, R. A. Guenther, and W. Mei, *Phys. Rev. B* **39**, 9738 (1989).
- [34] J. L. Sommerdijk and A. Bril, *J. Lumin.* **11**, 363 (1976).
- [35] T. B. Bekker, A. E. Kokh, N. G. Kononova, P. P. Fedorov, and S. V. Kuznetsov, *Cryst. Growth and Des.* **9**, 4060 (2009).
- [36] T. Nishimatsu, N. Terakubo, H. Mizuseki, Y. Kawazoe, D. A. Pawlak, K. Shimamura, and T. Fukuda, *Jpn. J. Appl. Phys.* **41**, 365 (2002).
- [37] M. A. Couto dos Santos, M. E. G. Valerio, R. A. Jackson, and J. F. de Lima, *Chem. Phys. Lett.* **369**, 90 (2003).
- [38] J. L. Sommerdijk, A. Bril, and F.M.J.H. Hoex-Strik, *J. Lumin.* **15**, 115 (1977).
- [39] M. C. Shinn and W. A. Sibley, *Phys. Rev. B* **29**, 3834 (1984).
- [40] M. Marsman, J. Andriessen, and C. W. E van Eijk, *Phys. Rev. B* **61**, 16477 (2000).
- [41] M. Henke, J. Perþon, and S. Kück, *J. Lumin.* **87-89**, 1049 (2000).
- [42] R. D. Shannon, *Acta Crystallogr. A* **32**, 751 (1976).
- [43] A. Boumriche, J. Y. Gesland, A. Bulou, M. Rousseau, J. L. Gourquet, and B. Hennion, *Solid State Commun.* **91**, 125 (1994).
- [44] Y. Tan and C. Shi, *J. Phys. Chem. Solids* **60**, 1805 (1999).
- [45] S. H. M. Poort, A. Meyerink, and G. Blasse, *J. Phys. Chem. Solids* **58**, 1451

- (1997).
- [46] R. Alcalá, D. K. Sardar, and W. A. Sibley, *J. Lumin.* **27**, 273 (1982).
- [47] Di Barolo, “Optical Interactions in Solids”, John Wiley & Sons (1968).
- [48] B. Moine and C. Pedrini, *Phys. Rev. B* **30**, 993 (1984).
- [49] V. Mürk, M. Nikl, E. Mihoková, and K. Nitsch, *J. Phys.: Condens. Matter* **9**, 249 (1997).
- [50] S. F. Collins, G. W. Baxter, S. A. Wade, T. Sun, K. T. V. Grattan, Z. Y. Zhang, and A.W. Palmer, *J. Appl. Phys.* **84**, 4649 (1998).
- [51] D. L. S. Dang, R. Romestain, and D. Simkin, *Phys. Rev. B* **18**, 2989 (1978).
- [52] M. Yamaga, B. Henderson, K. P. O’Donnell, and G. Yue, *Appl. Phys. B* **51**, 132 (1990).
- [53] M. Yamaga, B. Henderson, and K. P. O’Donnell, *J. Phys.: Condens. Matter* **1**, 9157 (1989).
- [54] M. Yamaga, B. Henderson, K. P. O’Donnell, C. Trager Cowan, and A. Marshall, *Appl. Phys. B* **50**, 425 (1990).
- [55] P. Dorenbos, *J. Lumin.* **104**, 239 (2003).
- [56] Y.P. Varshini, *Physica* **34**, 149 (1967).
- [57] J. S. Kim, Y. H. Park, S. M. Kim, J. C. Choi, and H. L. Park, *Solid State Commun.* **133**, 445 (2005).
- [58] L. Shi, Y. L. Huang, and H. J. Seo, *J. Phys. Chem. A* **114**, 6927 (2010).
- [59] Y. Huang and H. J. Seo, *J. Phys. Chem. A* **113**, 5317 (2009).
- [60] V. Bachmann, C. Ronda, O. Oeckler, W. Schnick, and A. Meijerink, *Chem. Mater.* **21**, 316 (2009).

Publication List

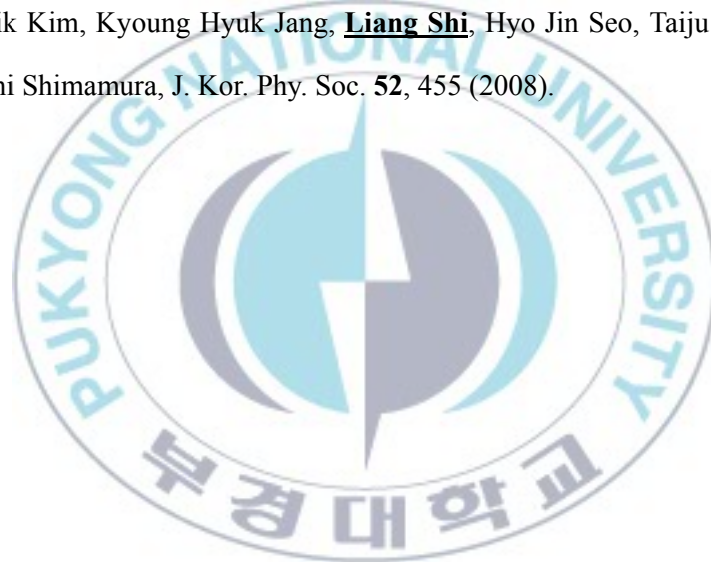
1. **Liang Shi** and Hyo Jin Seo, *Opt. Express* **19**, 7147 (2011).
2. **Liang Shi** and Hyo Jin Seo, *J. Lumin.* **131**, 523 (2011).
3. P. Babu, K. H. Jang, C. S. Rao, **L. Shi**, C. K. Jayasankar, V. Lavin, and H. J. Seo, *Opt. Express* **19**, 1836 (2011).
4. R. Praveena, **Liang Shi**, Kyoung Hyuk Jang, V. Venkatramu, C. K. Jayasankar, and Hyo Jin Seo, *J. Alloy. Compd.* **509**, 859 (2011).
5. **Liang Shi**, Yanlin Huang, and Hyo Jin Seo, *J. Phys. Chem. A* **114**, 6927 (2010).
6. Xiaoli Shi, Yanlin Huang, Jie Yan, **Liang Shi**, Xuebin Qiao, and Hyo Jin Seo, *J. Rare Earth.* **28**, 693 (2010).
7. Suyin Zhang, Yanlin Huang, **Liang Shi**, and Hyo Jin Seo, *J. Phys.: Condens. Matter* **22**, 35402 (2010).
8. DongLei Wei, Yanlin Huang Jin Soo Kim, **Liang Shi**, and Hyo Jin Seo, *J. Electron. Mater.* **39**, 441 (2010).
9. Yonggang Cao, Yanlin Huang, **Liang Shi**, Hyo Jin Seo, and Ye Tao, *Inorg. Mater.* **46**, 983 (2010).
10. Chuanxiang Qin, Yanlin Huang, Wanxue Zhao, **Liang Shi**, and Hyo Jin Seo, *Mater. Chem. Phys.* **121**, 286 (2010).
11. Jiayu Wang, Yadong Li, Yanlin Huang, **Liang Shi**, and Hyo Jin Seo, *Mater. Chem. Phys.* **120**, 598 (2010).

12. Nuan Xie, Yanlin Huang, Xuebin Qiao, **Liang Shi**, and Hyo Jin Seo, *Mater. Lett.* **64**, 1000 (2010).
13. P. Babu, Kyoung Hyuk Jang, Eun Sik Kim, **Liang Shi**, R. Vijaya, V. Lavín, C.K. Jayasankar, and Hyo Jin Seo, *J. Non-Cryst. Solids* **356**, 236 (2010).
14. Haiyan Ding, Yanlin Huang, **Liang Shi**, and Hyo Jin Seo, *J. Electrochem. Soc.* **157**, J54 (2010).
15. Chongfeng Guo, Lin Luan, **Liang Shi**, and Hyo Jin Seo, *Electrochem. Solid St.* **13**, J28 (2010).
16. Suyin Zhang, Yanlin Huang, Weifang Kai, **Liang Shi**, and Hyo Jin Seo, *Electrochem. Solid St.* **13**, J11 (2010).
17. Donglei Wei, Yanlin Huang, **Liang Shi**, Xuebin Qiao, and Hyo Jin Seo, *J. Rare Earth.* **27**, 905 (2009).
18. Suyin Zhang, Yanlin Huang, **Liang Shi**, Xuebin Qiao, and Hyo Jin Seo, *Phys. B* **404**, 4136 (2009).
19. K. H. Jang, W. K. Sung, E. S. Kim, **L. Shi**, J. H. Jeong and, H. J. Seo, *J. Lumin.* **129**, 1853 (2009).
20. Donglei Wei, Yanlin Huang, **Liang Shi**, Xuebin Qiao, and Hyo Jin Seo, *J. Electrochem. Soc.* **156**, H885 (2009).
21. Kyoung Hyuk Jang, Eun Sik Kim, **Liang Shi**, N. M. Khaidukov, and Hyo Jin Seo, *Opt. Mater.* **31**, 1819 (2009).
22. Chuanxiang Qin, Yanlin Huang, **Liang Shi**, Guoqiang Chen, Xuebin Qiao, and Hyo Jin Seo, *J. Phys. D: Appl. Phys.* **42**, 185105 (2009).
23. Jiu-hui Gan, Yanlin Huang, **Liang Shi**, Xuebin Qiao, and Hyo Jin Seo, *Mater.*

- Lett. **63**, 2160 (2009).
24. Haiyan Ding, Yanlin Huang, Donglei Wei, **Liang Shi**, Xuebin Qiao, and Hyo Jin Seo, J. Electrochem. Soc. **156**, J312 (2009).
 25. Kyoung Hyuk Jang, Eun Sik Kim, **Liang Shi**, Jung Hyun Jeong, and Hyo Jin Seo, Chem. Phys. Lett. **479**, 65 (2009).
 26. XiaoWu, Yanlin Huang, **Liang Shi**, and Hyo Jin Seo, Mater. Chem. Phys. **116**, 449 (2009).
 27. Yanlin Huang, **Liang Shi**, Xuebin Qiao, and Hyo Jin Seo, J. Electrochem. Soc. **156**, J230 (2009).
 28. Chuanxiang Qin, Yanlin Huang, Guoqiang Chen, **Liang Shi**, Xuebin Qiao, Jihui Gan, and Hyo Jin Seo, Mater. Lett. **63**, 1162 (2009).
 29. S. Mahlik, M. Grinberg, **Liang Shi**, and Hyo Jin Seo, J. Phys.: Condens. Matter **21**, 235603 (2009).
 30. Yanlin Huang, Wanxue Zhao, **Liang Shi** and Hyo Jin Seo, J. Alloy. Compd. **477**, 936 (2009).
 31. Yanlin Huang, Chuanfang Jiang, Yonggang Cao, **Liang Shi**, and Hyo Jin Seo, Mater. Res. Bull. **44**, 793 (2009).
 32. P. Babu, Kyoung Hyuk Jang, Eun Sik Kim, **Liang Shi**, and Hyo Jin Seo, J. Kor. Phy. Soc. **54**, 1488 (2009).
 33. P. Babu, Kyoung Hyuk Jang, Eun Sik Kim, **Liang Shi**, Hyo Jin Seo, F. Rivera-López, U. R. Rodríguez-Mendoza, V. Lavín, R. Vijaya, C. K. Jayasankar, and L. Rama Moorthy, J. Appl. Phys. **105**, 013516 (2009).
 34. Yanlin Huang, **Liang Shi**, Eun Sik Kim, and Hyo Jin Seo, J. Appl. Phys. **105**,

013512 (2009).

35. Eun Sik Kim, Kyoung Hyuk Jang, Liang Shi, and Hyo Jin Seo, J. Kor. Phy. Soc. **53**, 782 (2008).
36. Yanlin Huang, Yonggang Cao, Chuanfang Jiang, Liang Shi, Ye Tao, and Hyo Jin Seo, Jpn. J. Appl. Phys. **47**, 6364 (2008).
37. Yanlin Huang, Kyoung Hyuk Jang, Eun Sik Kim, Liang Shi, and Hyo Jin Seo, J. Kor. Phy. Soc. **52**, 449 (2008).
38. Eun Sik Kim, Kyoung Hyuk Jang, Liang Shi, Hyo Jin Seo, Taiju Tsuboi, and Kiyoshi Shimamura, J. Kor. Phy. Soc. **52**, 455 (2008).



Acknowledgements

The accomplishment of this paper benefits from the enlightenment of my supervisor, Hyojin Seo, whose inspiring insights, generous encouragements, and enthusiastic instructions have facilitated me much throughout my thesis writing. His penetrating and insightful comments afford me with inspiring source. He has been in constant concern about my paper, spared no pains to entertain my thesis draft. I would also like to extend my sincere thanks to Dr. Palamandala Babu, Chill Ok, JaeYong Je and KyoungHyuk Jang. Thanks to their instructive guidance and comprehensive education during the five years' schooling.

I would like to express my heartfelt gratitude to Prof. Yanlin Huang, Xinmin Zhang and Laishun Qin. Without their consistent and illuminating instruction, this thesis could not have reached its present form.

I am also greatly indebted to EunSik Kim, Xuebin Qiao, ByeongCheon Jeon, MiJu Kim and YuYu Tao of our workgroup, who gave me their help and time in listening to me and helping me work out my problems during the difficult course of the thesis.

Finally, my great gratitude also goes to my wife Qian Zhang, whose painstaking care I have benefited greatly from without which the completion of the thesis would not have been possible.